Mathematical modeling and experimental validation of thin low platinum content and functionally graded cathode catalyst layers

by

Kailyn Domican

A thesis submitted in partial fulfillment of the requirements for the degree of

Master of Science

Department of Mechanical Engineering
University of Alberta

Abstract

Low catalyst content remains a key requirement for the commercialization of polymer electrolyte fuel cells (PEFCs) into the energy, transportation, and material handling sectors. Understanding the fundamental phenomena reducing fuel cell performance at various stages of operation play a major role in PEFC optimization and reducing catalyst content. In this thesis, high performance PEFCs with low to moderate Pt loadings (27 - 112 $\mu g_{Pt}/cm^2$) have been fabricated using inkjet printing. To better understand thin low Pt content electrodes the PEFCs are tested at various back pressures, relative humidity, and oxygen partial pressures. The characterized PEFCs are then simulated using OpenFCST, an open-source FEM based fuel cell simulation framework, to aid in the investigation of key performance limiting phenomena. The simulations are obtained using a macro-homogeneous, non-isothermal MEA model where a multi-step reaction kinetics describes the oxygen reduction reaction. The model is then validated against the experimental Pt loading, ionomer loading, and oxygen partial pressure study. The successfully validated model highlighted key performance limitations between low Pt content and conventional (400 $\mu g_{Pt}/cm^2$) loading electrodes, while also highlighting the possible phenomena dictating ionomer and oxygen partial pressure performance. A mathematical model is also developed allowing the simulation of functionally graded electrodes. The model is then used to aid experimental design. To validate the new model two functionally graded ionomer electrodes are fabricated, characterized, and compared to the simulated results.

Keywords: polymer electrolyte fuel cells, finite element method, open-source, simulation, mathematical model ,membrane electrode assembly, functionally graded, low loading, thin electrode, ionomer loading, platinum loading, oxygen partial pressure, back pressure

Carpe diem

Acknowledgements

Firstly, I would like to take this opportunity to sincerely thank my supervisor Dr. Marc Secanell for providing me with the opportunity to work in such a comprehensive and cutting edge research team. His bedrock of knowledge, patients, critical thinking, and work ethic have been both flawless and incredibly inspirational. I feel truly fortunate to have encountered a supervisor whose leadership is set by example.

> *"We learn by example and by direct experience because there are real limits to the adequacy of verbal instruction."*
> — Malcolm Gladwell, *Blink*

I would also like to thank the ESDL research team for sharing their zeal for research, and creating such a pleasant and dynamic environment. I have learned as much from my colleagues as from my supervisor. It has been a true pleasure working along side you all, and I look forward to a time where we will chat and reminisce on the many moments shared at the University of Alberta.

Finally, I would like to thank my family for their unconditional love and support.

Table of Contents

List of Tables

List of Figures

Nomenclature

English Letters

$\bar{G}$	Molar Gibbs free energy, $[J \cdot mol^{-1}]$
$\bar{H}$	Molar enthalpy, $[J \cdot mol^{-1}]$
$\dot{W}$	Rate of work done by the system, $[W \cdot cm^{-3}]$
$\vec{N}$	Molar flux, $[mol \cdot cm^{-2} \cdot s^{-1}]$
A_0	Active area, $\left[m_{Pt}^2 \cdot g_{Pt}^{-1}\right]$
A_v	Volumetric active area, $\left[cm_{Pt}^2 \cdot cm_{cl}^{-3}\right]$
a_w	Water activity, $[-]$
D	Diffusion coefficient, $[cm^2 \cdot s^{-1}]$
E	Reversible cell potential, $[V]$
E_{cell}	Cell potential, $[V]$
EW	Equivalent weight, $[g \cdot mol^{-1}]$
F	Faradays constant, 96,485.3 $[C \cdot mol^{-1}]$
$I_{H_2}^{cross}$	Current produced from H_2 crossover, $[A]$
iR	Internal cell resistance, $[\Omega]$
j	Current density, $[A \cdot cm^{-3}]$
j^*	Reference scaling prefactor, 1,000 $[A \cdot cm^{-2}]$
$J_{H_2}^{cross}$	H_2 crossover rate, $[mol \cdot cm^{-2} s^{-1}]$
k	Thermal conductivity, $[W \cdot cm^{-1} \cdot K^{-1}]$

k_t Time constant, $[s^{-1}]$

M Molar weight, $[g \cdot mol^{-1}]$

n_{drag} Electro-osmotic drag coefficient

p Pressure, $[Pa]$

R Universal gas constant, 8.3144 $[J \cdot mol^{-1} \cdot K^{-1}]$

$R_{contact}$ Cell contact resistance, $[\Omega]$

R_{e^-} Electronic cell resistance, $[\Omega]$

R_{H^+} Protonic cell resistance, $[\Omega]$

S Volumetric source term, $[mol \cdot s^{-1} \cdot cm^{-3}]$

s stoichiometry

S_{heat} Volumetric heat source, $[W \cdot cm^{-3}]$

$slpm$ Standard litre per minute

T Temperature, $[K]$

V_{Pt} Platinum mass loading per unit volume in the catalyst layer, $[g_{Pt} \cdot cm^{-3}]$

$wt.\%$ Weight percentage

x Molar fraction of the gaseous species

z Valency of species, $[C \cdot mol^{-1}]$

A Area, $[cm^2]$

Abbreviations

ACL Anode catalyst layer

AFC Alkaline fuel cell

AFCC Automotive Fuel Cell Corporation Corp.

AGDL Anode gas diffusion layer

AMPL Anode microporous layer

BC Boundary conditions

BPP Bi-polar plates

CCL Cathode catalyst layer

CCM Catalyst coated membrane

CGDL Cathode gas diffusion layer

CL Catalyst layer

CMPL Cathode microporous layer

CV Cyclic voltammetry

DA Dissociative adsorption

DL Double-layer

DOF Degrees of freedom

DTK Double-trap kinetics

ECSA Electrochemical surface area

EDX Energy dispersive X-ray spectroscopy

EG Ethylene glycol

ESDL Energy Systems Design Laboratory

FEM Finite element method

GDL Gas diffusion layer

Gly Glycerol

HAD Hydrogen adsorption/desorption

HER Hydrogen evolution reaction

HOR Hydrogen oxidation reaction

IJP Inkjet printing

LSV Linear sweep voltammetry

MCFC Molten carbonate fuel cell

MEA Membrane electrode assembly

ML Membrane layer

MPL Microporous layer

NL Nafion® loading

OCV Open cell voltage

OEMs Original equipment manufacturers

OpenFCST Open-source fuel cell simulation toolbox

ORR Oxygen reduction reaction

PAFC Phosphoric acid fuel cell

Paral Parallel

PDE Partial differential equation

PEFC Polymer electrolyte fuel cell

PEM Polymer electrolyte membrane

Pt Platinum

PTFE Polytetrafluoroethylene

RA Reductive adsorption

RD Reductive desorption

RH Relative humidity

RT Reductive transition

SEM Scanning electron microscope

SOFC Solid oxide fuel cell

SOP Standard operating procedure

STDEV Standard deviation

TK Tafel kinetics

VACNTs Vertically aligned carbon nanotubes

Greek Letters

λ Membrane water content

μ Percolation universal constant

ϕ Electrical potential

σ Ionic conductivity, $[S \cdot cm^{-1}]$

ε Porosity

ε^{th} Percolation threshold

ε_N Electrolyte phase volume fraction

ε_S Solid phase volume fraction

ε_V Void phase volume fraction

Subscripts and Superscripts

0 Reference state

a anode

c cathode

d Reference

e^- Electron

eff Effective value averaged over a representative elementary volume

eq Equilibrium state

g Gas mixture

gkt Gasket

H^+ Proton

H_2 Hydrogen gas

H_2O Water vapour

HOR Hydrogen oxidation reaction

i Index of species

$irrev$ Irreversible

lam Lamination

m Membrane (electrolyte) phase

N_2 Nitrogen

O_2 Oxygen gas

ORR Oxygen reduction reaction

$overall$ Overall reaction

ref Reference

rev Reversible

S Solid phase

sat Saturation

$T0$ Start time interval

$T1$ End time interval

th Threshold

tot Total

vap Vaporization

Chapter 1

Introduction

1.1 Background

A fuel cell is a electrochemical device that converts chemical energy into electrical energy. The conversion of chemical energy into electrical energy using a fuel cell was first demonstrated over 160 years ago [3]. However, it is only in the last two decades that fuel cells have gained substantial attention in applications such as portable power generation, transportation, material handling, and backup power generation. The cause of this increased attention is due to the attractive system efficiencies and environmental benefits associated with fuel cell technology.

There are several types of fuel cells, which vary in temperatures regimes, materials, reactants, and products [4, 5]. Out of the five main types, *i.e.*, phosphoric acid (PAFC), polymer electrolyte (PEFC), alkaline (AFC) molten carbonate (MCFC), and solid-oxide fuel cells (SOFC), PEFCs have emerged as one of the more versatile options as they offer high efficiencies, low emissions, and relatively low operating temperatures (<100℃), providing suitable transient characteristics for both start up and shut down [6, 7].

Positive prospects for PEFCs in the automotive sector can be seen in major original equipment manufacturers (OEMs) such as General Motors, Toyota, Honda, Hyundai, and Ford. They all have signed memorandum of understanding with several countries providing mutual collaborative efforts into product development and infrastructure investments. Over the past two decades major improvements have been seen in PEFC performance, resulting in decreased costs by reducing catalyst content [8–10], while substantially increasing durability, power density, and economic feasibility. Research shows positive trends towards meeting the Department of Energy 2015

target of $30/kW [11].

The motivation of this project is to further reduce Pt loading in PEFC cathodes. The goal is then to understand and characterize thin, low Pt content electrodes (27 $\mu g_{Pt}/cm^2$) and moderately loaded electrodes ($\approx$ 100 $\mu g_{Pt}/cm^2$) manufactured using inkjet printing and to study their performance under a variety of conditions. Thin low Pt content electrodes have shown to have some of the highest utilization [1, 12, 13]. This is a result of the reduced transport length scales for ion and mass transportation. In previous work by Shukla et al. [1] an ionomer study demonstrated that thin low Pt content electrodes have little sensitivity to ionomer loading. Saha et al. [13] showed that increasing Pt content, and as a result thickness, added to the species transport losses and reactant supply issues. In this work, electrodes with various Pt content and thickness are characterized and tested at varying operating conditions to elucidate the impact operating conditions has on performance.

Improving PEFCs product life time and performance requires large amounts of experimental testing time. Experimental research in PEFCs is impaired by limitations such as material and manufacturing costs. Therefore, given the inherent time constraints and costs of experimental research an optimum product is difficult to arrive at. Modelling is a crucial step in increasing the understanding of PEFC especially where the components size is a limiting factor. This is especially true for the fuel cell components where their geometries and location make it incredibly difficult to discern design issues. PEFCs are complex multi-component systems where several phenomena are occurring simultaneously. Modelling can aid in this respect guiding design and allowing optimization which would otherwise take several months if not years to validate experimentally.

Therefore, a second goal of this work is to validate a mathematical model recently developed in our group [14], thereby reducing experimental guess work providing intelligent and effective design direction. The simulated results are obtained using an, open-source fuel cell finite element software developed in the Energy Systems Design Laboratory (ESDL) at the University of Alberta, namely the Open-source Fuel Cell Simulation Toolbox (OpenFCST)[15] to expose the performance limiting factors. The goal is to validate the mathematical model and its ability to capture the change in performance due to catalyst and ionomer loading using a recently implemented kinetics model by Moore [14]. Once the model has been validated it can then be used to aid fuel cell design and direct experimental efforts in future works.

In addition to the Pt and ionomer validation, the motivation behind this work is also to enhance the current mathematical model to incorporate functionally graded catalyst layer (CL) capabilities. Functionally graded CLs can be used in an effort to optimize the CL mass transport properties. The mathematical model is validated by comparing against experimentally tested functionally graded CLs. Validation of this enhancement can then aid functionally graded CL design and guide experimental fabrication and optimization efforts, saving both time and expense.

1.2 PEFC Background

The fundamental function of a fuel cell is to convert chemical energy in a fuel to electrical energy. The chemical energy is harvested by means of an electrochemical reaction. There are several variations of fuel cells, typically categorized by the type of electrolyte. In this work, the PEFCs are considered where the fuel supplied is hydrogen gas (H_2), and the reactant is oxygen (O_2). The products of this reaction are electricity, heat, and water. This differs from typical energy systems where the fuel is combusted in a chamber/engine producing heat, rather than electricity. Combustion of fuel is limited by the Carnot cycle, whereas electrochemical reactions can extract more useful high grade energy in the form of electricity, at greater efficiencies [16].

Figure 1.1 illustrates the basic components and species transport found during PEFC operation. The overall exothermic electrochemical reaction taking place inside the PEFC is described by:

$$2H_2 + O_2 \rightleftharpoons 2H_2O \tag{1.1}$$

where the reaction can be broken down into two fundamental half-cell reactions *i.e.*, the oxidation of hydrogen, and the reduction of oxygen. The hydrogen oxidation reaction (HOR) occurs in the anode and is given as:

$$2H_{2(g)} \rightleftharpoons 4H^+_{(aq)} + 4e^- \quad \textbf{: Anode} \tag{1.2}$$

If there is an external circuit connecting the anode and cathode, the electrons produced travel along the electrical conductor while the protons travel through the polymer electrolyte membrane (PEM) towards the cathode side of the cell. The protons and electrons arriving at the cathode side are consumed in the oxygen reduction reaction (ORR), given as:

$$O_{2(g)} + 4H^+_{(aq)} + 4e^- \rightleftharpoons 2H_2O_{(l)} \quad \textbf{: Cathode} \tag{1.3}$$

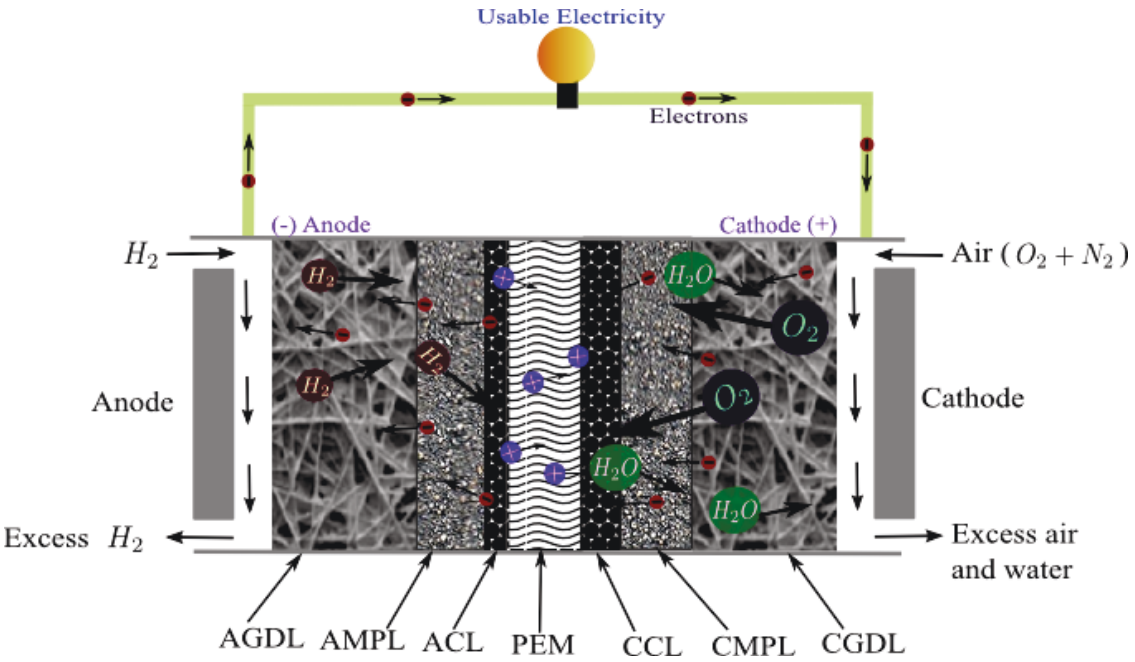

Figure 1.1 – Basic schematics and operation diagram of the polymer electrolyte fuel cell (PEFC). Reprinted with permission [17]

Reactions in Equation (1.2) and (1.3), take place in the anode catalyst layer (ACL) and cathode catalyst layer (CCL), respectively, where the platinum catalyst is found. The combination of ACL, CCL and PEM, is know as the catalyst coated membrane (CCM), where the PEM acts as an electronic and gas insulator between the two CLs.

The PEFC is enclosed in a stack assembly whereby the reactants are supplied through flow channels which can have one of several flow pattern designs [18]. These flow channels are etched into conductive material plates, called bi-polar plates (BPP). The supplied reactants diffuse or convect (dependent on flow channel arrangement) through the gas diffusion layer (GDL). The GDL is a porous media made up of either carbon fibres, paper, or cloth. GDLs on the anode side (AGDL) and cathode side (CGDL), generally are impregnated with polytetrafluroethylene (PTFE) a hydrophobic material in order to reduce the liquid water build up and blockage of pores which would otherwise inhibit reactant transport. Once the gas has reached the inner boundary of the GDL, the gas enters the microporous layer (MPL), which is found on both the anode side (AMPL) and cathode side (CMPL). MPLs have a reduced porosity compared to GDLs and act as an interface between the GDLs and CLs. MPLs have two main functions, *i.e.*, reduce the interfacial contact resistance between the GDLs and the CLs, while also providing good water management in the CLs.

The reactants then diffuse into the CLs where they react at the catalyst sites.

The electrochemical reaction requires three criteria, *i.e.*, sufficient electrical conducting network to transport the electrons between the CLs and BPP, sufficient ionomer content to provide protonic transport from the reaction site to the membrane layer (ML), and sufficient reactant transport to the ionomer covered Pt site. These three criteria provide the sufficient species for the HOR and ORR to occur. If any of the three are omitted the reaction will not take place. The most common ionomer used in the CLs and in the ML also refereed to as the PEM, is Nafion®. In CLs, transport of electrons occurs only in the solid phase and protons in the ionomer phase, while reactants in a gas phase diffuse through the pore (void) space.

Fuel cell performance is most commonly reported using a polarization curve, where the voltage-current relationship is graphed. The current is usually normalized by the area of the fuel cell, giving performance in terms of current density, A/cm^2. Representation of the performance in terms of current density allows the comparisons of both large and small scale PEFCs. When no current is being drawn the cell voltage remains at the open cell voltage (OCV). Connecting the system to a circuit and drawing a current will result in the cell voltage decreasing. There are three types of phenomena that cause cell voltage losses when drawing current, *i.e.*, kinetic, ohmic, and mass transport losses. Kinetic losses are most dominant at low overpotentials where small amounts of current are produced and are associated with activation losses. Ohmic losses occur at moderate overpotentials where the ionic and electronic conduction losses are dominant. At relatively high current densities, large amounts of water production and reactant depletion take place resulting in mass transport losses becoming dominant. When excess water production is resulting in mass transport issues it is usually refereed to as '*flooding*'. When reactant diffusion is the limiting factor cell '*starvation*' is said to occur. Typically mass transport limitations are a combination of cell flooding and starvation.

1.3 Literature Review

This work is primarily concerned with the fabrication and testing of thin low Pt content electrodes. To further understand the results, a mathematical model for thin low Pt content electrodes is also developed. Fabrication is carried out using an inkjet printing method, a relatively new fabrication method in the fuel cell litera-

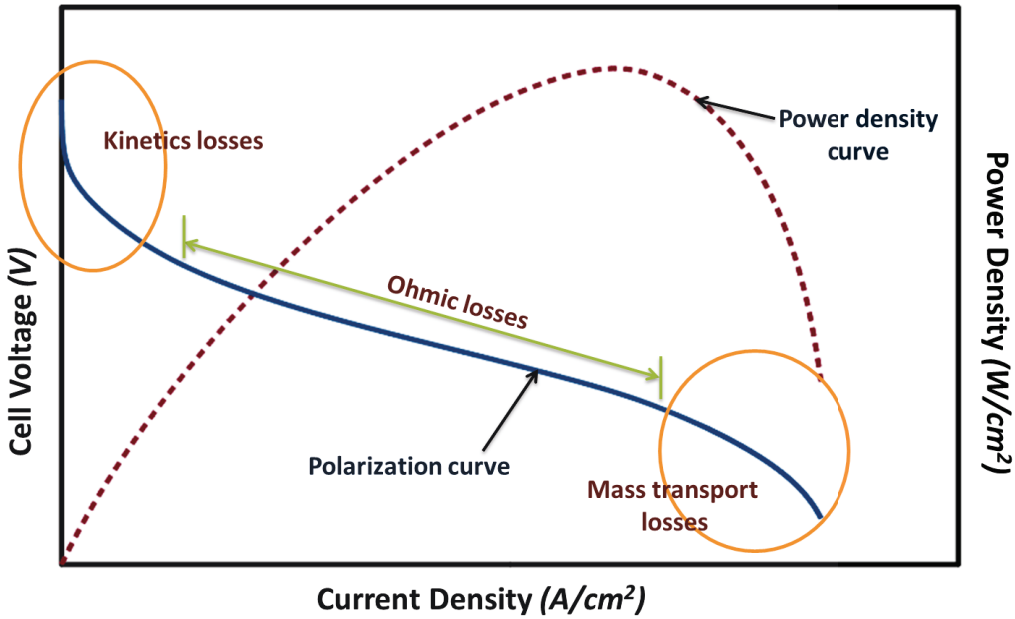

Figure 1.2 – Typical performance characteristics of a PEFC. Reprinted with permission [17]

ture. Analysis and validation of the mathematical model contains three parts, *i.e.*, the appropriate prediction of ionomer loading, platinum loading, and oxygen partial pressure.

The literature review has been sectioned into three areas, *viz.*, inkjet printing, platinum loading, and functionally graded CLs.

1.3.1 Inkjet Printing

Several methods are available to fabricate PEFC catalyst layers. For the more commonly used '*wet methods*', solvents are used to suspend the catalysed particles in a liquid which can then be easily deposited onto the substrate. Such methods include hand painting [19], screen printing [20, 21], spray [22], electro-spray [23], and Meyer bar or Dr. Blade [19, 24]. Fabrication of CLs using these methods can achieve sufficiently low Pt loadings, provided a low platinum on carbon support (Pt|C) is used. However, fabricating layers using conventional wet methods tend to produce layers which are still considered relatively thick at 3 - 5 μm [25, 26]. Moreover fabrication of such thin CLs creates challenges in terms of rheology, and Dr. Blade height. In addition, at relatively low Pt loadings these methods can lack adequate control when attempting fine loading studies [19].

Thin (200 Å - 1 μm) CL deposition methods have also been investigate in an effort to decrease thickness and increase utilization. These methods consist of ion beam assisted deposition [12], pulse laser deposition [27], and sputter deposition [28, 29]. Unlike the conventional wet methods which use a catalyst ink to deposit onto the substrate, these directly deposit the metal over the substrate without the carbon support and have been shown to produce ultra-thin as well as ultra-low Pt loaded CLs. Depositing such small particle sizes, giving rise to high electrochemical surface area (ECSA), however this small particle size and large active area is thought to decrease over time due to Ostwald ripening effects. Ostwald ripping occurs as larger particles are more energetically favoured than smaller particles, causing small particles to dissolve and redeposit onto larger particles. This process increases the average particle diameter and in return reduces ECSA values [30–32]. In addition, these deposition methods due to equipment complexity and strict environment control requirements are very expensive making them undesirable for industrial applications.

In more recent research, inkjet printing (IJP) has been investigated [1, 13, 33–35]. Inkjet deposition techniques have drop on demand control with high precession and little transfer losses compared to that of conventional spray coating, and Meyer bar or Dr. Blade methods. Moreover, inkjet methods can achieve loadings equivalent to those seen with ultra-low Pt loading technologies, without the inherent complexity or strict environment conditions.

Taylor et al. [33] used a thermal inkjet printer to fabricate CLs with loadings of $<$ 50 $\mu g_{Pt}/cm^2$. Using a water based catalyst ink solution they tailored the rheology of the ink to provide solution properties compatible with the cartridge design. The catalyst ink solution was printed onto a GDL substrate and compared to conventional screen printing and hand painted methods showing increases in Pt utilization and uniform thickness. In addition the versatility of IJP was demonstrated by fabricating functionally graded CLs, showing further increased performance compared to that of homogeneous IJP CLs. However, no thickness analysis was conducted.

There are two types of IJP methods, thermal as used in the work by Taylor et al. [33] and piezo-electric [1, 13]. Each provide picoliter drop control. Initial PEFC research with piezo-electric IJP was performed by Saha et al. [13]. Unlike thermal IJP, piezo-electric inkjet printers are more susceptible to air blockages, therefore sufficient rheology work is required to achieve a catalyst ink viscosity which is compatible with

the inkjet cartridges. Saha et al. [13] demonstrated piezo-electric IJP as a viable and practical method, fabricating thin (1 - 5 μm) CLs with low Pt loading in the range of 20 - 120 $\mu g_{Pt}/cm^2$. In this work the catalyst ink is directly coated onto the ML creating a catalyst coated membrane, as oppose to coating onto the GDL as seen by Taylor et al. CCMs have shown to have favourably low electrical resistance [1, 36, 37] compared to those seen in decal methods [37, 38]. Saha et al. reported exceptionally high Pt utilization values of $\approx$ 100% at loadings of 20 and 60 $\mu g_{Pt}/cm^2$. They also observed a gradual decrease in utilization at higher Pt content and thickness. The highest loading, 120 $\mu g_{Pt}/cm^2$, having a Pt utilization of 79%, only 13% greater than the conventional spray coated cell with 140 $\mu g_{Pt}/cm^2$. This decrease utilization was not further investigation in order to discern the cause of lowering utilization. As a result further work is needed in this area.

Saha et al., using SEM imaging, found the average thickness of one single printer pass (1 layer) equal to 0.7 μm while 10 layers had an average thickness of 5 μm. This analysis showed that the thickness was not a linear relationship, however, it was assumed that each layer had a thickness of 0.5 μm and no further thickness analysis was carried out. Therefore, further work characterizing CL thickness versus the number of passes is needed.

In later work Saha et al. [39] showed optical density maps for carbon and ionomer distribution using energy dispersive X-ray spectroscopy (EDX). The results demonstrated that IJP electrodes have good homogeneity for both ionomer and carbon throughout the CL cross section, compared to conventional Meyer bar method which showed areas of poor ionomer homogeneity and regions of carbon agglomeration. In both these studies 40 wt.% Pt|C supports are used.

Shukla et al. [1] used the same IJP technology and process as Saha et al. [13] to investigate the effect of ionomer loading on cell performance. In this study Shukla et al. fabricated CLs with 27 $\mu g_{Pt}/cm^2$ using a 20 wt.% Pt|C, utilizing the high ECSA associated with low wt.% of Pt|C supports [30–32]. Here ionomer loadings were varied from 10 - 50 wt.% in 10 wt.% intervals. Ionomer loading has been thoroughly studied for conventional methods [23, 40–43] however, no work had been done on IJP low Pt content CLs. Shukla et al. found that these thin low Pt content electrodes showed low sensitivity from 20 - 40 wt.% ionomer loadings with the exception of the extreme 10 and 50 wt.% cases where ionomer coverage and porosity issues arose. This differs greatly from conventional CLs which show sensitivity to ionomer loading, and

the optimum ionomer loading is found to lie within the 30 - 36 wt.% range. Further demonstrating the advantages of IJP low Pt content CLs, Shukla et al. compared against a conventional spray coated CL showing that IJP catalyst layers have far greater mass activities.

1.3.2 Low Pt Loading Electrodes

Since the 1960s where PEFCs found their first applications in NASA's Gemini space flights, major leaps in fuel cell technological and engineering have occurred [44, 45]. These '*quantum leaps*' have allowed substantial increases in performance while simultaneously reducing the expensive platinum catalyst used from 400 $\mu g_{Pt}/cm^2$ in the Gemini project, to 10 $\mu g_{Pt}/cm^2$ for the ACL and 50 $\mu g_{Pt}/cm^2$ in the CCL [45].

Much of these developments have come from electrode configuration, Pt alloying, and also improved electrode fabrication technologies. The substantial decrease in Pt loading has increased the need for high utilization of the catalyst. In an effort to achieve this many works are now focusing on finding an optimal CL thickness, whereby the active layer is sufficiently thick to allow support for the active Pt sites but also sufficiently thin so that the layer is not subjected to charge transport or mass transport limitation [29, 46, 47]. Moreover, with the substantial decrease in loading, efforts are now required in finding a suitable fabrication method capable of fine loading control while maintaining a thin electrode.

In the literature many methods have been used in order to fabricate low Pt content electrode. These consist of ion beam assisted deposition [12], pulse laser deposition [27], sputter deposition [28, 29], spraying [48], electrospray [23, 49, 50], screen-printing [51], and printing [34].

Martin et al. [52] used an electrospray method to coat MPLs with 10 $\mu g_{Pt}/cm^2$. The cell performance showed high Pt utilization and cell thickness between 50 - 80 μm. The large thickness resulted in a high porosity of 96% allowing good mass transport characteristics. However, the large thickness is undesirable in terms of charge species transport. In other works, Martin et al. [49] [23] conducted Pt (100 - 12.5 $\mu g_{Pt}/cm^2$) and ionomer loading (20 - 60 wt.%) studies showing increased performance with increase ionomer content. The 12.5 $\mu g_{Pt}/cm^2$ loaded electrode had the lowest sensitivity to ionomer loading and showed similar performances for 20 - 40

wt.% ionomer loadings with large performance drops outside this range, a trend also observed in the IJP study by Shukla et al. [1]. The overall performance of the electrosprayed electrodes were still very low only achieving a maximum current density of 0.225 A/cm^2 using pure O_2 as the cathode feed gas. This low cell performance is possible due to the large CL thickness leading to substantial charge species transport losses. Therefore, there is a need to fabricate low Pt content electrodes while maintaining thin CL thickness to avoid the large charge transfer losses.

Thin methods such as sputter deposition techniques have also been used [28, 53] to fabricate thin electrodes. Fofana et al. [53] fabricated CCLs with 50 $\mu g_{Pt}/cm^2$, using novel multilayer cathode electrode structures and compared against a conventional 200 $\mu g_{Pt}/cm^2$ electrode. The overall thickness of the layers ranged between a minimum of 10 μm carbon-ionomer layer with a 222 Å Pt layer on top, to a maximum thickness of 30 μm with 222 Å Pt layer at the end of each 10 μm carbon-ionomer layer [54]. The results showed higher Pt utilization and limiting current compared to the conventional electrode. However, the CLs are still considerably large in thickness in addition to the Pt layers being located relatively far from the membrane layer.

Tian et al. [55] using a novel method of growing vertically aligned carbon nanotubes (VACNTs) then coated the VACNTs using sputter deposition. The Pt coated CCLs had a thickness of 1.2 μm and a Pt loading of 35 $\mu g_{Pt}/cm^2$. The low Pt content cells were then compared against a conventionally loaded electrode with 400 $\mu g_{Pt}/cm^2$, showing similar performance to the conventional electrode with an extended mass transport region. The result from this study showed that large cell performances can be achieved with thin low Pt content cells, showing favourable results, however, due to the complexity of the equipment there remains uncertainty about the scalability for industrial applications.

Ohma et al. [51] used screen-printing [56] to fabricated two Pt content loadings, 120 $\mu g_{Pt}/cm^2$ (3.7 μm) and 350 $\mu g_{Pt}/cm^2$ (11 μm). Ohma et al. carried out an extensive study comparing both electrodes showing the losses for several phenomena throughout the PEFC. Their findings showed that with the 11 μm CL the greatest loss was associated with protonic transport, while in the 3.7 μm CL the majority of the losses were associated with activation and an unknown loss which they hypothesized to stem from the local gas-ionomer interface resistance as also thought by other authors [57] [58].

When considering Pt catalysts, high utilization and ECSA are both desirable and vital to having low Pt content electrodes with adequate cell performance. It has been shown that with lower wt.% Pt|C, smaller Pt particles are formed giving rise to greater ECSA values [30–32]. Qi and Kaufman [42] conducted a study on several fabrication methods using both 20 and 40 wt.% Pt|C, finding that at low Pt loadings ($< 200\ \mu g_{Pt}/cm^2$) the 20 wt.% Pt|C greatly outperformed the 40 wt.% Pt|C at 0.65 V. Qi and Kaufman found that lower Pt content was required for equivalent performance when using 20 wt.% Pt|C due to the reduced particle size and higher ECSA. In this case the 40 wt.% Pt|C (3.9 nm) being almost twice as large as the 20 wt.% Pt|C (2.0 nm) [30–32]. Therefore, during the fabrication of low Pt content electrodes, low Pt on carbon supports are highly recommended.

In the literature there are few low Pt loading mathematical model studies. Yoon and Weber [59] conducted a study on low Pt loading with no experimental validation, using a kinetics model that considered the OH_{ads} coverage on Pt sites. The main focus of the paper however, is on explaining mass transport limitations which is investigated using an agglomerate model. They conclude that there exists an unexplained resistances occurring at very low Pt loadings which is not seen in conventionally loaded electrodes and that the reason for this is due to a higher oxygen fluxes through the ionomer film and longer diffusion pathways. Although the study simulates loadings of 200 , 130, and 60 $\mu g_{Pt}/cm^2$ the kinetic region sees a relatively small decrease in performance. This differs from experimental observations where a large decrease in performance is seen [13]. Therefore, the qualitative and quantitative comparisons of simulated results against experimental results is required, in order to ensure adequate prediction of low Pt loading electrodes.

Recently Wang et al. [60] proposed the double-trap kinetic (DTK) model which accounts for the coverage of two dominant intermediate species (OH_{ads}, O_{ads}). Moore et al. [61] implemented this model into OpenFCST [15] and further improved on Wang's model by correcting for the local reactant (O_2) concentrations which in turn affects the coverage of intermediate species [62]. Using the DTK model Moore observed that the better prediction of the kinetic and ohmic region for conventional loading (400 $\mu g_{Pt}/cm^2$) CCLs, at various operating conditions. However, Moore [14] did not thoroughly study the effect at low Pt content ($< 100\ \mu g_{Pt}/cm^2$) CLs. This is discussed in this work, where low Pt content electrodes are fabricated, tested, and compared to simulations using DTK model and the traditional TK model for various Pt loadings, with particular focus on the kinetic region.

1.3.3 Functionally Graded Electrodes

In conventional CLs there is a constant trade off with protonic transport and mass transport limitations. The tradeoff arises from the relatively large thickness of conventional electrodes (10 μm) roughly five times thicker compared to that of thin low Pt content electrodes with a thickness of 1.55 μm [1]. Due to these thinner CLs mass transport limitations are reduced, allowing the thin low Pt content electrodes to have higher percentage of ionomer content promoting protonic transport [43]. Without resulting in greater mass transport losses, which would otherwise occur in conventional CLs. In addition, the reduced thickness of low Pt content electrodes results in a shorter transport path for the protons further reducing the operating losses. Wilson and Gottesfeld [38] showed that a CL of thickness lower than 5 μm will have adequate diffusion pathways to avoid reactant transport limitations, while also providing providing good proton transpiration. This idea was further demonstrated by Sasikumar et al. [43] finding that with reducing Pt content and thickness the best performance was found at greater ionomer concentrations ($\approx$ 40 wt.%). These high ionomer levels allow for sufficient protonic transfer, however at sufficiently high current mass transport limitation become an issue [41, 43]. To counteract this, non-homogeneous CLs are being investigated, in an attempt to maintain good protonic transport while reducing the incurred mass transport losses.

Fabrication of non-homogeneous CLs involves the variation of ionomer and/or Pt loading concentrations through the CL thickness (through-the-channel) and/or along the CL (along-the-channel)[63–65]. These types of CLs are referred to as functionally graded CLs. Current research has mainly focused on functionally grading either the ionomer or Pt content along the CL thickness. So far, these studies have all been conducted using conventional CL techniques and loadings. Using inkjet printing a much higher spacial resolution could be achieved.

Ionomer grading has shown improvements in both kinetic and mass transport regions of the polarization curve when having the highest wt.% of ionomer content at the ML-CL interface and the lowest wt.% at the CL-GDL interface. This ensures maximum proton transport in the region of greatest ion flux, and maximum porosity where the greatest gaseous flux is located. This idea has been confirmed both experimentally and using mathematical models [63, 66, 67]. Antoine et al. [67] conducted an

experimental and numerical study on the best location for Pt content for both porous and non porous electrodes. Both the experimental and numerical model found that for non porous electrodes the Pt should be situated at the CL-GDL interface, however for porous electrodes (as seen in PEFCs) the best performance is found with Pt located at the ML-CL interface. Showing that the catalyst utilization efficiency is dependent on both the diffusion and ionic transport, and that the optimal CL should be as thin as possible.

Song et al. [66] conducted one of the only mathematical modelling studies on functionally graded electrodes. A numerical single and double variable optimization for both ionomer and Pt loading at a cell voltage of 0.6 V, for a 26 μm thick CL. For the single variable optimization a linear distribution of ionomer was found to have the greatest wt.% at the ML-CL and lowest at the CL-GDL interface. The Pt loading produced the same linear trend having the highest Pt content at the ML-CL interface. Using a double variable optimization showed linear ionomer distribution as previously observed with the single variable optimization and non-linear distribution of the Pt loading having a convex increasing function containing the highest loading toward the ML-CL boundary. Double variable optimization showed to have marginally better performance, concluding that ionomer distribution has the strongest effect.

Taylor et al. [33] using the thermal IJP fabricated CLs with 500 $\mu g_{Pt}/cm^2$ showing that functionally grading the electrode for both Pt and ionomer showed best performance when the highest Pt and ionomer contents were found at the ML-CL interface, a similar distribution as described before and in the work by Xie et al. [63]. However in terms of thin low Pt content electrodes no functionally graded investigations have been carried out.

In summary, the above review for functionally graded CLs suggest that high Pt and ionomer content at the ML-CL interface and low contents at the CL-GDL interface are most optimal. This same idea will be investigated for thin low Pt content electrodes in this work, by initial observing ionomer distribution effects. Mathematical modelling of functionally graded electrodes has scarcely been analyzed and the gradation has only been in one direction. Using inkjet printing gradation in all three directions is possible. To achieve this goal a validated and multi-directional fuel cell modelling framework is required. This has been developed in this thesis.

In terms of low Pt content electrodes the literature has raised many areas that

requires further investigation. Thin low Pt content electrode studies have showed that low Pt content electrodes provide improved utilization, however the simultaneous experimental characterization and mathematical modelling of these electrodes has seldomly been performed. Simple semi-empirical models have been proposed [68–70], however, a comprehensive study of ionomer and Pt loading of low Pt content electrodes has not been performed.

Literature has also shown the importance of having high ECSA values when fabricating low Pt content electrodes. Due to the larger surface area of low wt.% Pt|C, this work will mainly focus solely on the 20 wt.% Pt|C.

1.4 Contributions

In this thesis the following contributions are made:

1. Experimental fabrication and characterization of several Pt loading electrodes over various operating conditions. Using ex-situ and in-situ characterization techniques to discern performance, electrochemical active areas, surface morphology, and thickness properties.

2. Mathematical model used to analyze low Pt content electrodes in an effort to better understand the phenomena limiting cell performance.

3. Study of functionally graded electrodes, in order to better understand the underlying phenomena limiting cell performance and to direct future experimental efforts.

1.5 Thesis Outline

Chapter 1 introduced the reader to fuel cells and their application in society. It has also described the fundamental mechanism behind fuel cell operation and the merits of coupling experimental and mathematical model efforts. The first chapter also provided an overview of the developments in inkjet printing, ionomer loading, platinum loading and functionally graded electrodes. Chapter 2 presents the experimental procedure and methodology used to fabricate and test PEFCs which have been produced in house. Chapter 3 presents the fundamentals of the mathematical model, outlining the inherent assumptions and governing equations. Chapter 4 presents the experimental characterization results for the PEFCs, later comparing the performance against that predicted results from the mathematical model. Finally, chapter 5 concludes on the research and results from this work and provides areas for future efforts.

Chapter 2

Experimental Fabrication, Characterization and Testing

2.1 Introduction

There are several ways to fabricate CCMs as mentioned in Section 1.3. In this work, a wet method is used, namely inkjet printing, focusing on the fabrication of low Pt content electrodes from 27 to 112 $\mu g_{Pt}/cm^2$. When carrying out low Pt loading studies, as done in this work, it is important to have fine deposition control.

In this work a piezo-electric inkjet printer is utilized in order to obtain fine deposition control. A piezo-electric printer works by using a piezo-electric actuator to decreases the nozzle volume, causing ink to jet onto the substrate, as seen in Figure 2.1 (d). This inkjet method allows for drop on demand giving high control (1 - 10 pL) over the amount of ink jetted onto the substrate (membrane in this work) with very little waste of ink compared to traditional methods, *i.e.*, painted [19], screen printing [20, 21], spray [22], Meyer bar, and Dr. Blade [19, 24].

2.2 Materials, Fabrication, and Equipment

In this work, CCMs have been prepared in house to achieve varying platinum loadings. To fabricate CCMs platinum on carbon support, and ionomer are mixed with additional solvents to create a catalyst ink, also known as an ink slurry. The platinum and carbon are supplied together in a powder form where the platinum is attached to the carbon support.

In this work two different platinum concentrations are used. 20 wt.% Pt|C (Vulcan XC-72 carbon black HiSPEC™ 3000) and 46.7 wt.% Pt|C (Graphitized carbon black, Tanaka TEC10EA50E). The different Pt|C ratios allows the study of CCMs with similar loadings but different concentrations of Pt on the carbon.

The ionomer used when fabricating the ink slurry is a 5 wt.% Nafion® ionomer solution (1,100 EW, H^+ form). Two solvents have been used in this study, namely, isopropanol mixed with either Glycerol (Gly) or Ethylene glycol (EG). The role of the Gly and EG is to increase the viscosity of the ink slurry so that it is compatible with the inkjet printer cartridge, which requires a viscosity in the region of 10 centipoise.

Fabrication for both Pt catalysts and solvents have been carried out using the same standard operating procedure (SOP), Table 2.1 lists the four ink variations used in this work.

Table 2.1 – Ink types used to fabricate the CCMs

Ink Name	Pt|C Type wt.%	Solvent Type
20% Pt|C Gly	20	Glycerol
20% Pt|C EG	20	Ethylene glycol
20% Pt|C EG*	20	Ethylene glycol (with larger EG content)
46.7% Pt|C Gly	46.7	Glycerol

2.2.1 Catalyst Ink Formulation

The ink slurry is obtained by mixing the desired amounts of Pt|C powder, 5 wt.% ionomer solution, isopropanol, and Gly or EG. Once the ink has been formulated for the desired ionomer and Pt loadings, the ink undergoes stages of sonification in order to break up large unwanted aggregates. The ink is then injected into the inkjet cartridge and placed into a commercially available piezo-electric inkjet printer (Dimatix Materials Printer, DPM-2800 series, Fujifilm), as seen in Figure 2.1 (a) (b).

The inkjet cartridge has 16 nozzles which are linearly spaced 254 microns apart. Typical drop sizes are 10 pL (DMC-11610), as seen in Figure 2.1 (c). The cartridge assembly holder is rotated to achieve a perpendicular distance of 20 μm between each nozzle. When printing the cartridge is swept laterally across the printing platform depositing the ink directly onto the membrane (NR211) forming a 5 cm^2 active area.

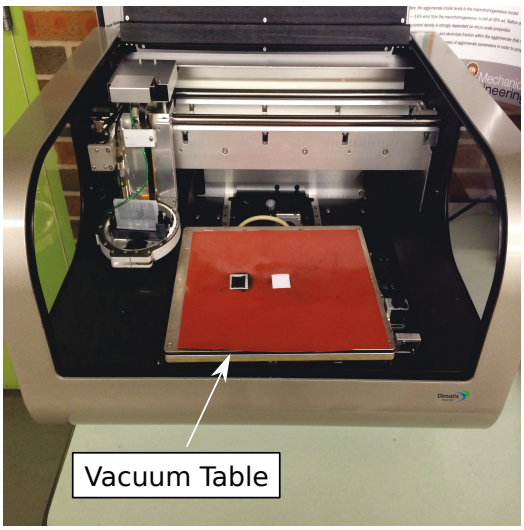

(a) Dimatix piezo-electric printer

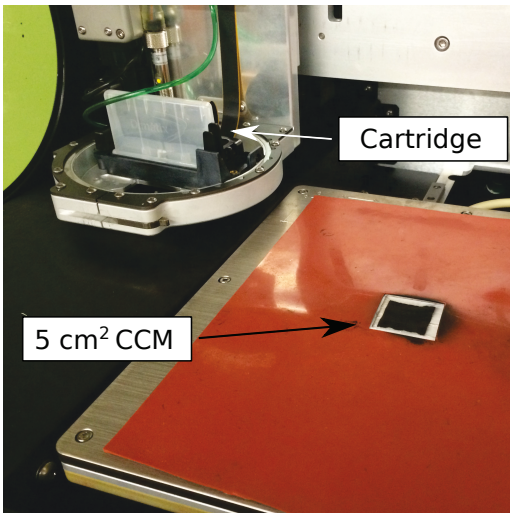

(b) View of cartridge and printed CCM

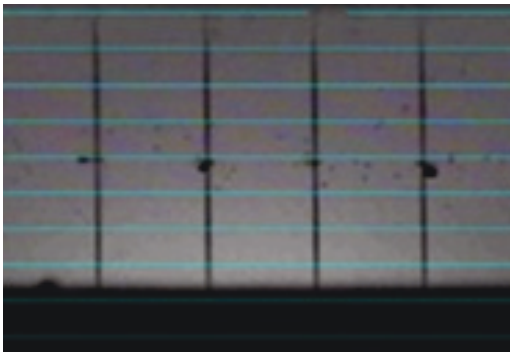

(c) Ink jet nozzles during operation

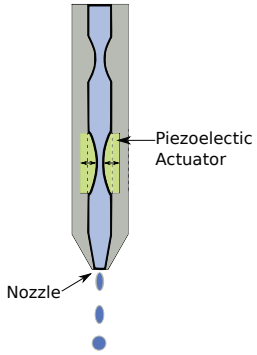

(d) Piezo-electric printer nozzle

Figure 2.1 – Commercially available piezo-electric printer (a) used to deposit catalyst ink onto the substrate. (b) showing cartridge and printed CCM, (c) showing the printer nozzle during operation, (d) schematic of piezo-electric printing nozzle.

Once the cartridge has reached the end of the active area, one pass has been completed. In this work, the desired Pt loading is controlled by the number of full passes over the active area (5-20 passes/layers).

After the first CL has been fully deposited onto the membrane. The half CCM is placed into an oven at 80 °C for 24 hours until fully dried, before printing the opposite side. Once both sides of the CCM have been printed and completely dried the CCM is then submerged into boiling deionized water for 3 hrs to remove the residual solvents. After boiling, the CCM is rinsed with deionized water and placed into an oven to dry for three hours.

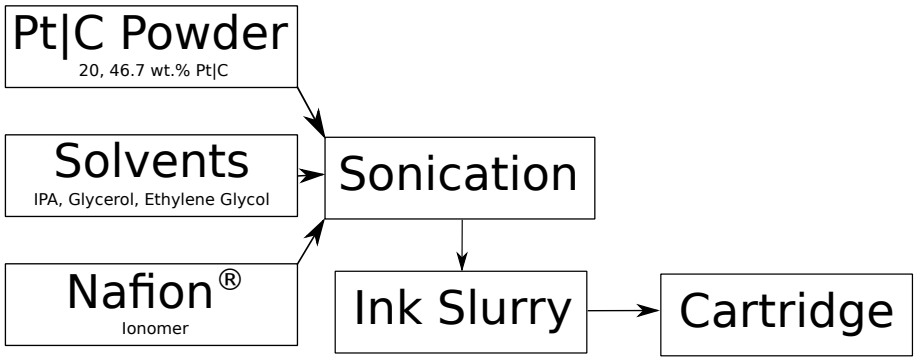

Figure 2.2 – Flow diagram of fabrication stages

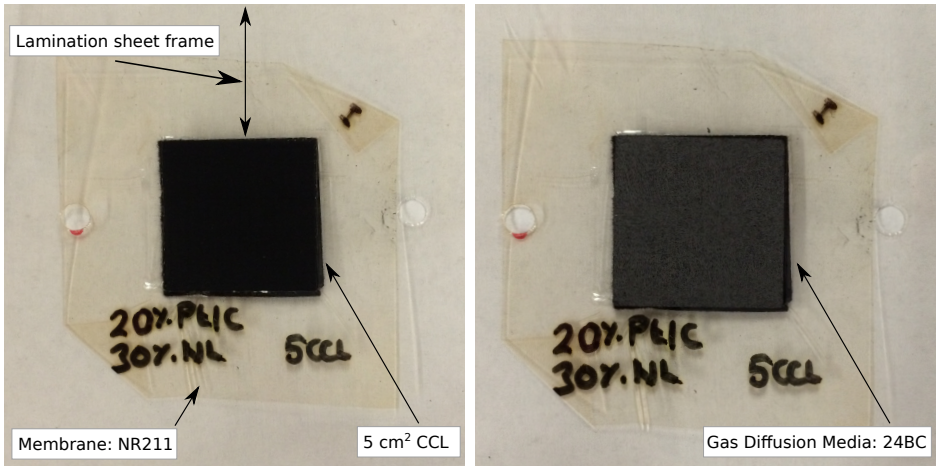

(a) Laminated CCM (b) Laminated MEA

Figure 2.3 – Laminated CCM with and without gas diffusion media layers.

When the CCM has fully dried it is then laminated using 76 μm thick lamination sheets. Lamination of the exterior membrane acts as a handling frame while also keeping the CCM flat and wrinkle free, as seen in Figure 2.3 (a). Figure 2.3 (b) shows the laminated CCM sandwiched between two gas diffusion media. The CCM and gas diffusion media sandwich is known as the membrane electrode assembly (MEA). Once the MEA has been formed it is now ready to place into the stack assembly.

2.2.2 PEFC Components, Stack Assembly, and Conditioning

2.2.2.1 PEFC Components and Hardware

A PEFC consists of several layers each with a specific role, namely, PEM, CLs, MPLs, GDLs and BPPs, as described in Section 1.1. In this work the PEM used is a Nafion® membrane NR211 (1,100 EW, H^+ form, Dupont™). The CLs consist of ionomer, and Pt on carbon support as described in Section 2.2.1. The CCM is sandwiched between two gas diffusion media forming the MEA which is then placed into the single stack assembly, as seen in Figure 2.4 (a).

There are two main types of gas diffusion media, *i.e.*, single or double layer. A single-layer consists of one anisotropic carbon fibrous layer impregnated with PTFE (GDL). A double-layer gas diffusion media consists of the anisotropic GDL and also a less porous isotropic layer (MPL) coated on one side, which is made of carbon black and impregnated with PTFE as binder. In this work, a 235 μm thick double-layer gas diffusion media is used for all samples (24BC, SIGRACET®), containing 5 wt.% PTFE in the GDL and 10 wt.% PTFE in the MPL. The 5 cm^2 gas diffusion media are placed on either side of the MEA with the MPL facing the CL.

The entire PEFC sandwich is then placed between two graphite BPPs and compressed in a multi/single stack assembly. The BPPs provide electronic conduction and are also used to supply reactant gas through flow channels. In this work the gas channels milled into the BPPs are a co-flow single pass serpentine flow field (0.8 mm x 0.8 mm), as seen in Figure 2.5 (a).

Once the cell is assembled, a Scribner Associates - 850e test station is used for testing of the CCM samples, as seen in Figure 2.5 (b). The test station controls the environment of the cell, *i.e.*, gas flow rates, humidity, temperature, and pressures on the anode and cathode side of the PEFC. During testing, the cell assembly is

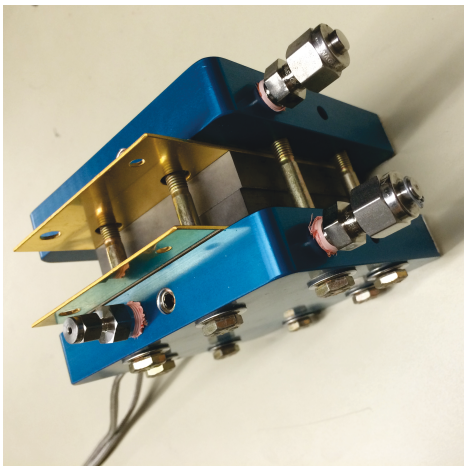

(a) Cell assembly

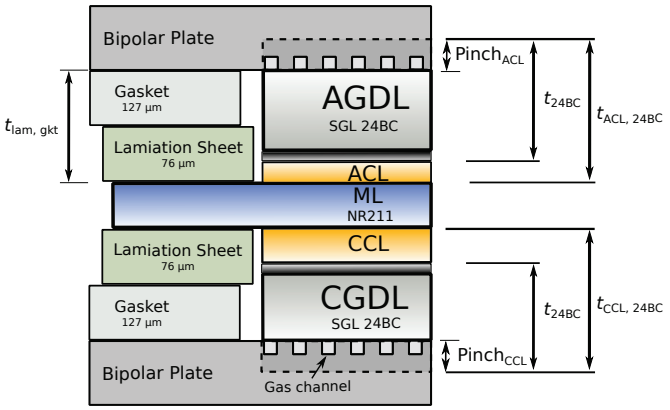

(b) Cell pinch

Figure 2.4 – Single stack assembly (a) with accompanied diagram illustrating cell pinch (b)

maintained at a constant temperature, while the feed gases dew point temperatures are varied to supply the desired relative humidity.

2.2.2.2 Stack Assembly

In this work, a screw compression, single cell stack assembly is used (Scribner Associates), as seen in Figure 2.4 (a). Compression of the cell is done to achieve two goals, apply sufficient pressure to ensure good inter-facial contact between layers (CCM-MPL, GDL-BPP) and to stop gas leakage to the environment. When compressing the cell it is important to avoid over-compression of the MEA.

Over-compression of the gas diffusion media would lead to significant reduction in reactant transport to the active CLs causing greater mass transport losses (lower limiting current) due to reduced diffusion and water transport [71]. In order to seal the assembly and to reduce the compression force on the gas diffusion media, 127 μm silicon gaskets are placed on either side of the laminated CCM giving the desired cell pinch, as shown in Figure 2.4 (b). Cell pinch is the compressive load on the active area of the CCM.

Pinch is calculated by taking the sum of the CL and gas diffusion media thickness ($t_{ACL,\,24BC}$ or $t_{CCL,\,24BC}$) and subtracting the thickness of the lamination sheet and gaskets ($t_{lam,\,gkt}$), as seen in Equation (2.1) and (2.2). The total cell pinch ($Pinch_{tot}$)

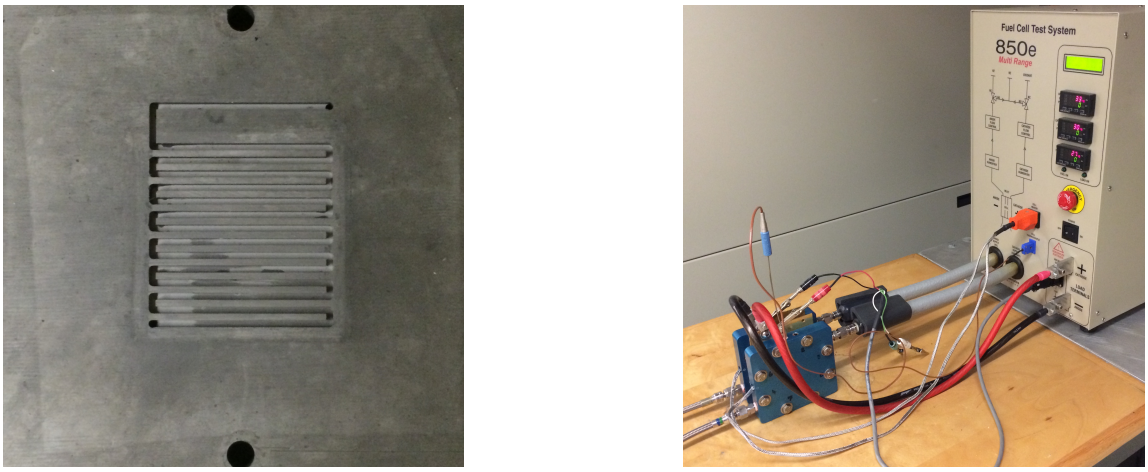

(a) (b)

Figure 2.5 – Graphite bipolar plate with serpentine flow channel (a) and Scribner Associates - 850e test station hardware (b)

is recommended to have a value of $\approx 100\ \mu m$ [71], which is found using Equation (2.3). In this study the total pinch has been calculated to lie between 67 - 73 μm depending on CL thickness, which is a property of the ink type and number of layers printed, as seen in Figure 4.2.

$$\text{Pinch}_{ACL} = t_{ACL,\,24BC} - t_{lam,\,gkt} \tag{2.1}$$

$$\text{Pinch}_{CCL} = t_{CCL,\,24BC} - t_{lam,\,gkt} \tag{2.2}$$

$$\text{Pinch}_{tot} = \text{Pinch}_{ACL} + \text{Pinch}_{CCL} \tag{2.3}$$

The assembly is compressed tightening each of the eight bolts, using a star-cross pattern to insure uniformity of pressure. In previous work, each bolt on the assembly was tightened to 7.34 $N \cdot m$ to reduce cell resistance. Compression was found to be excessive, as seen in Figure 2.6 (d), causing shearing of the GDL and intrusion of the lamination sheet into the gas channel, Figure 2.6 (e) and (f). As a result compression tests were carried out using Pressurex® paper to ensure adequate pressure along the channel and to see whether good sealing has been achieved. Figures 2.6 (a)-(c), shows the pressure analysis from 3.95 - 5.65 $N \cdot m$. The 3.95 $N \cdot m$ showed adequate sealing pressure but inadequate pressure along the top section of the serpentine channels, conversely the 5.65 $N \cdot m$ showing slightly excessive pressure. The optimal torque was found to lie between 5.08 - 5.65 $N \cdot m$. A value of 5.3 $N \cdot m$ was used in this study.

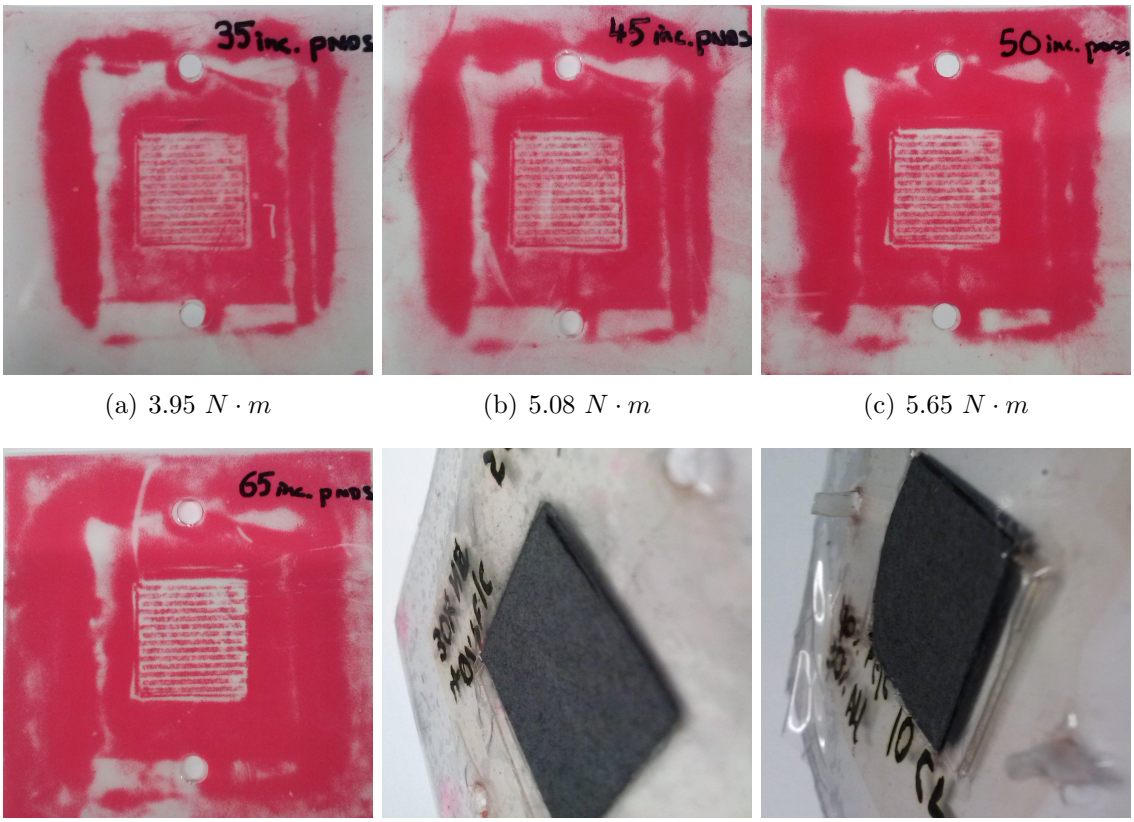

(a) 3.95 $N \cdot m$ (b) 5.08 $N \cdot m$ (c) 5.65 $N \cdot m$

(d) 7.34 $N \cdot m$ (e) 7.34 $N \cdot m$ (f) 7.34 $N \cdot m$

Figure 2.6 – Pressure analysis (a)-(d), GDL shearing (e), and lamination protrusion (f)

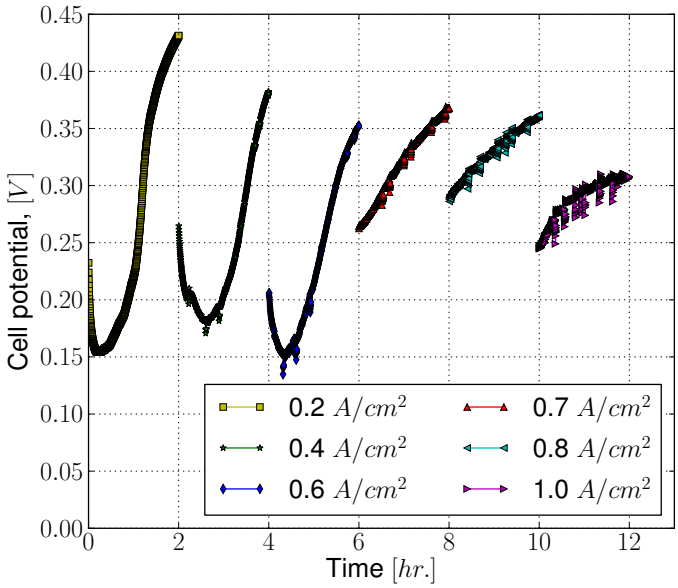

Figure 2.7 – Galvanostatic conditioning over a period of 13 hours, holding each current step for a period of 2 hours. Where the cell voltage is substantially increasing over the first several hours and less so in the later stages.

2.2.2.3 Conditioning

Conditioning is done holding constant current (galvanostatic) steps over a period of 13 hours. Current is varied from 0.1 to 1 A/cm^2 keeping a constant cell temperature of 80 °C, as seen in Figure 2.7. The cell is conditioned at 80% RH with hydrogen/air feed gas supplied through the anode/cathode flow fields at 0.2/0.4 *slpm* and atmospheric pressure. During this conditioning time several processes occur, *i.e.*, cell hydration, and flushing out trapped dust, all which increase the cells performance. This cell performance can be observed in Figure 2.7, where the cell voltage increases over time for a given current.

2.2.3 Ex-situ Characterization

2.2.3.1 SEM Characterization

There are two main objectives for imaging the CCMs, surface characterization and thickness analysis. The analysis will allow observations of the surface characteristics and thickness variation for the various ink types. The thickness values obtained are then utilized in the mathematical model.

To gain information on the thickness and surface characteristics, micrograph images were taken of the CCM surface and cross sections using a scanning electron microscope (SEM)(JEOL JSM-6301F, using 5,000 kV at 35 seconds per frame). Obtaining micrographs of the surface requires little preparation other than the fabrication and regular post processing of the CCM sample, however cross-sectional views require additional steps.

To prepare the cross-sectional specimens the samples were freeze fractured using liquid nitrogen. Freeze fracturing reduced damage on the desired surface, as the reduced temperature caused the membrane layer to cleanly fracture. If cut with a knife or scissors surface damage and alteration of the CCM thickness, due to local compression was observed.

Several CCMs were prepared varying the number of passes from 5 to 20 in 5 layer intervals. The analysis has been carried out using micrographs of $x1000$ and $x6000$ magnification. Thickness values are obtained by averaging over 100 thicknesses per sample to insure accurate representation of the CCMs, achieved using *ImageJ* [72] imaging processing functionality. The results from this analysis can be found in Section 4.1.1, showing both thickness results and SEM imaging.

2.2.4 In-situ Characterization

2.2.4.1 Cell Resistances

During cell operation resistive losses occur due to proton and electron flux through the fuel cell materials as well as contact resistance between the sandwiched layers. In this section the electronic and contact resistance ($R_{e^-} + R_{contact}$) losses are investigated, using the same methodology as Neyerlin et al. [73]. Neyerlin et al. used a power supply to pass 1.0 A/cm^2 through the assembly, the voltage drop across the cell is then determined according to Ohm's law.

Achieving this requires a conducting circuit, however the stack assembly as seen before is designed to insulate the anode side from the cathode. To obtain the conducting circuit when assembling the stack, all the components except the CCM (ACL, ML, CCL) are present. Note this method does not include resistance due to MPL-CL interfaces. The assembly consists of two 76 μm lamination sheets, two 127 μm gaskets, and two 24BC gas diffusion media with the MPLs facing each other.

Protonic resistance is achieved subtracting the electronic and contact resistance from the total internal cell resistance (iR). The iR of the PEFC is obtained using a current interrupt, a method inbuilt into the Scribner 850e test station. iR is the total resistance due to contact, electronic, and protonic (R_{H^+}) resistance.

$$iR = R_{e^-} + R_{contact} + R_{H^+} \tag{2.4}$$

iR is achieved using the following steps ten times a second. The cell voltage and current are measured during operation (V_{T0} and I_{T0}), the current is then removed. A short period after the current has been removed the voltage is then measured again (V_{T1}), once this has been done the current is reapplied to the cell. Using the obtained values Equation (2.5) is then used to calculation the internal cell resistance,

$$iR = \frac{(V_{T1} - V_{T0})}{I_{T0}} \tag{2.5}$$

The results from this study are shown in Section 4.1.2.2.

2.2.4.2 Fuel Crossover

Crossover is caused by diffusion of hydrogen from the anode to the cathode through the membrane and through pin holes in the PEM due to damage. Reactant crossover can cause degradation of the cell, reduction of open cell voltage, and reduced fuel efficiency. In addition the oxidant can also cross the membrane barrier by similar mechanisms. The direct reaction between H_2 and O_2 at the cathode produce peroxide radicals, which can degrade the cell by attacking the membrane and catalyst layer [74].

Crossover tests are used to insure the cell has not incurred excesses damage, and the polarization curve is an accurate representation of the cells performance. To experimentally characterize the crossover an inert gas, *i.e.*, N_2, is purged on the cathode side of the cell, 0.7 *slpm* at 100% RH. Hydrogen is passed through the anode, 0.2 *slpm* at 100% RH. Once the cell voltage has dropped below 0.1 V to ensure O_2 has been removed from the ionomer, the inert gas flow is stopped and the crossover test is performed.

The crossover test is done by fixing the potential at the pseudo-reference electrode (anode), while the working electrode (cathode) undergoes a linear potential sweep. This type of voltage sweep is refereed to as a linear sweep voltammetry (LSV) experiment. In this work the potential is increased from 0.1 - 0.5 V in 0.1 V increments,

each step lasting a duration of 200 seconds, as seen in Figure 2.8. By recording the electrode current vs. working electrode potential it is possible to obtain the hydrogen crossover flux using Faraday's law, *i.e.*,

$$J_{H_2}^{cross} = \frac{I_{H_2}^{cross}}{n \times F \times A} \tag{2.6}$$

where it is assumed that H_2 molecules that have crossed over from the anode to the cathode are completely oxidized. Figure 2.8 (a) shows the typical results of a pristine cell, whereby the voltage is increased in steps over time, as seen in Figure 2.8 (c) while current remains constant. This is not the case for a degraded cell Figure 2.8 (b) where as the voltage is increased the current is also seen to increase. This is generally the result of pin holes in the membrane which have been introduced due to improper handling. Results for the average crossover for several layers used in this work can be found in Section 4.1.2.

2.2.4.3 Electrochemical Surface Area

For a Pt site to be active in the CL, it requires access to electrons (e^-), protons (H^+), and oxygen (O_2). Electronic conductivity from the Pt site to the conducting plate is provided by the Pt carbon support network, while the proton conduction across the layer is supported through the ionomer. The third requirement during fuel cell operation is access to O_2, however for an electrochemical surface area (ECSA) characterization this is not required as only the adsorption and desorption of H_2 onto the Pt sites are recorded.

If the Pt site is missing one of these two connection pathways, the Pt will be inactive and will not be in the electrochemical reaction processes, thereby reducing the electrode ECSA. Inactive Pt is highly undesirable, therefore the higher the ECSA the more effective the cell.

It is possible to obtain the ECSA by recording the total charge required for complete monolayer-adsorption/desorption of H_2 onto the Pt sites. Characterization of the ECSA is obtained by cyclic voltammetry (CV) where the voltage is cycled so that the adsorption-limited charge transfer reactions can be recorded. In this work, the hydrogen adsorption/desorption (HAD) reactions are used to characterize the ECSA of the catalyst layer, *i.e.*,

$$Pt + H^+ + e^- \leftrightarrow Pt - H_{ads} \tag{2.7}$$

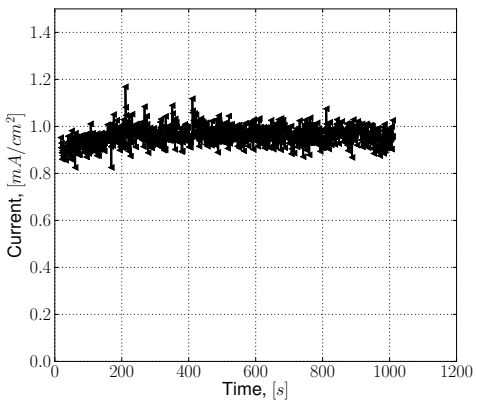

(a) Pristine cell

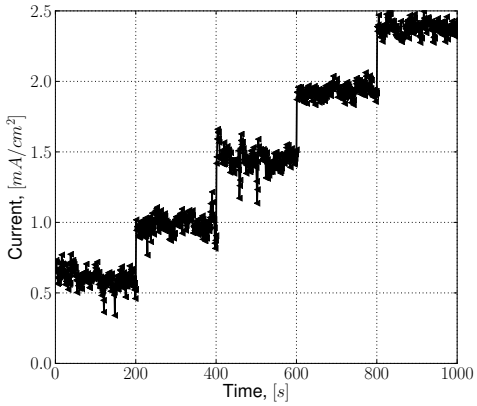

(b) Degraded cell

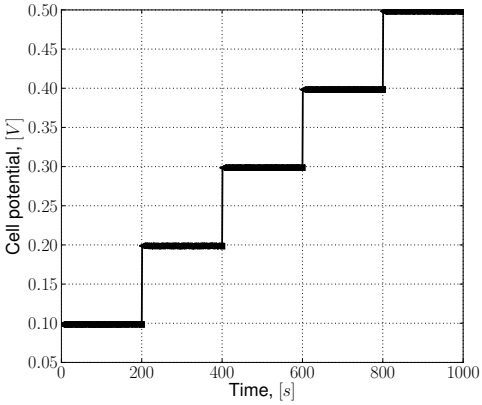

(c) Potential steps

Figure 2.8 – Crossover analysis of a pristine (a) and a degraded cell (b), as the potential is increased over time (c). Here the pristine remains at a constant current, however the degraded cell increases in current with potential.

Before beginning the CV analysis the cell and gas temperatures are reduced to 30 °C. The cathode side (working electrode) of the CCM is purged (0.8 $slpm$) with an inert gas, in this work nitrogen (N_2) is used at 100 % RH. The purging process is done over several hours to ensure no reactants from previous tests remain dissolved in the ionomer, which if not removed, could alter the results. On the anode side (pseudo-reference electrode) of the CCM, hydrogen flows at 0.2 $slpm$ and 100% RH. Once the cell voltage has dropped below 0.1 V, this indicates that all reactants have been removed from the working electrode. Flow on the working electrode (cathode) side is then stopped and the CV analysis can begin. Research has shown that maintaining a flow rate on the anode side produces more accurate CV results [75]. However, as our humidification system is done by a bubble humidifier and the water in the humidifier might contain dissolved O_2, it is preferred to run with no flow, reducing the influx of O_2 dissolved in the humidifier.

The CV analysis is carried out using a voltage linear sweep (40 mV/s) from 0.8 to 0.07 V. When the voltage has returned to 0.8 V the cycle is then repeated for a total of 10 times, averaging of the ten sweeps is then used for the analysis. During the cathodic voltage sweep (0.8 to 0.07 V) the electrochemical reduction of protons takes place. This leads to the adsorption of protons onto the Pt surfaces. As the voltage reaches 0.07 V the adsorbed protons then begin to leave the surface as they combine to form H_2 in the hydrogen evolution reaction (HER). HER is undesired as it frees up Pt sites for additional adsorption giving the illusion of more Pt reaction sites than are actually available. Therefore when calculating the ECSA only values between 0.1 and 0.4 V are considered, as seen in Figure 2.9. On the return anodic voltage sweep (0.07 to 0.8 V), the charge transfer due to desorption of protons off the Pt sites is recoded.

Equation (2.9) is used to obtain the ECSA of the Pt catalyst [76]. For Pt catalysts, 210 $\mu C/cm^2_{Pt}$ is the commonly assumed charge released when hydrogen molecules fully cover a cm^2 of Pt surface [77, 78].

$$ECSA\left(\frac{cm^2_{Pt}}{g_{Pt}}\right) = \frac{charge\ (C/cm^2)}{210\ (\mu C/cm^2_{Pt}) \times \text{Electrode loading}\ (g_{Pt}/cm^2)} \tag{2.8}$$

An example CV curve of a 5 cm^2 cell can be seen in Figure 2.9, using a scan rate of 40 mV. In order to calculate the ECSA the CV data must first be translated onto the x-axis. The curve is offset due to hydrogen crossover, which causes the centre-line of the CV curve to displace in the positive y-direction on the graph, as seen in

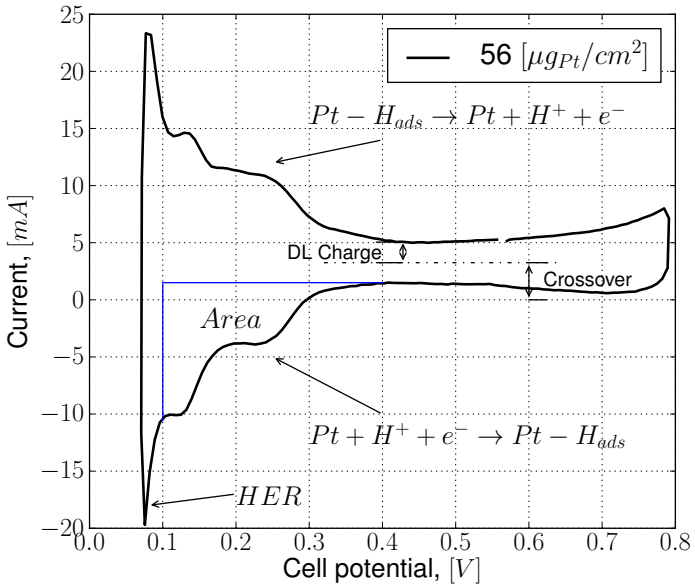

Figure 2.9 – Cyclic voltammetry used to calculate ECSA of CL. Lower half of graph shows hydrogen being adsorbed onto the surface, while the top half shows H_2 desorption. DL charge causes the CV curve to show current even when there are no reactions, while crossover causes the CV centre line to be displaced in the positive y axis.

Figure 2.9. In addition double-layer (DL) charge effects are observed between 0.4 - 0.6 V causing the the CV curve to be displaced symmetrically on both sides of CV centre-line. DL charge causes the CV curve to show current even when there are no reactions. To counteract the DL charge we begin the ECSA calculation at 0.4 V where Faradaic processes are no longer present [77]. Once the DL effects have been accounted for it is now possible to integrate the area under the reduction half of the curve shown in Figure 2.9 by the region marked as '*Area*'. Dividing the charge term by the scan rate in order to convert the numerator in Equation (2.9) to mA/cm^2. The area under the CV curve can now be used to calculate the ECSA.

$$ECSA\left(\frac{m_{Pt}^2}{g_{Pt}}\right) = \frac{Area\ (mA/cm^2 \times V)}{0.21\ (mC/cm_{Pt}^2) \times \text{Scan rate}\ (V/s) \times \text{Electrode loading}\ (g_{Pt}/cm^2)} \times 10^{-4}$$

Data showing the ten sweeps of the CV analysis can be observed in Figure 2.10, where the 'Area' region increases with increasing Pt content.

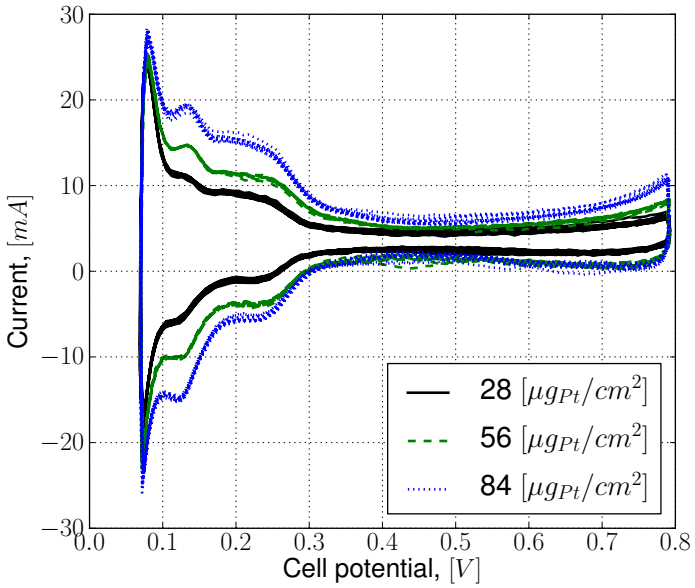

Figure 2.10 – EG ink CV plot versus Pt loading between 28 and 84 $\mu g_{Pt}/cm^2$, at 40 mV/s scan rate. Showing the increase in H^+ adsorption and desorption with increasing Pt content.

2.2.5 Electrochemical Performance Characterization

As mentioned in Chapter 1, the performance of an electrochemical device is quantified by plotting the current density (I) against the cell potential (V). This type of plot is known as a polarization curve or I-V curve for short. To characterize the fuel cells I-V curve, a Scribner Associates - 850e test station is used, supplying '*Ultra-high purity*' hydrogen at the anode side, and compressed air (21% O_2 in N_2) or N_2-O_2 mixtures with various partial pressures of O_2 (1%, 10%, 100%) are supplied on the cathode side. The flow rates during testing for the anode and cathode are 0.2 and 0.4 *slpm* respectively. The cells are operated at ambient pressure and constant cell temperature of 80 °C. The fuel cell is characterize at three RH values, *i.e.*, 50, 70, and 90%. The relative humidity is controlled by altering the dew point of the supplied gases.

At each RH testing begins holding the OCV for 5 minutes. The polarization curve is then obtained using galvanostatic intervals of 20 mA/cm^2, maintaining each point for 60 seconds before recording the value. At increasing current steps, the voltage gradually decreases, mapping out the kinetic, ohmic, and, mass transport region of the polarization curve. Once the cell voltage has dropped below 0.22 V, the process is

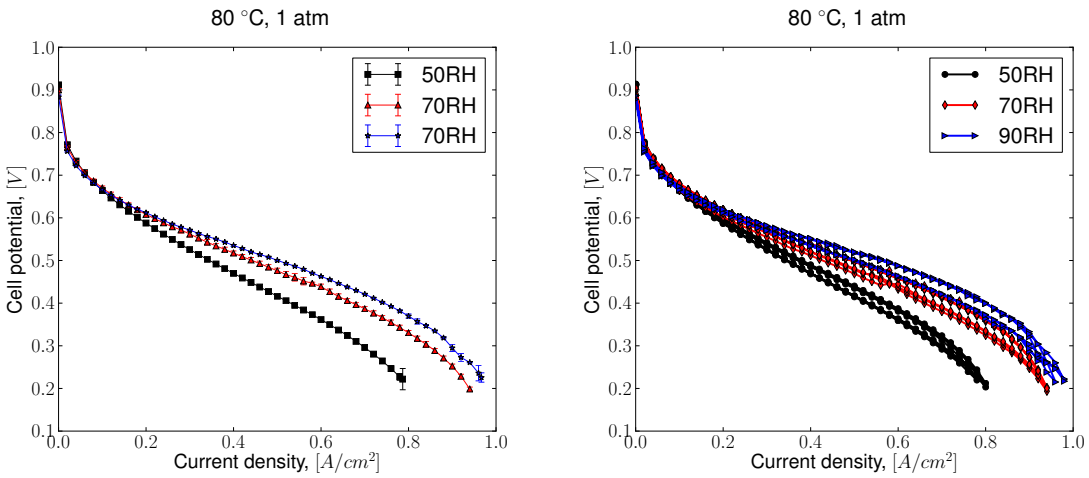

(a) (b)

Figure 2.11 – Experimental polarization curves for forward averaged sweeps (a) and also the raw data showing forward and backward sweeps. The STDEV seen in (a) represents the change between forward sweeps only.

reversed until OCV. This full cycle is referred to as one full sweep. Three full sweeps are taken for each RH (3 forward and 3 backward). Before the next relative humidity is tested there is a 30 minute interval in order for the cell to acclimatize to the new humidification, the 5 minute OCV is then started and polarization sweeps begin.

Plotting the I-V curve is typically done by taking an average of only the forward sweeps. Forward sweeps are thought to represent the true performance of a fuel cell as backward sweeps overstate fuel cell performance. This is a result of additional hydration at higher currents, which lowers ohmic losses. Figure 2.11 (a) shows the average data and STDEV for forward sweep only. It can be seen that there is little to no variation between forward sweeps. Figure 2.11 (b) shows the hysteresis between the forward and backward sweeps for the different RH values. Throughout this work only the averaged forward sweeps will be considered for comparisons.

2.3 Functionally Graded Electrodes

In this work, functionally graded CLs have also been examined. When fabricating functionally graded CLs all stages of the procedure are the exact same as when producing a homogeneous CL, with one additional drying stage. Fabricating a ho-

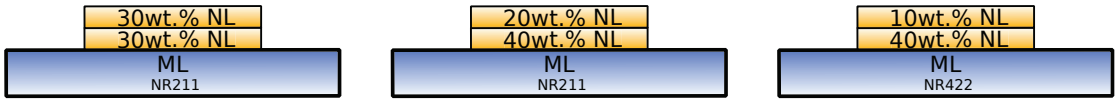

(a) ML|30|30 (b) ML|40|20 (c) ML|20|40

Figure 2.12 – Homogeneous CCL with 30 wt.% ionomer loading (a) and two functionally graded CCLs, one with an inner layer of 40 wt.% ionomer and an outer layer of 20 wt.% ionomer (b), and the second with the inverse (c)

mogeneous CL requires only one ink composition. However, to achieve functionally graded CLs two inks are formulated, varying in either wt.% Pt|C, and/or ionomer wt.%. In this work the functionally graded ionomer electrodes have been fabricated using NR211 for the PEM and CCLs with 20 wt.% Pt|C (Vulcan XC-72 carbon black HiSPEC™ 3000).

When fabricating functionally graded CLs the first ink is formulated and is used to deposit the desired number of inkjet passes onto the substrate to create the first inner CL. In this work 5 passes are done. The CCM is then placed into an over to dry for 24 hours. Once the CCM is fully dried the second ink is prepared and deposited to form the second outer CL, in this work the second layer also consists of 5 printer passes. The intermediate drying stage is done to ensure two distinct CLs are achieved.

Figure 2.12 (a) shows a homogeneous CL with 30 wt.% ionomer loading. Figure 2.12 (b) shows a functionally graded CL, having an inner layer of 40 wt.% ionomer and an outer layer of 20 wt.% ionomer (ML|40|20), while Figure 2.12 (c) shows the second type of graded cell in this work having the inverse of the first (ML|20|40).

Chapter 3

PEFC Mathematical Model

3.1 Membrane Electrode Assembly Model

In order to develop the fuel cell governing equations a mass balance for each species and an energy balance are performed to predict the concentration of each reactant, electrical potential, electrolyte potential, water in the membrane, and temperature. The governing equations are all solved inside a two-dimensional, through-the-channel MEA configuration. Section 3.1.1, shows the basic mass and energy balances, while the remaining sections discuss the flux expressions and source terms.

3.1.1 Mass and Energy Conservation

The fuel cell system of governing equations is achieved by performing a mass balance for each species and an energy balance over an infinitesimal control volume in each layer. An example of this for the mass balance of species i is shown as:

$$\frac{\partial c_i}{\partial t} + \nabla \cdot N_i = S_i \tag{3.1}$$

where $\frac{\partial c_i}{\partial t}$ is the concentration change of species i over time. As this is a steady state model the time dependant term is equal to zero ($\frac{\partial c_i}{\partial t} = 0$), c_i is the molar concentration of species i, N_i is the volumetric molar flux of species i, and S_i is the volumetric source term. The energy balance can be found in Section 3.1.5 or for a more detailed derivation in [17].

The flux of each one of species will be discussed in the following sections. There are three types of source terms considered. S_λ which refers to the adsorption and desorption of water in the membrane, as discussed in Section: 3.1.7. This source term will couple the water content equations and ensure equilibrium between the sorbed water content in the membrane and the water vapour in the gases. The second type

of source terms (reaction source terms) will relate the species production and consumption, due to the electrochemical reactions in the ACL and CCL. The third type relates the thermal energy transfer and production throughout the PEFC assembly.

For a single phase through-the-channel non-isothermal MEA model these six governing equations are given as:

$$\begin{aligned}
\vec{\nabla} \cdot \vec{N}_{O_2} &= S_{O_2} \\
\vec{\nabla} \cdot \vec{N}_{H_2O} &= S_{H_2O} + S_\lambda \\
\vec{\nabla} \cdot \vec{N}_{H^+} &= S_{H^+} \\
\vec{\nabla} \cdot \vec{N}_{e^-} &= S_{e^-} \\
\vec{\nabla} \cdot \vec{N}_\lambda &= -S_\lambda \\
-\vec{\nabla} \cdot \left(k^{eff} \vec{\nabla} T \right) + \sum_{\text{gases},\lambda} \left(\vec{N}_i \cdot \vec{\nabla} \bar{H}_i \right) &= S_T
\end{aligned} \tag{3.2}$$

the respective flux terms ($\vec{N}_i$) and source terms (S_i) will now be developed in more detail in the subsequent sections.

3.1.2 Gaseous Species Transport

3.1.2.1 Assumptions

1. Feed gas of the cathode flow channel is humidified air, *i.e.*, mixture of oxygen, water vapour, and nitrogen.
2. Feed gas of the anode flow channel is pure humidified hydrogen, *i.e.*, hydrogen and water vapour.
3. The reactant gases contain no impurities.
4. All gas species behave as ideal gases ($PV = nRT$).
5. There are no convective flow gas transport effects.
6. Negligible concentration and pressure drop along the channel.
7. Negligible crossover of reactants through the membrane
8. Oxygen and water vapour are considered dilute species in nitrogen (characterize by Fick's law).
9. Water vapour is considered a dilute species in hydrogen (characterize by Fick's law).

10. GDL is an anisotropic network of carbon fibres with pore space.

11. MPL is considered to be a isotropic mixture of solid conductive material with pore space.

12. CCL is a isotropic mixture of solid and ionomer materials with pore space.

3.1.2.2 Reactant Flux

Successful operation of the PEFC requires the ability for reactants (O_2/H_2) to reach the reaction sites. In this model, the gas is assumed to travel from the edge of the channel through the GDL, MPL, and into the CL by diffusion only. The geometry of the model represents a parallel flow channel configuration (Figure 4.22) with high stoichiometry, where it is assumed no concentration changes along the channel with low pressure drops and no inter-channel pressure gradients. Thereby allowing these effects to be neglected [79]. In reality, concentration gradients and convective effects are present due to limited flow velocities and pressure gradients across the cell.

At the cathode gas channel humidified air (O_2, N_2, water vapour) is supplied to the channel, while at the anode humidified hydrogen (H_2, water vapour) is supplied. To express the oxygen flux a multi-component mixture (Maxwell-Stefan [80]) equation would typically be used. In this work, due to the high nitrogen molar fraction (0.79) in air and in order to reduce the non-linearity of the system of equations an isobaric infinitely dilute solution is assumed. Therefore, the Maxwell-Stefan equation simplifies to Fick's equation [79]:

$$N_i = -c_g D_{i,j}^{eff} \nabla c_i \tag{3.3}$$

where N_i is the molar flux, $D_{i,j}^{eff}$ is the effective diffusion of a gas i with respect to gas j, and c_i representing the concentration gradient of the gas i. Using Fick's law, the molar flux of oxygen and water vapour in the cathode side of the cell can be represented as:

$$N_{O_2} = -c_g D_{O_2,N_2}^{eff} \nabla x_{O_2} \tag{3.4}$$

$$N_{H_2O} = -c_g D_{H_2O,N_2}^{eff} \nabla x_{H_2O} \tag{3.5}$$

Applying the same procedure to the anode side of the cell and assuming H_2 as the solvent, the water vapour flux is:

$$N_{H_2O} = -c_g D_{H_2O,H_2}^{eff} \nabla x_{H_2O} \tag{3.6}$$

In the fuel cell model the system of equations are being solved over multiple domains

each consisting of different porosity, and as a result, each have different effective diffusivity and conductivities.

For the CLs, there are several expressions available to compute effective diffusivity, however, the most common in fuel cell modelling is the Bruggemann's relation [81]. Using the Bruggemann equation would incur erroneous assumptions as mentioned by Secanell [79] and also result in gas transport even for infinitely small void volume fractions (pores), this however is not the case. It has been shown that there is a minimum volume fraction necessary to form a percolation network [79, 82]. Therefore, the effective gas diffusion coefficient is determined using percolation theory [79],

$$D_{i,j}^{eff} = D_{i,j} \left(\frac{\varepsilon - \varepsilon^{th}}{1 - \varepsilon^{th}} \right)^{\mu} \Theta \left(\varepsilon - \varepsilon^{th} \right) \tag{3.7}$$

where $D_{i,j}$ is the bulk gas diffusivity of gas i with respect to the abundant gas j, ε is the void fraction, ε_{th} is the porosity threshold, and μ is a '*universal*' constant which is dependant on the fibre orientation. It is understood that for two dimensions $\mu = 1.3$ and for three dimensions $\mu = 2$ [79, 82, 83]. As μ is a universal constant, in this work it has been kept at a constant value of $\mu = 2$ as the CL is a three-dimensional lattice [79, 82, 83]. In order to capture the threshold below which no diffusion will occur the Heaviside step function is utilized,

$$\Theta(\varepsilon - \varepsilon^{th}) = \begin{cases} 0 \text{ for } (\varepsilon - \varepsilon^{th}) < 0 \\ 1 \text{ for } (\varepsilon - \varepsilon^{th}) \geq 0 \end{cases} \tag{3.8}$$

In this work the porosity threshold ε_{th} for the ACL and CCL have been fitted to experimental data obtained by Yu et al. [2] for CL of varying porosity, I/C Ratios, and carbon supports. To fit to the experimental data a least squares fit method was performed, resulting in a porosity threshold of 0.259. The results of this μ and fitted ε_{th} value are plotted against the experimental data in Figure 3.1. This fit is considered sufficient as it is in close agreement with the experimental data. In reality the experimental PEFCs being compared to in this work might not have the exact same porosity or effective diffusion relationship, however, this comparison shows that the effective diffusion are representative of actual physical CL properties.

The micro-structures of MPLs and CLs are considered to be isotropic in nature having effective diffusion values for in-plane and through-plane to be equal, and so can be describe using the percolation Equation (3.7). However, this is not the case

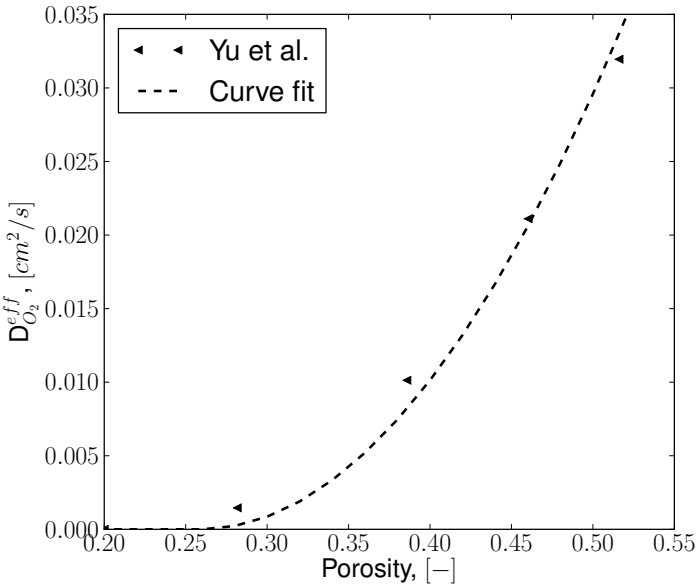

Figure 3.1 – Curve fit of the effective oxygen diffusion coefficient to Yu et al. [2] experimentally observed data in electrodes of varying porosity, I/C Ratio, and carbon supports

for the GDLs as they have random anisotropic fibre arrangements. Tomadakis and Sotirchos [84] used numerical Monte Carlo simulations to propose a new expression for predicting the effective diffusivity in fibrous porous media:

$$D_{g,j}^{eff} = D_{g,j}\ \varepsilon \left(\frac{\varepsilon - \varepsilon^{th}}{1 - \varepsilon^{th}} \right)^{\mu^i} \Theta\left(\varepsilon - \varepsilon^{th}\right) \tag{3.9}$$

where $D_{g,j}^{eff}$ and $D_{g,j}$ are the effective and bulk gas diffusivity of gas g in the abundant gas j, and μ^i is the i^{th} direction for either in-plane or through-plane. This expression is used in the GDL in this work.

3.1.3 Charged Species Transport

3.1.3.1 Assumptions

1. Protons are only conducted through the electrolyte phase (Nafion®), and its transport is governed by Ohm's law.

2. Ionomer has sufficient homogeneously distributed anionic groups assuming a constant concentration of protons.

3. Electrons are only conducted through the solid phase (Pt, carbon), and its transport is governed by Ohm's law

3.1.3.2 Electron Flux

The movement of electrons (e^-) through the PEFC occurs in the solid (Pt, carbon) phase. This electron flux is governed by Ohm's law [79]:

$$\vec{N}_{e^-} = -\frac{\sigma_s^{eff}}{z_{e^-}F}\vec{\nabla}\phi_s \;=\; \frac{\sigma_s^{eff}}{F}\vec{\nabla}\phi_s \tag{3.10}$$

where σ_s^{eff} is the effective electron conductivity of the layer, z_{e^-} represents the charge of an electron (-1), and ϕ_s is the solid electrical potential. To capture the effective transportation of electrons through the CL, MPL, and GDL percolation theory is used. The effective electronic conductivity, σ_S^{eff}, is expressed by [79, 82, 83]:

$$\sigma_S^{eff} = \sigma_S \left(\frac{\varepsilon_S - \varepsilon_{th}}{1 - \varepsilon_{th}}\right)^{\mu} \theta(\varepsilon_S - \varepsilon_{th}) \tag{3.11}$$

where σ_S is the electronic conductivity of a pure conductor material, ε_S is the volume fraction of the conductive material, ε^{th} is the percolation threshold, and μ is the universal exponent. Further detailed descriptions of this expression can be found in the following reference [79], and will not be discussed further.

3.1.3.3 Proton Flux

Proton flux in a polymer electrolyte with fixed charges can be expressed using Ohm's law [85]:

$$\vec{N}_{H^+} = -\frac{\sigma_m^{eff}}{z_{H^+}F}\vec{\nabla}\phi_m = -\frac{\sigma_m^{eff}}{F}\vec{\nabla}\phi_m \tag{3.12}$$

where z_{H^+} represents the charge of a proton ($+1$), and σ_m^{eff} is the effective proton conductivity of the porous CL structure.

Proton conductivity has been shown to have a dependence on both sorbed water content (λ) in the membrane, and temperature (T). Conductivity increases with increasing humidification and temperature [86].

In this work, data published by Iden et al. [87] is used to estimate effective CL proton conductivity which has been characterized for varying Nafion® loadings, relative humidity, and carbon support. Utilizing this work, it is now possible to capture

proton conductivity for a range of Nafion® loadings. Fitting to the experimental work resulted in a third order polynomial expression:

$$\sigma_m^{eff} = \varepsilon_N^{1.6} \left(1.93 \times 10^{-7}\omega^3 - 6.735 \times 10^{-6}\omega^2 + 0.00075\omega - 0.008\right) e^{751.54\left(\frac{1}{353} - \frac{1}{T}\right)} \tag{3.13}$$

where ε_N is the electrolyte volume fraction, T is the temperature in Kelvin, and ω is defined as:

$$\omega = \begin{cases} 100\left(0.000094\lambda^3 - 0.00865\lambda^2 + 0.1832\lambda - 0.1254\right) & \text{for } \lambda < 13 \\ 100 & \text{otherwise} \end{cases} \tag{3.14}$$

For the bulk proton conductivity in the membrane layer, experimental values observed for Nafion® NR211 [88, 89] are used. This relationship was previously implemented by Dobson et al. [90].

$$\sigma_m = \left(-1.0125 \times 10^{-4}\lambda^2 + 0.01052\lambda - 0.020634\right) e^{751.5412\left(\frac{1}{303} - \frac{1}{T}\right)} \tag{3.15}$$

3.1.4 Sorbed Water Content and Transport

In a PEFC, there exists three forms of water in the catalyst layer, *i.e.*, water vapour in the catalyst layer pores, liquid water, and also sorbed water in the ionomer. In this mathematical model, it is assumed that only sorbed water and water vapour exist and that liquid water does not. This single phase assumption might lead to super-saturation (RH $\geqslant 100\%$). If this occurs the model will no longer be valid.

As seen in the previous section membrane water content can have effects on local relative humidity, and proton conductivity. In addition the membrane water content can also have an effect on the water movement inside the membrane which will now be discussed.

3.1.4.1 Assumptions

1. Vapour equilibrium membrane, *i.e.*, $n_{drag} = 1$
2. Only two species are transported in membrane, *i.e.*, water and protons.
3. The membrane is impermeable to gas and electron transport.
4. No liquid water is present in any layer of the MEA, *i.e.*, only water vapour and sorbed water
5. Convective transport is neglected

3.1.4.2 Membrane Water Transport

The amount of sorbed water in the membrane is defined by λ [86]:

$$\lambda = \frac{c_{H_2O}}{c_{SO_3^-}} \tag{3.16}$$

where c_{H_2O} is the concentration of water molecules, $c_{SO_3^-}$ is the mole concentration of sulfonic groups in the membrane which can be found using the equivalent weight,

$$c_{SO_3^-} = \frac{\rho_{m,\,dry}}{EW} \tag{3.17}$$

where $\rho_{m,\,dry}$ is the dry membrane density.

There are three modes of water transport in the membrane during fuel cell operation: electro-osmotic drag, diffusive flux, and thermal diffusion flux. Increasing the amount of adsorbed water in the membrane effects the overall water movement. Combining all three sorbed water flux terms inside the electrolyte gives the following expression [17]:

$$\vec{N}_\lambda = \underbrace{-n_{drag}\frac{\sigma_m^{eff}}{F}\vec{\nabla}\phi_m}_{\text{Electro-osmotic drag}} \underbrace{-\frac{\rho_{m,\,dry}}{EW}D_\lambda^{eff}\vec{\nabla}\lambda}_{H_2O\text{ Diffusion}} \underbrace{-\frac{D_T^{eff}}{M_{H_2O}}\vec{\nabla}T}_{\text{Thermal-osmosis}} \tag{3.18}$$

where n_{drag} is constant and is equal to 1 [91, 92] for a vapour-equilibriated membrane, which has also been considered in this work and previous works using this model [14, 17].

3.1.5 Thermal Transport

3.1.5.1 Assumptions

1. Heat generation due to viscous dissipation is neglected
2. Pressure gradients are negligible
3. Negligible dissolution energy of H_2/O_2 in the polymer electrolyte

3.1.5.2 Thermal Transport Equations

In PEFCs thermal transport occurs due to three phenomena, *i.e.*, convection, diffusion, and conduction. Bhaiya [17] implemented a non-isothermal model in OpenFCST

and conducted an order of magnitude analysis on each mode of thermal transport phenomena. Bhaiya found that the thermal transport due to convection was negligible, and simplified the thermal transport equation to:

$$\vec{\nabla} \cdot \left(k^{eff} \vec{\nabla} T \right) - \vec{\nabla} \cdot \left(\sum \bar{H}_i \vec{N}_i \right) + S_{heat} - \dot{W}_{electrical} = 0 \tag{3.19}$$

where k^{eff} is the effective thermal conductivity as defined in [17], $\bar{H}_i$ and $\vec{N}_i$ is the Molar enthalpy and the effective molar flux of specie i, S_{heat} and $\dot{W}$ are volumetric rates of heat production and work done by the system.

Thermal conduction is represented in the first term on the left hand side expressing heat transport due to Fourier conduction, the second term corresponds to enthalpy transport due to inter-diffusion. The third term S_{heat}, accounts for the irreversible heat generation associated with the electro-chemical reaction and $\dot{W}_{electrical}$ accounts for the electrical work done by the cell. In this model only certain thermal properties are accounted for in each layer. For example only heat generation occurs inside the CCL and ACL where the electrochemical reactions take place. For this reason Bhaiya implemented layer-specific thermal transport equations.

These layer specific equations describe the thermal transport in the cathode GDL|MPL (Equation (3.20)), anode GDL|MPL (Equation (3.21)), membrane layer (Equation (3.22)), cathode and anode CLs (Equation (3.23) and (3.24)) [17].

Cathode GDL|MPL

$$\underbrace{\vec{\nabla} \cdot \left(k^{eff} \vec{\nabla} T \right)}_{\text{Thermal Conductivity}} + \underbrace{D^{eff}_{O_2,N_2} \frac{p_T}{RT} \left(\frac{\partial \bar{H}_{O_2}}{\partial T} - \frac{\partial \bar{H}_{N_2}}{\partial T} \right) \vec{\nabla} T \cdot \vec{\nabla} x_{O_2}}_{\text{Thermal inter-diffusion transport } O_2 \text{ in } N_2}$$
$$+ \underbrace{D^{eff}_{H_2O,N_2} \frac{p_T}{RT} \left(\frac{\partial \bar{H}_{H_2O}}{\partial T} - \frac{\partial \bar{H}_{N_2}}{\partial T} \right) \vec{\nabla} T \cdot \vec{\nabla} x_{H_2O}}_{\text{Thermal inter-diffusion transport } H_2O \text{ in } N_2} + \underbrace{S_{e^-_{Ohmic}}}_{\text{Ohmic Heating}} = 0 \ . \tag{3.20}$$

Anode GDL|MPL

$$\underbrace{\vec{\nabla} \cdot \left(k^{eff} \vec{\nabla} T \right)}_{\text{Thermal Conductivity}} + \underbrace{D^{eff}_{H_2O,H_2} \frac{p_T}{RT} \left(\frac{\partial \bar{H}_{H_2O}}{\partial T} - \frac{\partial \bar{H}_{H_2}}{\partial T} \right) \vec{\nabla} T \cdot \vec{\nabla} x_{H_2O}}_{\text{Thermal inter-diffusion transport } H_2O \text{ in } H_2} + \underbrace{S_{e^-_{Ohmic}}}_{\text{Ohmic Heating}} = 0 \ . \tag{3.21}$$

Membrane Layer

$$\underbrace{\vec{\nabla}\cdot\left(k^{eff}\vec{\nabla}T\right)}_{\text{Thermal Conductivity}} + \underbrace{\frac{n_{drag}\ \sigma_m^{eff}}{F}\frac{\partial\bar{H}_\lambda}{\partial T}\vec{\nabla}T\cdot\vec{\nabla}\phi_m}_{\text{Electro-osmotic drag}} + \underbrace{\frac{\rho_{m,\,dry}}{EW}D_\lambda^{eff}\frac{\partial\bar{H}_\lambda}{\partial T}\vec{\nabla}T\cdot\vec{\nabla}\lambda}_{H_2O\text{ Diffusion}}$$
$$+ \underbrace{\frac{1}{M_{H_2O}}D_T^{eff}\frac{\partial\bar{H}_\lambda}{\partial T}\vec{\nabla}T\cdot\vec{\nabla}T}_{\text{Thermal-osmosis}} + \underbrace{S_{H^+_{Ohmic}}}_{\text{Ohmic Heating}} = 0\ . \quad (3.22)$$

Cathode Catalyst Layer

$$\underbrace{\vec{\nabla}\cdot\left(k^{eff}\vec{\nabla}T\right)}_{\text{Thermal Conductivity}} + \underbrace{D^{eff}_{O_2,N_2}\frac{p_T}{RT}\left(\frac{\partial\bar{H}_{O_2}}{\partial T}-\frac{\partial\bar{H}_{N_2}}{\partial T}\right)\vec{\nabla}T\cdot\vec{\nabla}x_{O_2}}_{\text{Thermal inter-diffusion transport } O_2 \text{ in } N_2}$$
$$+ \underbrace{D^{eff}_{H_2O,N_2}\frac{p_T}{RT}\left(\frac{\partial\bar{H}_{H_2O}}{\partial T}-\frac{\partial\bar{H}_{N_2}}{\partial T}\right)\vec{\nabla}T\cdot\vec{\nabla}x_{H_2O}}_{\text{Thermal inter-diffusion transport } H_2O \text{ in } N_2} + \underbrace{\frac{n_{drag}\ \sigma_m^{eff}}{F}\frac{\partial\bar{H}_\lambda}{\partial T}\vec{\nabla}T\cdot\vec{\nabla}\phi_m}_{\text{Electro-osmotic drag}}$$
$$+ \underbrace{\frac{\rho_{m,\,dry}}{EW}D_\lambda^{eff}\frac{\partial\bar{H}_\lambda}{\partial T}\vec{\nabla}T\cdot\vec{\nabla}\lambda}_{H_2O\text{ Diffusion}} + \underbrace{\frac{1}{M_{H_2O}}D_T^{eff}\frac{\partial\bar{H}_\lambda}{\partial T}\vec{\nabla}T\cdot\vec{\nabla}T}_{\text{Thermal-osmosis}}$$
$$\underbrace{S_{irrev,ORR}}_{\text{Irreversible electro-chem heat gen.}} - \underbrace{S_{rev,ORR}}_{\text{ORR reversible heat release}} - \underbrace{S_{vap,ORR}}_{H_2O\text{ vaporization}}$$
$$+ \underbrace{S_{H^+_{Ohmic}} + S_{e^-_{Ohmic}}}_{\text{Protonic and Electronic Ohmic Heating}} + \underbrace{S_{sorp,CL}}_{H_2O\text{ Adsorption / Desorption}} = 0. \quad (3.23)$$

Anode Catalyst Layer

$$\underbrace{\vec{\nabla}\cdot\left(k^{eff}\vec{\nabla}T\right)}_{\text{Thermal Conductivity}} + \underbrace{D^{eff}_{H_2O,H_2}\frac{p_T}{RT}\left(\frac{\partial\bar{H}_{H_2O}}{\partial T}-\frac{\partial\bar{H}_{H_2}}{\partial T}\right)\vec{\nabla}T\cdot\vec{\nabla}x_{H_2O}}_{\text{Thermal inter-diffusion transport } H_2O \text{ in } H_2}$$
$$+ \underbrace{\frac{n_{drag}\sigma_m^{eff}}{F}\frac{\partial\bar{H}_\lambda}{\partial T}\vec{\nabla}T\cdot\vec{\nabla}\lambda}_{\text{Electro-osmotic drag}} + \underbrace{\frac{\rho_{m,\,dry}}{EW}D_\lambda^{eff}\frac{\partial\bar{H}_\lambda}{\partial T}\vec{\nabla}T\cdot\vec{\nabla}\lambda}_{H_2O\text{ Diffusion}} + \underbrace{\frac{1}{M_{H_2O}}D_T^{eff}\frac{\partial\bar{H}_\lambda}{\partial T}\vec{\nabla}T\cdot\vec{\nabla}T}_{\text{Thermal-osmosis}}$$
$$+ \underbrace{S_{irrev,HOR}}_{\text{Irreversible electro-chem heat gen.}} - \underbrace{S_{rev,HOR}}_{\text{HOR reversible heat release}}$$
$$+ \underbrace{S_{H^+_{Ohmic}} + S_{e^-_{Ohmic}}}_{\text{Protonic and Electronic Ohmic Heating}} + \underbrace{S_{sorp,CL}}_{H_2O\text{ Adsorption / Desorption}} = 0 \quad (3.24)$$

Additional details on the thermal terms and derivations can be found in reference [17] and are not discussed further.

3.1.6 Kinetic Models

3.1.6.1 Cathode Kinetics

Tafel Kinetics (TK)

In the case of the ORR reaction, due to the high overpotentials and assuming abundant protons are available for reacting, the Butler-Volmer equation can be simplified to the Tafel equation [85, 93]:

$$i = i_0^{ref} \left(\frac{c_{O_2}}{c_{O_2}^{ref}} \right) e^{-\alpha F \eta / RT} \tag{3.25}$$

where i_0^{ref} is the exchange current density, $c_{O_2}^{ref}$ is the reference oxygen concentration, c_{O_2} is the oxygen concentration at the reaction site, α is the transfer coefficient, and η is the overpotential.

The overpotential of a cell is defined as:

$$\eta = (\phi_s - \phi_m) - E_{eq} \tag{3.26}$$

where ϕ_s and ϕ_m are the solid and electrolyte potentials, and E_{eq} is equilibrium potential for the half-cell reaction under the conditions at which α, i_0^{ref}, and $c_{0_2}^{ref}$ were measured. If the fuel cell operates at different operating conditions other than standard temperature and pressure (STP) the E_{eq} is defined by the Nernst Equation [85, 93].

$$E_{eq} = E_0 + \frac{\Delta s}{nF}(T - T_0) + \frac{RT}{nF} \ln \left(p_{O_2}^{1/2} \right) \tag{3.27}$$

where E_0 is the cells open cell voltage at standard temperature and pressure (STP) $1.229\,V$, Δs is the change in entropy, T_0 is standard temperature, T is the cell temperature, n is the number of electrons transferred, and p_{O_2} is the partial pressures of oxygen.

Equation (3.25) predicts the current per cm^2 of platinum surface rather than the required volumetric current density. To achieve this, the equation is multiplied using the active area of the cell, A_v. The active area relates the unit area of active platinum surface cm_{Pt}^2 to the unit volume of the electrode cm_{CL}^3, and is expressed as:

$$A_v = A_0 V_{Pt} \tag{3.28}$$

where A_0 is the experimentally observed active area (Section: 2.2.4.3), $\left[\frac{cm_{Pt}^2}{g_{Pt}}\right]$ and V_{Pt} is the volumetric loading of platinum, $\left[\frac{g_{Pt}}{cm_{CL}^3}\right]$.

In the above Tafel equation and the following Double-trap, Dual-path kinetics models the c_{O_2} and c_{H_2} are the concentrations at the reaction sites. As the active platinum is assumed to be under an ionomer film, the reactants will have to dissolve into a thin-film of ionomer. This concentration, c_g, at the reaction sites is expressed using Henry's law:

$$c_g = \frac{p_T x_g}{H_{g,N}} \tag{3.29}$$

where p_T is the total pressure, x_g is the mole fraction of the gas g, and $H_{g,N}$ is Henry's constant for the dissolution of the gas ($H_{H_2,N}$[94] and $H_{O_2,N}$[95]) in the ionomer film.

The Tafel (Butler-Volmer) equation is only applicable for single-electron transfer reactions. When considering the ORR reaction this is not the case, therefore the Tafel equation is unable to capture the complexity of the ORR which contains several steps [60, 96, 97]. This lead to the developments of an improved Double-trap kinetics model [61, 98]. Section 4.2 provides a discussion and comparisons of the Tafel and double-trap models.

Double-trap Kinetics (DTK)

The double-trap intrinsic kinetic model proposed by Wang et al. [60] is used to capture the ORR reaction. Although there are several intermediate species [97, 99], Wang et al. accounted for the coverage of two dominant intermediate species and four reaction steps, *i.e.*, the Dissociative Adsorption (DA), Reductive Adsorption (RA), which yield two reaction intermediate (OH_{ads}, O_{ads}), Reductive Transition (RT), and Reductive Desorption (RD). The reaction pathways are,

$$\tfrac{1}{2}O_2 \Leftrightarrow O_{ads} \qquad \text{Dissociative Adsorption (DA)} \tag{3.30}$$

$$\tfrac{1}{2}O_2 + H^+ + e^- \Leftrightarrow OH_{ads} \qquad \text{Reductive Adsorption (RA)} \tag{3.31}$$

$$O_{ads} + H^+ + e^- \Leftrightarrow OH_{ads} \qquad \text{Reductive Transition (RT)} \tag{3.32}$$

$$OH_{ads} + H^+ + e^- \Leftrightarrow H_2O \qquad \text{Reductive Desorption (RD)} \tag{3.33}$$

The above reaction steps result in the following two pathways [14]:

$$\tfrac{1}{2}O_2 \underset{+H^+e^-}{\overset{RA}{\rightleftharpoons}} OH_{ads} \underset{+H^+e^-}{\overset{RD}{\rightleftharpoons}} H_2O \tag{3.34}$$

$$\tfrac{1}{2}O_2 \overset{DA}{\rightleftharpoons} O_{ads} \underset{+H^+e^-}{\overset{RT}{\rightleftharpoons}} OH_{ads} \underset{+H^+e^-}{\overset{RD}{\rightleftharpoons}} H_2O \tag{3.35}$$

Moore et al. [61] implemented this model into OpenFCST [15] and further improved on Wang's model by correcting for the local reactant (O_2) concentrations which in turn affects the coverage of intermediate species [62]. Correction of the local reactant concentration is done assuming a linear relationship between current and oxygen concentration. Moore et al. [61] further improved the model by accounting for the backward reaction which was assumed negligible in the original formulation. The improved DTK model is now able to accurately predict the coverage profiles of intermediate species observed experimentally by Subramanian et al. [100] while also capturing experimentally observed doubling of the Tafel slope [101]. The kinetic current produced in the reaction is approximated as:

$$\mathrm{i} = A_v \left(j^* e^{-\Delta G^*_{RD}/kT} \theta_{OH} - j^* e^{-\Delta G^*_{-RD}/kT} \left(1 - \theta_O - \theta_{OH}\right)\right) \tag{3.36}$$

where A_v is the active area, j^* is the reference prefactor (scaling factor), set to 1,000 A/cm^2, ΔG^*_i are the potential dependent free energies of activation of the i^{th} step, finally θ_{OH} and θ_O are the coverages of intermediate species which have been fitted to experimental observed data from Parthasarathy et al. [101, 102].

Further details on the implementation and kinetic terms can be found in references [14, 61] and are not discussed further.

3.1.6.2 Anode Kinetics

Dual-Path (HOR) Kinetics

The hydrogen oxidation reaction (HOR) is usually analyzed using the Butler-Volmer equation. Chen and Kucernak [103] showed that the Butler-Volmer equation is inadequate to predict the HOR. Wang et al. [104] then proposed the Dual-path kinetics model, to express the HOR reaction kinetics.

Dual-path kinetics is based on Tafel-Heyrovsky-Volmer mechanism where three elementary reaction steps are present. The three reaction steps consist of one chemical pathway (Tafel), and two electrochemical (Heyrovsky, Volmer) [104] . The model assumes minimal coverages and negligible backwards reaction step, expressed as:

$$H_2 + 2Pt \leftrightharpoons 2(Pt - H_{ads}) \qquad \textbf{Tafel reaction} \tag{3.37}$$

$$H_2 + Pt \leftrightharpoons (Pt - H_{ads}) + H^+ + e^- \qquad \textbf{Heyrovsky reaction} \tag{3.38}$$

$$(Pt - H_{ads}) \leftrightharpoons Pt + H^+ + e^- \qquad \textbf{Volmer reaction} \tag{3.39}$$

Wang et al. proposed that the current density can be expressed as:

$$j_k = A_v \frac{c_{H_2}}{c_{H_2}^{ref}} \left[j_{0T} \left(1 - e^{-2F\eta/\gamma RT} \right) + j_{0H} \left(e^{F\eta/2RT} - e^{-F\eta/\gamma RT} e^{-F\eta/2RT} \right) \right] \tag{3.40}$$

where the Tafel-Volmer and Heyrovsky-Volmer exchange current density pathways are given by j_{0T} (0.47 A/cm^2) and j_{0H}, (0.01 A/cm^2) and γ (1.2) is a potential constant.

3.1.7 Source Terms

In order to apply a mass balance for each species three types of source terms are present, *i.e.*, reaction source, sorption source, and thermal source terms. The first couples the various species by having source/sink terms corresponding to the current production. The second couples the water in the catalyst layer with the water vapour in the gas by controlling the sorption and desorption of water to and from the ionomer. The third represents the thermal terms. Now that the flux terms have been derived for each of the governing equations the following governing equations containing source terms can be expressed as:

$$\begin{aligned}
-\vec{\nabla} \cdot \left(\frac{p_T}{RT} \, D_{O_2,N_2}^{eff} \vec{\nabla} x_{O_2} \right) &= S_{O_2} \\
-\vec{\nabla} \cdot \left(\frac{p_T}{RT} \, D_{H_2O,N_2 \text{ or } H_2}^{eff} \vec{\nabla} x_{H_2O} \right) &= S_{H_2O} + S_\lambda \\
-\vec{\nabla} \cdot \left(\sigma_m^{eff} \vec{\nabla} \phi_m \right) &= S_{H^+} \\
\vec{\nabla} \cdot \left(\sigma_s^{eff} \vec{\nabla} \phi_s \right) &= S_{e^-} \\
-\vec{\nabla} \cdot \left(n_{drag} \frac{\sigma_m^{eff}}{F} \vec{\nabla} \phi_m + \frac{\rho_{m,\,dry}}{EW} D_\lambda^{eff} \vec{\nabla} \lambda + \frac{D_T^{eff}}{M_{H_2O}} \vec{\nabla} T \right) &= -S_\lambda \\
-\vec{\nabla} \cdot \left(k^{eff} \vec{\nabla} T \right) + \sum_{\text{gases},\lambda} \left(\vec{N}_i \cdot \vec{\nabla} \bar{H}_i \right) &= S_T
\end{aligned} \tag{3.41}$$

3.1.7.1 Reactant Consumption and Production

Using Faraday's law and the stoichiometries of the reactions in Equation (1.2) and (1.3), the flux of charge species can be obtained as,

$$\vec{N}_i = -\frac{s_i}{nF} j \tag{3.42}$$

where s_i is the stoichiometry of species i, n is the number of electrons transferred in the reaction per mole of reactant fuel, and j is the volumetric current density, $\frac{A}{cm^3_{CL}}$.

In the CCL where the ORR reaction takes place the source terms for various species being consumed/produced, is expressed as:

$$\begin{aligned} \vec{N}_{O_2} &= S_{O_2} &&= -\frac{j}{4F} \\ \vec{N}_{H_2O} &= S_{H_2O} &&= \frac{j}{2F} \\ \vec{N}_{H^+} &= S_{H^+} &&= -\frac{j}{F} \\ \vec{N}_{e^-} &= S_{e^-} &&= -\frac{j}{F} \end{aligned} \tag{3.43}$$

In the ACL,

$$\begin{aligned} \vec{N}_{H^+} &= S_{H^+} = \frac{j}{F} \\ \vec{N}_{e^-} &= S_{e^-} = \frac{j}{F} \end{aligned} \tag{3.44}$$

The volumetric current density j, for the electrochemical reactions taking place in the catalyst layers is expressed using the kinetic models in Section 3.1.6.

The respective layer-specific source terms are given as:

$$S_{O_2} = \begin{cases} \frac{-j}{4F} & \text{in CCL} \\ 0 & \text{otherwise} \end{cases} \tag{3.45}$$

$$S_{H_2O} = \begin{cases} \frac{j}{2F} - k_t \frac{\rho_{m,\,dry}}{EW}(\lambda_{eq} - \lambda) & \text{in CCL} \\ -k_t \frac{\rho_{m,\,dry}}{EW}(\lambda_{eq} - \lambda) & \text{in ACL} \\ 0 & \text{otherwise} \end{cases} \tag{3.46}$$

$$S_{H^+} = \begin{cases} -j & \text{in CCL} \\ j & \text{in ACL} \\ 0 & \text{otherwise} \end{cases} \tag{3.47}$$

$$S_{e^-} = \begin{cases} -j & \text{in CCL} \\ j & \text{in ACL} \\ 0 & \text{otherwise} \end{cases} \tag{3.48}$$

3.1.7.2 Ionomer Water Sorption in the CLs

Water enters the system in two ways, water vapour from the humidified gases and also sorbed water produced during the ORR reaction in the CCL. In a vapour-equilibriated membrane at steady state operation, the amount of water vapour in the CL pores and sorbed water mole fractions in the CL ionomer should be in equilibrium. To relate the two mole fractions the equilibrium value λ in the electrolyte is determined by using the sorption isotherm. Hinatsu et al. [105] obtained this relationship at typical cell operating temperature of 80℃, showing that the equilibrium λ is dependant only on equivalent weight (EW) of the membrane, temperature, and water vapour mole fraction. In order to pair this relationship a coupling term is required to account for the sorption/desorption of water to/from the electrolyte, S_λ. This coupling term accounting for sorption/desorption is then added to the water vapour and sorbed water transport equations, as seen in Equation (3.41). Depending on the local humidity conditions and temperature values, water vapour will either be desorbed from the electrolyte to the pore space, or sorbed into the electrolyte from the pore space. This coupling term, is given as [79]:

$$S_\lambda = k_t \frac{\rho_{m,\,dry}}{EW}(\lambda_{eq} - \lambda) \tag{3.49}$$

where k_t is a time constant and is set to $10,000\,[s^{-1}]$, this large value is used to ensure a strong coupling between the membrane and the CL [79], λ is the membrane water content, and λ_{eq} is the equilibrium water content. The equilibrium membrane water content is determined by the sorption iosotherm given by Liu et al. [106] and is dependant on surrounding water vapour (water activity), and temperature:

$$\lambda_{eq} = \left[1 + 0.2352 a_w^2 \left(\frac{T - 303.15}{30}\right)\right](14.22 a_w^3 - 18.92 a_w^2 + 13.41 a_w) \tag{3.50}$$

where a_w is the activity of water vapour in the CL and is describe as:

$$a_w = \frac{p_T\ x_{H_2O}}{p_{sat}(T)} \tag{3.51}$$

where p_T is the cell pressure, x_{H_2O} is the mole fraction of water vapour, p_{sat} is the water saturation pressure and is dependent on temperature which has been expressed by Springer et al. [86]:

$$\begin{aligned} log_{10}\,(p_{sat}) = &-2.1794 + 0.02953\,(T - 273.15) - 9.1837 \times 10^{-5}\,(T - 273.15)^2 \\ &+ 1.4454 \times 10^{-7}\,(T - 273.15)^3 \end{aligned} \tag{3.52}$$

The respective layer-specific source terms are gives as:

$$S_{\lambda} = \begin{cases} k_t \frac{\rho_{m,\,dry}}{EW}(\lambda_{eq} - \lambda) & \text{in CLs} \\ 0 & \text{otherwise} \end{cases} \tag{3.53}$$

3.1.7.3 Thermal Source Terms

The thermal source terms arise from five main sources:

1. Ohmic heating from the proton and electron flux, $S_{H^+_{Ohmic}}$ and $S_{e^-_{Ohmic}}$.
2. Irreversible heat generation inside the ORR and HOR electrochemical reactions, $S_{irrev,ORR}$ and $S_{irrev,HOR}$.
3. Reversible heat release from the ORR and HOR half-cell reactions, $S_{rev,ORR}$ and $S_{rev,HOR}$.
4. Heat sink for the vaporization of liquid water produced during ORR reaction, $S_{vap,ORR}$
5. Heat release/adsorption due to the sorption/desorption of water vapour in the CLs, $S_{sorption,CL}$.

As mentioned in Section: 3.1.5.2, Bhaiya [17] implemented layer specific terms in order to account for the individual source/sink terms within each layer. The thermal source terms are represented as:

$$
S_T = \begin{cases}
\underbrace{\sigma_s^{eff}\left(\vec{\nabla}\phi_s \cdot \vec{\nabla}\phi_s\right)}_{\text{Electonic Ohmic Heating}} & \text{in GDL and MPL} \\
\underbrace{\sigma_m^{eff}(\vec{\nabla}\phi_m \cdot \vec{\nabla}\phi_m)}_{\text{Protonic Ohmic Heating}} & \text{in Membrane} \\
\underbrace{-j\eta}_{\text{Irreversible electro-chem heat gen.}} - \underbrace{\frac{j}{2F}T f_{ORR}\Delta\bar{S}_{overall}}_{\text{ORR reversible heat release}} - \underbrace{\frac{j}{2F}\bar{H}_{lv}}_{H_2O \text{ vaporization}} & \\
+ \underbrace{\sigma_m^{eff}(\vec{\nabla}\phi_m \cdot \vec{\nabla}\phi_m)}_{\text{Protonic Ohmic Heating}} + \underbrace{\sigma_s^{eff}(\vec{\nabla}\phi_s \cdot \vec{\nabla}\phi_s)}_{\text{Electonic Ohmic Heating}} & \\
+ \underbrace{k_t\frac{\rho_{m,\,dry}}{EW}(\lambda_{eq}-\lambda)\bar{H}_{sorp}}_{H_2O \text{ Adsorption/Desorption}} & \text{in CCL} \\
\underbrace{j\eta}_{\text{Irreversible electro-chem heat gen.}} + \underbrace{\frac{j}{2F}(-T(1-f_{ORR})\Delta\bar{S}_{overall})}_{\text{HOR reversible heat release}} & \\
+ \underbrace{\sigma_m^{eff}(\vec{\nabla}\phi_m \cdot \vec{\nabla}\phi_m)}_{\text{Protonic Ohmic Heating}} + \underbrace{\sigma_s^{eff}(\vec{\nabla}\phi_s \cdot \vec{\nabla}\phi_s)}_{\text{Protonic Ohmic Heating}} & \\
+ \underbrace{k_t\frac{\rho_{m,\,dry}}{EW}(\lambda_{eq}-\lambda)\bar{H}_{sorp}}_{H_2O \text{ Adsorption/Desorption}} & \text{in ACL}
\end{cases}
\tag{3.54}
$$

where f_{ORR} is a factor used to consider the fraction of reversible heat released in the ORR, $\bar{S}_{overall}$ is the overall entropy change per mole of fuel (H_2), $\bar{H}_{lv}$ is the molar latent heat of vaporization of water, $\bar{H}_{sorp}$ is molar enthalpy change (heat released) due to the sorption of water vapour into the ionomer. The above equations and therms are discussed in more detail in [17] and will not be developed further.

3.2 Solution Method and Boundary Conditions

In most practical real life problems complicated domains, loads, and nonlinear equations forbid the development of analytical solutions. For this reason, approximate solutions using numerical methods are developed. The numerical method used in OpenFCST to solve the non-linear partial differential equations that govern the fuel

cell behaviour, is the finite element method (FEM). FEM is a general technique used to construct approximate solutions to problems given in a partial differential equation (PDE) form. Solving PDEs involves the following steps:

1. Decomposition of the physical domain into finite pieces.
2. Developing a weak formulation of the PDE (integral form), and applying approximation functions to discretize and solve the problem. In this work, quadratic Langrange elements are used.
3. Applying boundary conditions.

In this work six solution variables are solve:

$$\vec{u} = \{x_{O_2},\ x_{H_2O},\ \phi_m,\ \phi_s,\ \lambda,\ T\} \tag{3.55}$$

3.2.1 Solution Method

The final system of equations, Equation (3.41), can be written as:

$$R(\vec{u}) = \begin{Bmatrix} x_{O_2} \\ x_{H_2O} \\ \phi_m \\ \phi_s \\ \lambda \\ T \end{Bmatrix} = 0 \tag{3.56}$$

Table 3.1 shows the equations solved in each domain (layer). In the cases where the variable is not solved at the edge of the MEA domain the boundary condition will then shift inwards to the edge of the relevant domain.

The partial differential equations are highly nonlinear due to current density source terms and variable dependent effective transport properties. Therefore, an iterative method is used to solve the non-linear FEM problem, in this case Newton's method is used. Newton's method requires an initial guess (u^0) to initialize the problem. Starting with an initial solution, the system of linearized equations are solved.

The linearized form of the governing equations is given as:

$$\left.\frac{\partial R}{\partial u}\right|_{u=u^n} (-\delta u) = R\left(u^n\right) \tag{3.57}$$

where δu is the perturbed solution variable, u^n is the solution at the previous Newton step and $u^{n+1} = u^n + \delta u$. The linear system is solved iteratively until the residual

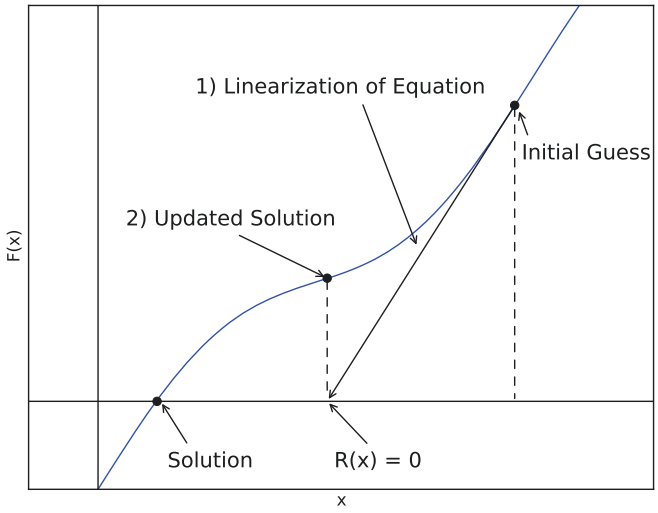

Figure 3.2 – Graphical representation of the steps involved when solving a non-linear equation using Newton's method.

has reached a required tolerance as shown in Figure 3.2. In this work a tolerance of 10^{-10} ($R(u) \leqslant 10^{-10}$).

To solve the linearized system of PDEs, the finite element method is used. A weak form of the governing equations is obtained using Bubanov-Galerkin FEM where second order Langrangian polynomials approximate the solution. Once the system of equations has been discretized, an algebraic system of equations is obtained, $Au = \vec{b}$, and solved using UMFPACK [107]. Further discussions and detailed explanations of the numerical methods can be found at the following reference [79] and is not discussed further.

Table 3.1 – Table of solution variables considered in the single-phase, non-isothermal MEA model.

Solution variable	AGDL	AMPL	ACL	ML	CCL	CMPL	CGDL
Oxygen molar fraction, x_{O_2}					✓	✓	✓
Water molar fraction, x_{H_2O}	✓	✓	✓		✓	✓	✓
Solid potential, ϕ_s	✓	✓	✓		✓	✓	✓
Electrolyte potential, ϕ_m			✓	✓	✓		
Membrane water content, λ			✓	✓	✓		
Temperature, T	✓	✓	✓	✓	✓	✓	✓

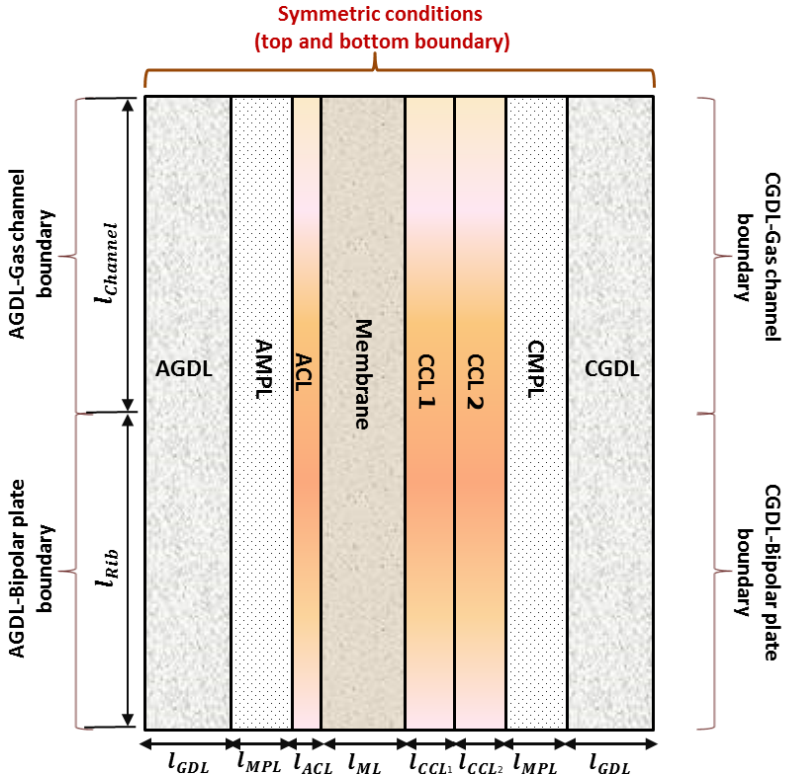

Figure 3.3 – Description of the computational domain with multiple CCLs. Modified and reproduced with permission [17]

3.2.2 Boundary Conditions

The MEA computational domain consists of seven two dimensional layers. When considering functionally graded MEA domains, the number of layers will increase depending on the number of additional CCLs, as seen in Figure 3.3. In order to reduce the computational requirement the MEA domain only considers half of the channel and bipolar plate width. This can be done due to the symmetry of the problem [79].

The symmetry of the domain is captured by applying no species flux at the top and bottom boundary of the geometry. There are six boundaries in total:

1. Two symmetric boundaries
2. Two current collector boundaries, AGDL-Bipolar plate and CGDL-Bipolar plate
3. Two gas channel boundaries, AGDL-Gas channel and CGDL-Gas channel

Symmetric Boundary Conditions

At the symmetric boundaries the flux terms are equal to zero and no solution variables are know, therefore only Neumann conditions are present:

$$\begin{aligned}
N_{e^-} &= \vec{n} \cdot (\sigma_s^{eff} \vec{\nabla} \phi_s) &&= 0 \\
N_{H^+} &= \vec{n} \cdot (\sigma_m^{eff} \vec{\nabla} \phi_m) &&= 0 \\
N_{O_2} &= \vec{n} \cdot (\frac{p_T}{RT} D_{O_2,N_2}^{eff} \vec{\nabla} x_{O_2}) &&= 0 \\
N_{H_2O} &= \vec{n} \cdot (\frac{p_T}{RT} D_{H_2O,N_2}^{eff} \vec{\nabla} x_{H_2O}) &&= 0 \\
N_\lambda &= \vec{n} \cdot \left(\frac{\sigma_m^{eff}}{F} \vec{\nabla} \phi_m + \frac{\rho_{m,\,dry}}{EW} D_\lambda \vec{\nabla} \lambda + \frac{D_T^{eff}}{M_{H_2O}} \vec{\nabla} T \right) &&= 0 \\
N_T &= \vec{n} \cdot \left(\left(k^{eff} \vec{\nabla} T \right) - \sum_{\text{gases},\lambda} \vec{n} \cdot \left(\vec{\nabla} \bar{H}_i \right) \right) &&= 0
\end{aligned} \tag{3.58}$$

where $\vec{n}$ is the normal to the boundary surface, and N_i are the flux normal to the boundary.

Anode Gas Channel

The anode gas channel has 5 flux boundary (Neumann) conditions and one value boundary (Dirichlet) condition,

$$x_{H_2O} = x_{H_2O,\,a}^0$$

$$\begin{aligned}
N_{e^-} &= \vec{n} \cdot (\sigma_s^{eff} \vec{\nabla} \phi_s) &&= 0 \\
N_{H^+} &= \vec{n} \cdot (\sigma_m^{eff} \vec{\nabla} \phi_m) &&= 0 \\
N_{O_2} &= \vec{n} \cdot (\frac{p_T}{RT} D_{O_2,N_2}^{eff} \vec{\nabla} x_{O_2}) &&= 0 \\
N_\lambda &= \vec{n} \cdot \left(\frac{\sigma_m^{eff}}{F} \vec{\nabla} \phi_m + \frac{\rho_{m,\,dry}}{EW} D_\lambda \vec{\nabla} \lambda + \frac{D_T^{eff}}{M_{H_2O}} \vec{\nabla} T \right) &&= 0 \\
N_T &= \vec{n} \cdot \left(k^{eff} \vec{\nabla} T \right) &&= 0
\end{aligned} \tag{3.59}$$

Cathode Gas Channel

The cathode gas channel has the same flux boundary conditions as in the anode, however oxygen and water mole fractions are specified for the Dirichlet conditions.

$$\begin{aligned}
x_{O_2} &= x_{O_2}^0 \\
x_{H_2O} &= x_{H_2O,\,c}^0
\end{aligned} \tag{3.60}$$

Anode Bipolar Plate Boundary

At the bipolar plate boundaries, both Dirichlet and Neumann boundary conditions exist. Since the bipolar plate is a non porous material no species flow across the boundary except for thermal energy. The Dirichlet conditions represent the known reference/cell potential (anode/cathode). Then,

$$\begin{aligned}
\phi_s &= 0 \\
N_{H^+} &= \vec{n} \cdot (\sigma_m^{eff} \vec{\nabla} \phi_m) &= 0 \\
N_{O_2} &= \vec{n} \cdot (\frac{p_T}{RT} D_{O_2,N_2}^{eff} \vec{\nabla} x_{O_2}) &= 0 \\
N_\lambda &= \vec{n} \cdot \left(\frac{\sigma_m^{eff}}{F} \vec{\nabla} \phi_m + \frac{\rho_{m,\,dry}}{EW} D_\lambda \vec{\nabla} \lambda + \frac{D_T^{eff}}{M_{H_2O}} \vec{\nabla} T \right) &= 0 \\
\sum_{\text{gases},\lambda} N_i &= \sum_{\text{gases},\lambda} \vec{n} \cdot \left(\vec{\nabla} \bar{H}_i \right) &= 0
\end{aligned} \tag{3.61}$$

Cathode Bipolar Plate Boundary

Similarly the cathode bipolar plate has the same flux boundary (Neumann) conditions as in the anode. In the anode case the solid potential (ϕ_s) is set to zero as it is the reference electrode, while the cathode side is set to V_{cell} which is computed using Nernst Equation (Equation (3.27)). This differential in potential across the cell is used to compute the current.

$$\phi_s = V_{cell} \tag{3.62}$$

The geometric properties (dimensions) of the computational domain (MEA) considered in this work are given in Table 3.2.

Table 3.2 – Geometric dimensions of the computational domain

Parameters	Value, $[\mu m]$
l_{GDL}	250
l_{MPL}	50
l_{ACL}	Cell Dependent [1]
l_{CCL}	Cell Dependent [2]
l_{ML}	25
l_{Rib}	500
$l_{Channel}$	500

[1] The ACL thickness will depend on the experimental cell, Section: 2.2.3

[2] The CCL thickness will depend on the experimental cell, Section: 2.2.3

3.3 Base Parameters

In this section, the base parameters for the PEFC simulations are introduced. These input parameters describe properties such as charged transport, composition and reactant transport properties of the GDL, MPL, ACL, CCL, and also the material bulk properties. The composition and transport properties for the GDL and MPL are considered to be the same for both electrodes. In this work Nafion®, platinum loadings, and functionally graded ionomer loading is studied. These parameter changes are shown in Table 3.8, 3.9, 3.10 and 3.11.

3.3.1 Gas Diffusion Layer Parameters

Table 3.3 shows the GDL properties used for both the anode and cathode as well as the value of the percolation constants and thermal conductivities [79, 108–111].

Table 3.3 – Composition and transport properties of the GDL

Parameters	Value
Composition	
Porosity, ε	0.6
Gas transport properties	
Porosity threshold, ε^{th}	0.118
Porosity network constant X, μ^X	0.785
Porosity network constant Y, μ^Y	0.521
Electron transport properties	
Solid network threshold, ε_s^{th}	0.0
Solid network constant X, μ_s^X	1.5
Solid network constant Y, μ_s^Y	1.0
Thermal transport properties	
Effective thermal conductivity X, k_X^{eff}	[17]
Effective thermal conductivity Y, k_Y^{eff}	[17]

3.3.2 Micro Porous Layer Parameters

Table 3.4 shows the MPL properties used for both the anode and cathode as well as the value of the percolation constants and thermal conductivities [79, 108–111].

Table 3.4 – Composition and transport properties of the MPL

Parameters	Value
Composition	
Porosity, ε	0.4
Gas transport properties	
Porosity threshold, ε^{th}	0.118
Porosity network constant, μ	2.0
Electron transport properties	
Solid network threshold, ε_s^{th}	0.118
Solid network constant, μ_s	2.0
Thermal transport properties	
Effective thermal conductivity X, k_X^{eff} $[W \cdot cm^{-1} \cdot K^{-1}]$	0.003 [112]
Effective thermal conductivity Y, k_Y^{eff} $[W \cdot cm^{-1} \cdot K^{-1}]$	0.0387 [113]

3.3.3 Conventional CCL Parameters

Table 3.5 defines the composition, gas transport properties, electron transport properties, and thermal transport properties used in simulating the conventional spray coated conventional CCL ($l_{CCL} = 1.0 \times 10^{-3}$ $[cm]$) [17, 79, 114, 115].

3.3.4 Conventional ACL Parameters

Table 3.6 defines the composition, gas transport properties, electron transport properties, and thermal transport properties used in simulating the conventional spray coated ACL ($l_{ACL} = 3.33 \times 10^{-4}$ $[cm]$) [17, 79, 114, 115].

3.3.5 Bulk Material Properties

Table 3.7 defines the PEFC bulk material properties for Nafion®, Pt, and carbon [17, 79, 117].

Table 3.5 – Composition and transport properties of the conventional CCL

Parameters	Value
Composition	
Platinum loading on support $[wt.\%]$	46
Platinum loading per unit volume $[mg \cdot cm^{-3}]$	400
Electrolyte loading $[wt.\%]$	30
Active area $[cm^2 \cdot cm^{-3}]$	2.0×10^5
Gas transport properties	
Porosity threshold, ε^{th}	0.259
Porosity network constant, μ	2.0
Electron transport properties	
Solid network threshold, ε_s^{th}	0.118
Solid network constant, μ_s	2.0
Thermal transport properties	
Effective thermal conductivity, k^{eff} $[W \cdot cm^{-1} \cdot K^{-1}]$	0.0027 [17, 116]

Table 3.6 – Composition and transport properties of the conventional ACL

Parameters	Value
Composition	
Platinum loading on support $[wt.\%]$	46
Platinum loading per unit volume $[mg \cdot cm^{-3}]$	300
Electrolyte loading $[wt.\%]$	30
Active area $[cm^2 \cdot cm^{-3}]$	1.2×10^5
Gas transport properties	
Porosity threshold, ε^{th}	0.259
Porosity network constant, μ	2.0
Electron transport properties	
Solid network threshold, ε_s^{th}	0.118
Solid network constant, μ_s	2.0
Thermal transport properties	
Effective thermal conductivity, k^{eff} $[W \cdot cm^{-1} \cdot K^{-1}]$	0.0027 [17, 116]

Table 3.7 – Bulk properties of the PEFC materials

Parameters	Value
Nafion®	
Equivalent weight, EW $[g \cdot mol^{-1}]$	1100
Dry membrane density, $\rho_{m,\,dry}$ $[g \cdot cm^{-3}]$	2.0
Thermal conductivity, k $[W \cdot cm^{-1} \cdot K^{-1}]$	0.0013
Carbon	
Density, ρ $[g \cdot cm^{-3}]$	2
Particle electron conductivity, σ_s $[S \cdot cm^{-1}]$	88.84
Fibre electron conductivity X, σ_s^X $[S \cdot cm^{-1}]$	16.03
Fibre electron conductivity Y, σ_s^Y $[S \cdot cm^{-1}]$	272.78
Platinum	
Density, ρ_{Pt} $[g \cdot cm^{-3}]$	21.5

3.3.6 Nafion® Loading Parameters

The experimental parameters obtained in the Nafion® loading study carried out by Shukla et al. [1] can be seen in Table 3.8. The table shows the composition of the relevant PEFCs and have been used to simulated the Nafion® loading results in Chapter 4. The ACL properties are kept constant throughout the Nafion® loading study and are represented by the 30 wt.% ionomer loading. All other PEFC properties, such as, gas diffusion media and material properties remain the same as given in previous tables.

Table 3.8 – Composition properties of the CCL with respect to Nafion® loading

Electrolyte loading $[wt.\%]$	10	20	30	40	50
Composition					
Pt loading on support $[wt.\%]$	20	20	20	20	20
Pt loading per unit vol. $\left[\frac{mg_{Pt}}{cm^3_{CL}}\right]$	161.29	161.29	161.29	161.29	161.29
Active area $[cm^2_{Pt} \cdot cm^{-3}_{CL}]$	80645	101613	104839	98387	91935

3.3.7 Platinum Loading Parameters

The experimental Pt loading study obtained via ex-situ testing in this work using the EG ink can be seen in Table 3.9. The tables shows the composition of the relevant

PEFCs and have been used to simulated the Pt loading results in Chapter 4. The ACL properties are kept constant throughout the Pt loading study and are represented by the 28 $\mu g_{Pt}/cm^2$ loading. All other PEFC properties, such as, gas diffusion media and material properties remain the same.

Table 3.9 – Composition properties of the CCL with respect to Pt loading

Pt Loading $[\mu g_{Pt}/cm^2]$	28	56	84	112
Composition				
Pt loading on support $[wt.\%]$	20	20	20	20
Pt loading per unit vol. $\left[\frac{mg_{Pt}}{cm^3_{CL}}\right]$	133	175	182.6	203.6
Electrolyte loading $[wt.\%]$	30	30	30	30
Active area $[cm^2_{Pt} \cdot cm^{-3}_{CL}]$	104000	97969	94957	90781

3.3.8 Functionally Graded Nafion® Parameters

The functionally graded ionomer electrodes were first simulated using the experimentally observed data for a typical 54 $\mu g_{Pt}/cm^2$ (10 layer) loaded electrode using glycerol ink, as seen in Table 3.10 (ML|30|30). The functionally graded study initial assumes that the active area is similar to that of the homogeneous electrode in order to observe the trends solely due to the ionomer grading. The parameters used to initially view the graded trends are seen in Table 3.10.

In addition, two functionally graded ionomer electrodes were fabricated to validate the predictive abilities of the functionally graded model. The experimentally observed ECSA from these electrodes, as seen in Section 4.1.2.5 are then used as the simulation parameters, seen in Table 3.11. These experimental ECSA parameters are used to compared against the experimental trends in Section 4.5.2.

Table 3.10 – Composition properties of the CCL for functionally graded ionomer electrodes using ECSA observed from a homogeneous 54 $\mu g_{Pt}/cm^2$ electrodes, to guide functionally graded ionomer experimental efforts.

Pt Loading $[\mu g_{Pt}/cm^2]$	ML|30|30	ML|20|20	ML|20|40	ML|40|20	ML|40|40
Composition					
Pt loading on support $[wt.\%]$	20	20	20	20	20
Pt Loading $[\mu g_{Pt}/cm^2]$	54	54	54	54	54
Pt loading per unit vol. $\left[\frac{mg_{Pt}}{cm^3_{CL}}\right]$	174	174	174	174	174
Electrolyte loading $[wt.\%]$	30	20	30	30	40
Active area $[cm^2_{Pt} \cdot cm^{-3}_{CL}]$	68806	68806	68806	68806	68806

Table 3.11 – Composition properties of the CCL for functionally graded ionomer electrodes using experimental ECSA results.

Pt Loading $[\mu g_{Pt}/cm^2]$	ML|20|40	ML|40|20
Composition		
Pt loading on support $[wt.\%]$	20	20
Pt Loading $[\mu g_{Pt}/cm^2]$	54	54
Pt loading per unit vol. $\left[\frac{mg_{Pt}}{cm^3_{CL}}\right]$	174	174
Electrolyte loading $[wt.\%]$	30	30
Active area $[cm^2_{Pt} \cdot cm^{-3}_{CL}]$	83613	91277

3.4 Functionally Graded Enhancement

In this work, the current OpenFCST framework has been modified in order to study functionally graded CLs. Functionally graded electrodes are studied by dividing the CCL into multiple blocks of CLs with homogeneous properties. The functionally graded model when using multiple CCLs has the exact same boundary conditions and geometric properties except for possessing additional CCLs, Figure 3.3. With this new functionality it is now possible to simulate PEFCs with multiple CCLs that vary in properties such as Pt and Nafion® loading.

3.4.1 Validation of Functionally Graded Model

In order to validate the functionally graded model, a graded electrode with two identical layers is compared to the previously developed macro homogeneous model. Figure 3.4 shows the polarization curve and temperature comparisons between the conventional homogeneous CCL and the functionally graded CCL. Both models show the exact same performance and temperature throughout the polarization curve. In addition when comparing the contour plots, as seen in Figure 3.5, both show the exact same current and temperature profiles. Therefore, there is no change in model performance with the addition of multiple CCLs thereby validating the functionally graded application. Table 3.12 defines the geometric dimensions for the two domains.

Table 3.12 – Validation domain geometric dimensions

Parameters	Homogeneous $[\mu m]$	Functionally Graded $[\mu m]$
l_{GDL}	250	250
l_{MPL}	50	50
l_{ACL}	3.33	3.33
l_{CCL_1}	10	5
l_{CCL_2}	-	5
l_{ML}	25	25
l_{Rib}	500	500
$l_{Channel}$	500	500

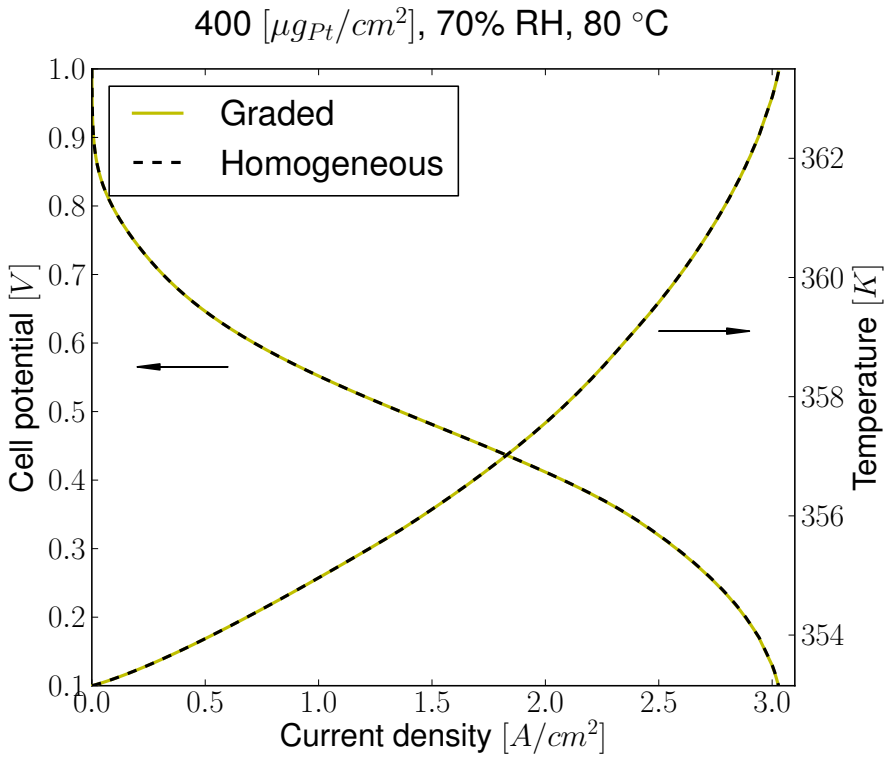

Figure 3.4 – Validation comparisons of the functionally graded model against the homogeneous model

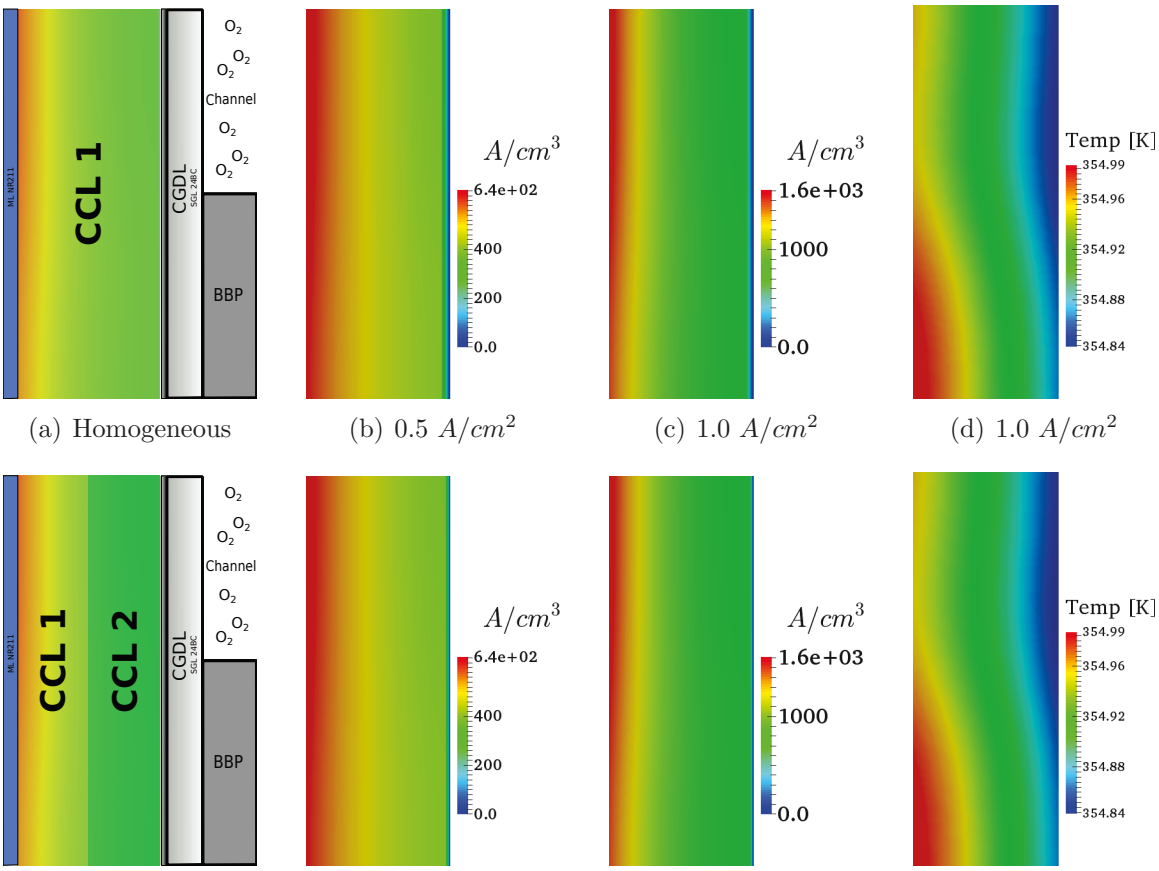

(a) Homogeneous (b) 0.5 A/cm^2 (c) 1.0 A/cm^2 (d) 1.0 A/cm^2

(e) Graded (f) 0.5 A/cm^2 (g) 1.0 A/cm^2 (h) 1.0 A/cm^2

Figure 3.5 – Comparison of homogeneous CL and functionally graded CL to validate model. (a)-(d) represent the homogeneous CCL contour plots for current density and temperature, where the contour regions is marked in (a) by the CCL 1 region. (e)-(h) represents the functionally graded CCL contour plots for current density and temperature, where the contour regions is marked in (e) by the CCL 1 and CCL 2 region. The zero current density along the right edge is a post process artifact caused by zero current in the MPL.

Chapter 4

Results

The results chapter has been separated into five sections:

1. PEFC characterization
2. Nafion® loading (NL) study
3. Platinum loading study
4. Oxygen partial pressure
5. Functionally graded Nafion® study

The first section provides the results of the PEFC characterization using the methodology described in Chapter 2, the remaining four sections will qualitatively look at both experimental results and simulated results with a quantitative discussion section at the end of each.

4.1 PEFC Characterization

4.1.1 Ex-situ Characterization

4.1.1.1 Thickness Analysis

To obtain the thickness of the CCMs the specimens were examined using SEM imaging, as described in Section 2.2.3. Figure 4.1 shows images from the thickness study using EG at $x6000$ magnification against the number of printer passes, intermediate drying and increased solvent content. The membrane is located on the left hand side of all the images. The bright porous layer on the membrane is the CL.

Table 4.1 – CCM thickness using micrograph analysis

	Ink Type			
Printer Passes #	Gly [μm]	EG [μm]	EG [1] [μm]	EG* [μm]
5	1.6 ± 0.3 [2]	2.1 ± 0.3		2.5 ± 0.5
10	3.0 ± 0.6 [2]	3.2 ± 0.6	3.5 ± 0.8	
15	4.5 ± 0.6	4.6 ± 0.5		
20	6.1 ± 1.0	5.5 ± 0.5		

The freeze fractured samples show almost uniform thickness along the membrane and no large voids with homogeneous distribution throughout the CCM. As the number of printer passes increase, the CL thickness also increases as in Figure 4.1 (a) to Figure 4.1 (f). The CLs show good adhesion to the membrane surface, an attribute that leads to low inter-facial resistance and improved degradation properties [118]. This intimate interface has also shown to remain after testing, which is advantageous over decal methods whereby the CCM is pressed onto the membrane surface and has shown to delaminate in post tested images [118].

The thickness study also included a CL which has been dried in between each 5 passes, and is represented by ML|5DRY|5. It was observed that the ML|5DRY|5 CL increased in thickness by 10% and standard deviation (STDEV) by 33% compared to the ten layer with no intermediate drying process. The ink with increased amounts of EG (EG*) had the greatest thickness, however, due to drying issues at greater passes no further thickness studies were possible.

The thickness data has been graphed in Figure 4.2 showing the linear and non-linearity of thickness with Gly and EG, and also tabulated in Table 4.1 showing the exact results and STDEV.

In terms of surface characteristics the Gly ink showed striations along the sweeping path of the printer, as seen in Figure 4.3 (a). Figure 4.3 (b) shows that these striations are reduced using the EG ink. The EG* ink which contains larger solvent content showed the best membrane coverage, however, as a result of the large solvent content the drying time increased from 24 hours to 48 hours for the five layer CLs. Printing ten layers or greater with EG* ink, resulted in the CLs not drying using an oven

[1] Dried before printing second five passes.
[2] Two separate samples

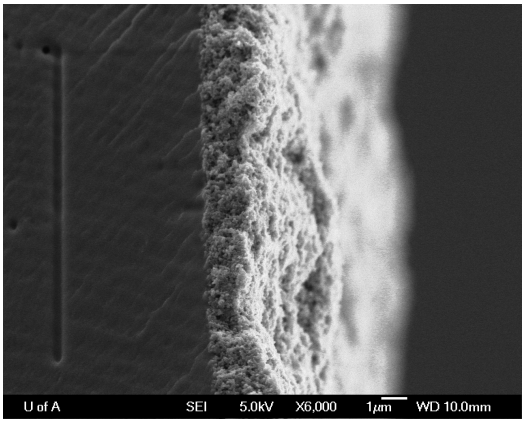

(a) 5 Passes

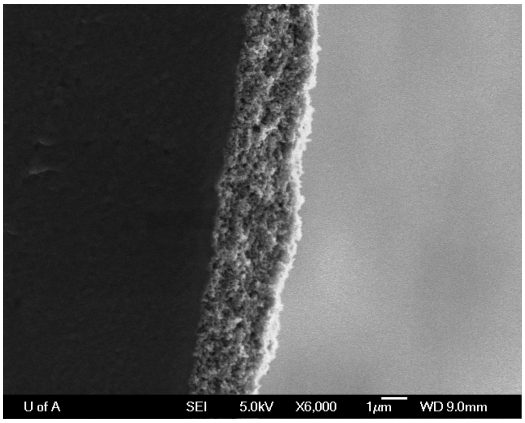

(b) 5 Passes, increased EG content (EG*)

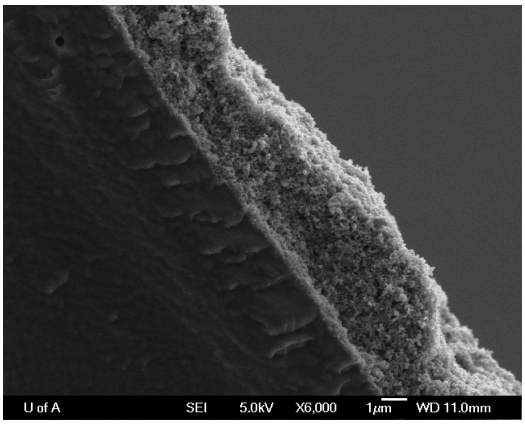

(c) 10 Passes

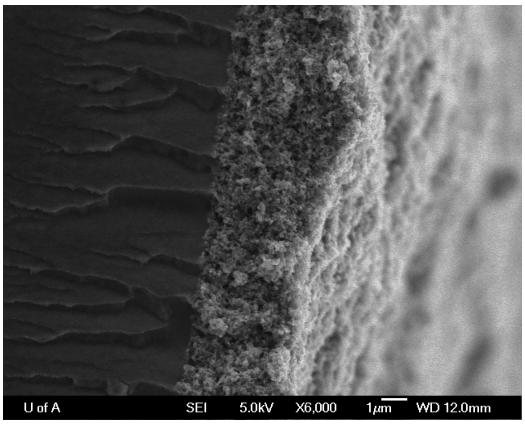

(d) 10 Passes, ML|5Dry|5

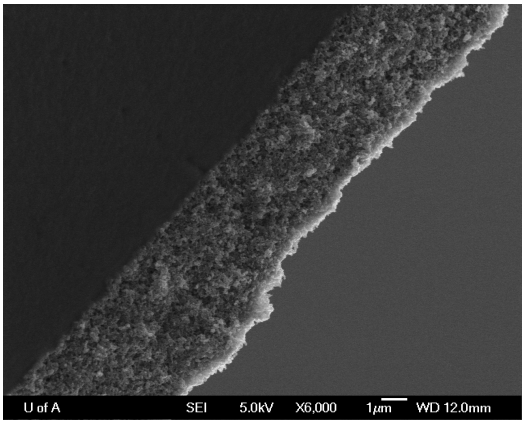

(e) 15 Passes

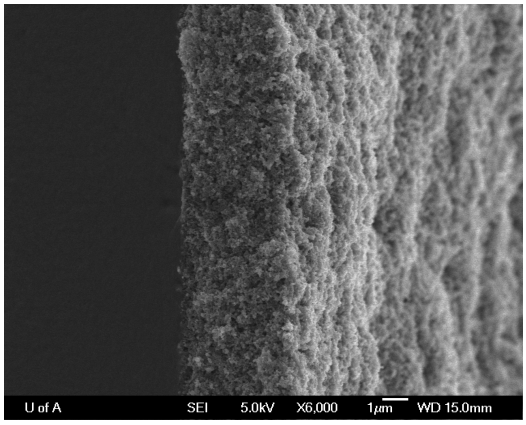

(f) 20 Passes

Figure 4.1 – Variation of Ethylene glycol CCM thickness with number of printer passes, intermediate drying and solvent content at x6000 magnification: (a) 5 passes, (b) 5 passes with increased Ethylene glycol content, (c) 10 passes, (d) 10 passes (ML|5Dry|5), (e) 15 passes, and (f) 20 passes.

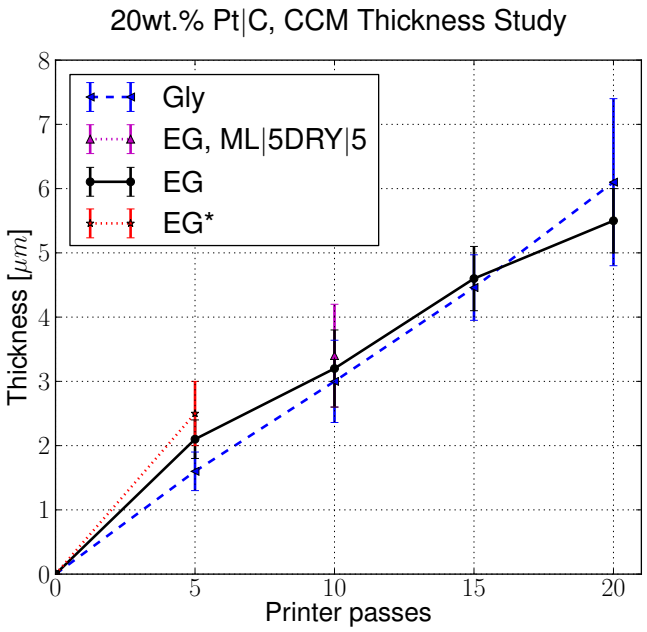

Figure 4.2 – Thickness analysis of 30 wt.% ionomer loading CCMs, with varying printer passes and solvent type. Gly ink showing a linear relationship, EG showing non-linear relationship, EG* having increased amounts of EG being the thickness of the 5 layer CLs, and EG with intermediate drying showing largest thickness and STDEV of the 10 pass CLs.

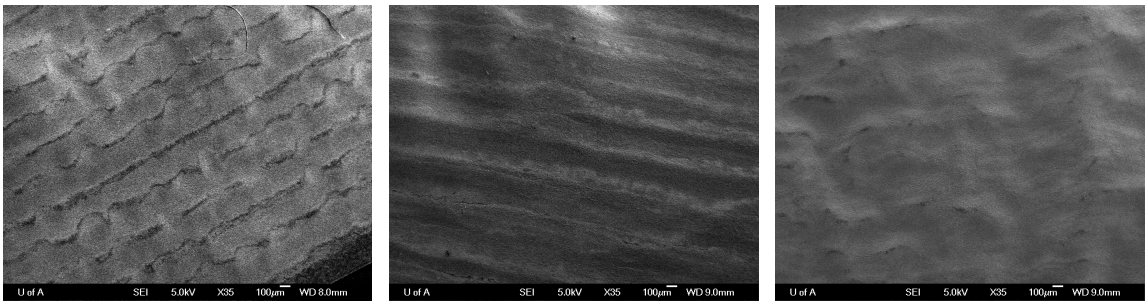

(a) Gly: 5 Passes (b) EG: 5 Passes (c) EG*: 5 Passes

Figure 4.3 – Variation of CCM surface with ink solvent and solvent content: When using Gly ink and 5 passes (a) significant striations occur, using EG ink and 5 passes (b) the striations are reduced, and EG with increased solvent content (EG*) and 5 passes showing most uniformity (c).

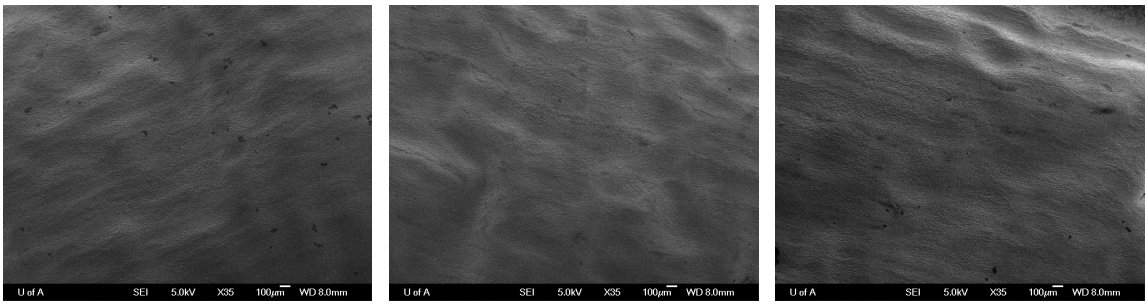

(a) 10 Passes (b) 15 Passes (c) 20 Passes

Figure 4.4 – Uniform coverage of EG CCM surface characteristics at 10 to 20 passes.

temperature of 80 °C. Therefore, fabrication of CCMs with more than 5 passes was not achievable using the EG* ink. Gly and EG ink types were used in the Pt loading study, both showing uniform coverage over the membrane at 10 passes or greater. Figure 4.4 shows the uniform coverage of the EG ink type for 10 to 20 passes which was also observed for the Gly ink.

4.1.1.2 Platinum Loading

The Pt loadings of the CLs were obtained using X-Ray Fluorescence (Thermo Scientific, Niton XL3t) at AFCC, one of the ESDL collaborators. Investigating the Pt content as a function of printer passes showed that a catalyse layers Pt loading is not very sensitive to solvent type or content. Table 4.2 shows the Pt loadings and STDEV of differing ink types. When printing the 20 wt.% Pt|C EG ink showed to have superior printer cartridge compatibility compared to other ink types and as a

Table 4.2 – CCM loading analysis using XRF data

	Ink Type			
Printer passes #	20% Pt|C Gly $\left[\frac{\mu g_{Pt}}{cm^2}\right]$	46.7% Pt|C Gly $\left[\frac{\mu g_{Pt}}{cm^2}\right]$	20% Pt|C EG $\left[\frac{\mu g_{Pt}}{cm^2}\right]$	20% Pt|C EG* $\left[\frac{\mu g_{Pt}}{cm^2}\right]$
3	-	37	-	-
5	27.2 ± 2 [1]	61	27.8 ± 0.05 [1]	26.4 ± 1.56 [1]
10	58.6 ± 2 [1]	-	59.8 ± 1.57 [1]	-

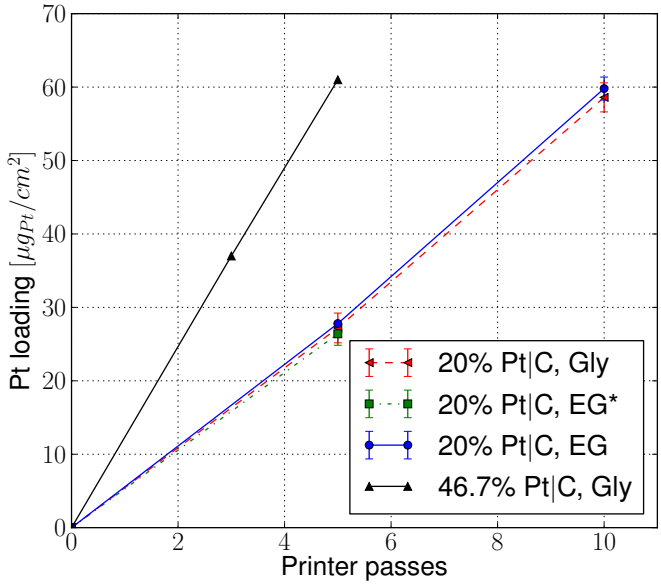

Figure 4.5 – Platinum loading analysis with respect to ink type, number of printer passes, and Pt|C support.

result has relatively low STDEVs. Table 4.2 has been illustrated in Figure 4.5 showing a close to linear increase in Pt loading with respect to solvent type, number of printer passes, and Pt|C support.

4.1.2 In-situ Characterization

4.1.2.1 Fuel Crossover

Crossover analysis has been carried out using the methodology explained in Section 2.2.4.2. Crossover is caused by diffusion of reactant from the anode to the cathode through the membrane and through pin holes in the PEM due to damage. In this

[1] Two samples

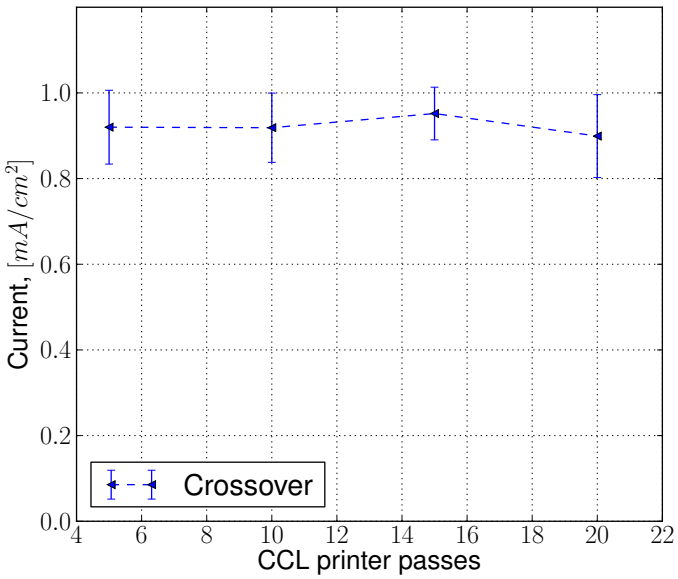

Figure 4.6 – Average crossover results for pristine cells with varying CCL printer passes, while ACL is remained constant at 5 printer passes.

work, Nafion® NR211 (25 μm) membranes are used. Figure 4.6 shows the average crossover versus CL thickness of all CLs fabricated. The average crossover current for successful CCMs is less than 1 mA/cm^2 (2.0×10^{-8} $mole \cdot s^{-1} \cdot cm^{-2}$), regardless of the number of printer passes. Only results for cells that are below this ≈ 1 mA/cm^2 threshold are reported in this thesis.

4.1.2.2 Cell Resistances

The cell resistance has been achieved using the methodology described in Section 4.1.2.2. Figure 4.7 shows the cell resistance at different temperatures. An increasing linear trend is observed with increasing temperature. Cell assembly resistance, without the MEA, is found to be ≈ 1.9 $m\Omega/cm^2$ at an operating cell temperature of 80 °C. Therefore the electronic transfer losses are found to be relatively small when compared to the protonic transfer losses through the ionomer in the CL and ML.

The protonic transfer losses decreases with increasing RH and current production due to the increase in sorbed water content in the ionomer, as described in Section 3.1.4. This can be observed in Figure 4.8 where the iR resistance is seen to decrease with increasing RH and current density. The figure shows that under conditions where air is supplied on the cathode side at 90% RH, the electronic and contact resistances

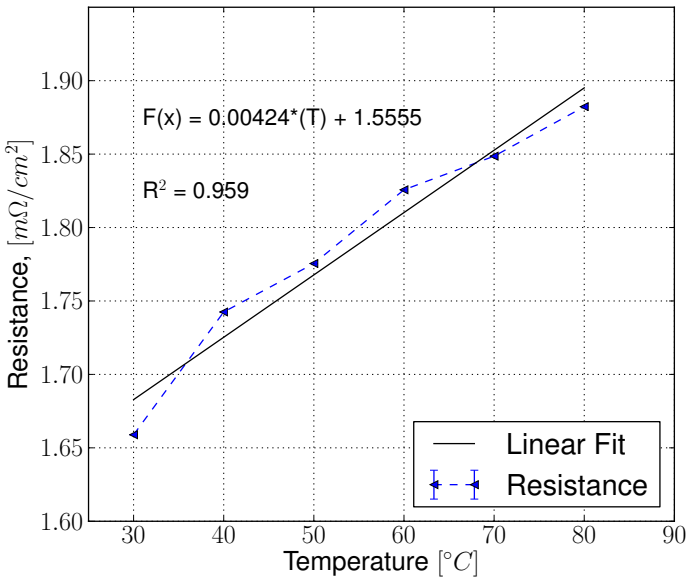

Figure 4.7 – Cell assembly electronic resistance per cm^2 vs. temperature.

make up a maximum of 29% of the overall resistance.

Figure 4.8 shows an unusual result of zero iR resistance at low current densities. This is caused by the operating range of the equipment. When the test station introduces a current interrupt it measures the change in voltage. This change in voltage needs to be above a certain threshold in order for the equipment to detect the change, and calculate the resistance using Equation (2.4). Therefore, only at large enough currents can the voltage drop be detected. This explains the increasing zero iR results at the initial stage of the graph with decreasing resistance. At large voltage drops (iR, 50RH) the current required is less than at the low voltage drop (iR, 90RH), hence the increasing delay when reading iR for the 70% and 90% RH case compared to the 50% case.

4.1.2.3 Pt Loading and Concentration vs. ECSA

Several factors can have an effect on the ECSA, such as particle size, Pt|C, ionomer loading, relative humidity, and Pt loading [13, 32, 75, 119–121] . In this study, it is observed that the specific ECSA decreased with increasing Pt loading [13, 119, 121], however, this was not observed when the Pt|C support was changed from 20 to 46.7 wt.% Pt|C. This maybe due to the fact that at equivalent loadings the 20 wt.% Pt|C

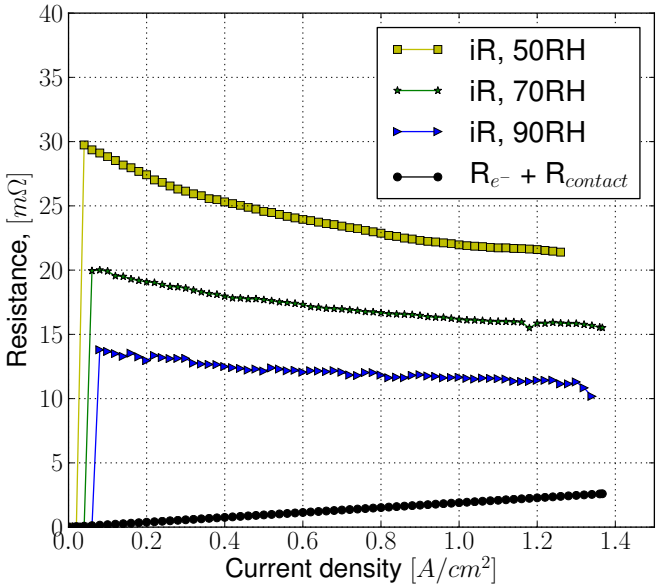

Figure 4.8 – Cell Resistance over different RH values, showing the total internal cell resistance (iR) and the resistance associated with electronic (R_{e^-}) and contact ($R_{contact}$) resistance. Where the iR resistance is seen to decrease with increasing RH and current density due to reduced charge transport resistance.

Table 4.3 – CCM active area analysis of Pt loading, solvent type, and wt.% of Pt|C

	Ink Type		
Printer Passes #	20 wt.% Pt|C EG $[m^2_{Pt}/g_{Pt}]$	20 wt.% Pt|C Gly $[m^2_{Pt}/g_{Pt}]$	46.7 wt.% Pt|C Gly $[m^2_{Pt}/g_{Pt}]$
5	71	56.5 ± 0.7 [1]	47.1 ± 3.7 [2]
10	55.8	40.7 ± 1.9 [2]	32.7 ± 3.9 [1]
15	49.9 ± 1.4 [1]	33.1 ± 1.4 [2]	30.3 ± 0.9 [1]
20	44.6	33.9 ± 1.6 [1]	25.1

is twice as thick as the 46.7 wt.% Pt|C or due to the difference in carbon support [120]. There is also a significant effect with varying solvents. In order to more easily see the trends in Table 4.3, Figure 4.9 has also been included. Here it is possible to see the relatively large decrease in ECSA between 5 layer CLs and 10 layer CLs, this rate of decreasing activity then begins to reduce at higher printer passes (10 to 20 layers).

To use the above ECSAs in the mathematical model they need to be converted into active area of Pt per cm^3 of catalyst layer, (A_v). This is achieved by using Equation (3.28), allowing us to see the volumetric activity of the layer, as shown in Figure 4.10. The figure shows that increasing the wt.% of Pt|C increases the volumetric active area by almost three times. However, more interestingly when observing the EG solvent the rate of decrease in the CLs A_v is relatively low compared to the Gly solvent. Indicating that with EG the CLs volumetric active area remains relatively high with increasing Pt content (thickness), an attribute not observed when using Gly ink which reduces by 40% when comparing the 5 and 20 layer CLs for both 20 wt.% and 46.7 wt.% Pt|C .

4.1.2.4 Relative Humidity vs. Electrochemical Surface Area

To further characterize the electrodes, the ECSA vs. RH is investigated for two separate samples with 30 wt.% ionomer loading. The cell temperature was maintained constant at 50 °C while the dew point of the feed gases were altered to give the desired RH. To let the cell fully acclimatize the humidified feed gas were supplied at the desired RH for an hour prior to CV tests. The process was then repeated twice for both cells to acquire the STDEV. It can be observed in Figure 4.11 that no noticeable effects of RH are observed for 30 wt.% ionomer content CLs. This differs

[1] Two samples
[2] Three samples

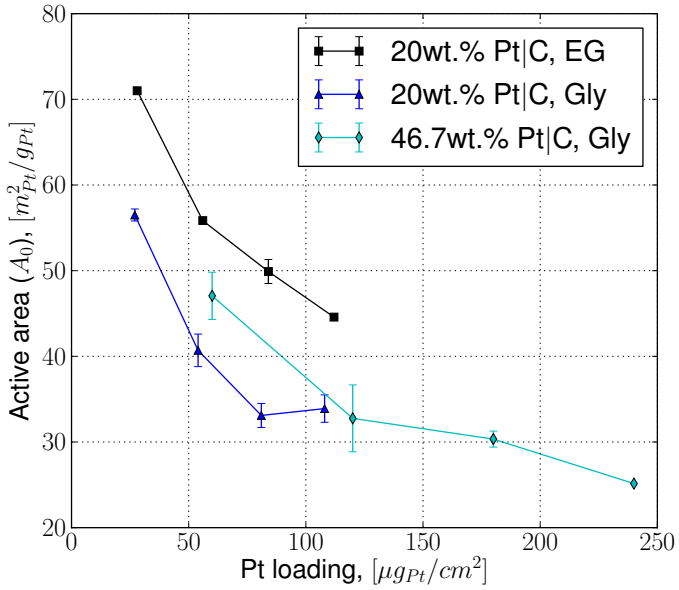

Figure 4.9 – Effect of Pt loading and concentration on ECSA (A_0) of 30 wt.% Nafion® content electrodes

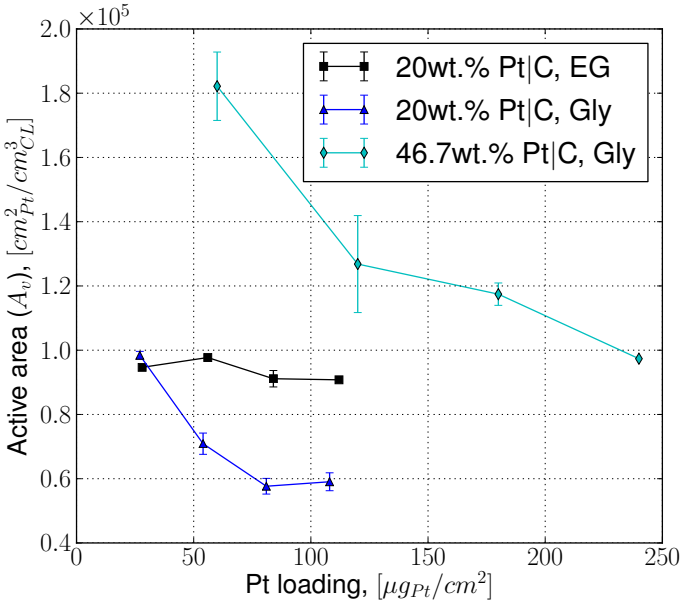

Figure 4.10 – Effect of Pt loading and concentration on ECSA (A_v) of 30 wt.% Nafion® content electrodes

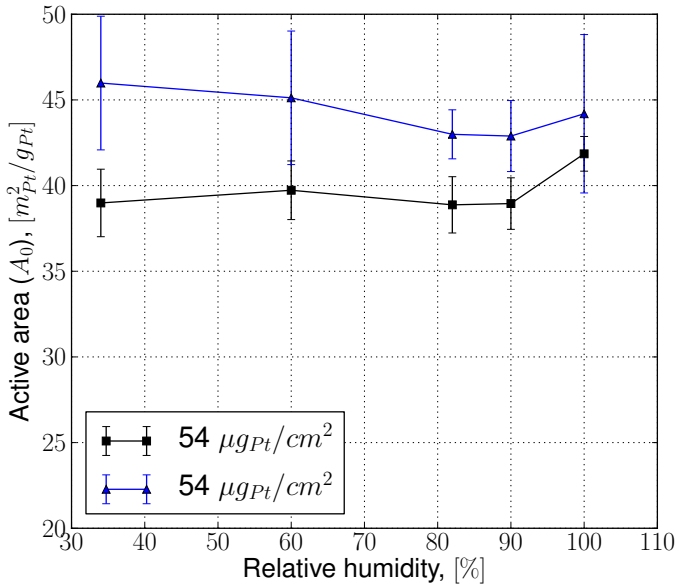

Figure 4.11 – Effect of RH on ECSA, with 30 wt.% NL, 20 wt.% Pt|C Vulcan XC-72, and Gly solvent.

from conventional layers showing higher sensitivity [120]. In this study Soboleva et al. [120] investigated the effect on ECSA with carbon support, ionomer loading, and RH. The low sensitivity seen in low Pt content IJP CLs is very advantageous in terms of commercial applications reducing the demand on fuel cell balance of plant.

4.1.2.5 ECSA of Functionally Graded Electrodes

In this work, functionally graded CLs have also been examined. It was found that for similar loadings functionally grading could enhance the ECSA of the CL. Figure 4.12 compares a homogeneous CL with 30 wt.% NL against a functionally graded CL with equivalent averaged NL of 30 wt.%.

The functionally graded electrodes have 5 layers consisting of 20 wt.% NL and also 5 layers with 40 wt.% NL on either the inner or outer layers. The functionally graded CL with the highest NL on the inner layer (ML|40|20) showing best results, with a 28% increase in ECSA compared to the equivalent homogeneous electrode.

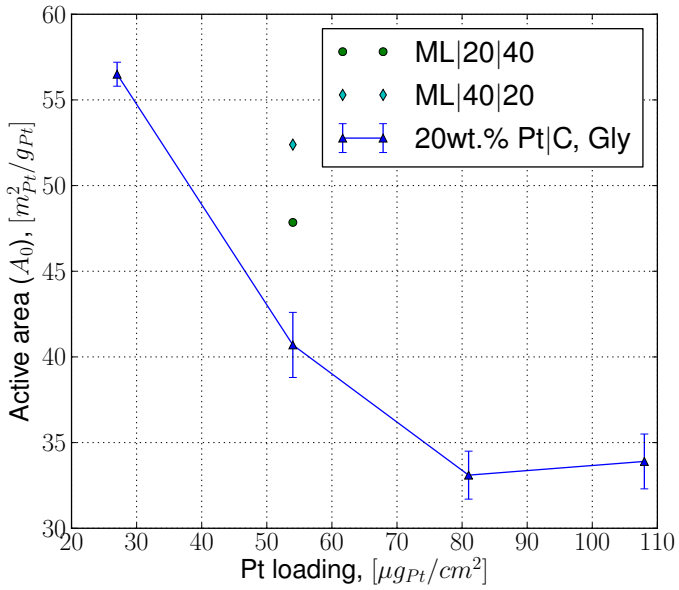

Figure 4.12 – Effect of functionally grading NL on ECSA, 20 wt.% Pt|C Vulcan XC-72, and Gly solvent. Functionally graded showing significant increases in ECSA for the same content of ionomer and Pt.

4.2 Homogeneous Pt Loading Study

The goal of the homogeneous Pt loading study is to investigate the effect on performance and mass activity with increasing catalyst content in the CCL . In addition a mathematical model is used to simulate the various Pt loadings in order to see if the model can accurately capture the changes in performance with Pt content. To do this two kinetics models are used, *i.e.*, Tafel kinetics (TK) and double-trap kinetics (DTK) model. In this section the low Pt content electrode experimental results are compared to simulations predictions using DTK model and the traditional TK model for various Pt loadings, with particular focus on the kinetic region.

4.2.1 Experimental Results

Increasing the amount of Pt in the CL will typically increase the amount of available reaction sites. Therefore, at a fixed cell voltage the larger the platinum content in a CL the greater the current produced, provided sufficient reactant is available.

Figure 4.13 compares the performance IJP CLs with Pt loadings between 27 and

108 $\mu g_{Pt}/cm^2$ using 20 wt.% Pt|C, 30 wt.% NL , and EG/Gly solvent, against a conventional spray coated CL (400 $\mu g_{Pt}/cm^2$). The conventional spray coated CL has been provided in collaboration with the National Research Council Canada - Institute for Fuel Cell Innovation (NRC-IFCI), fabricated with 46.7 wt.% Pt|C Ketjen Black and 30 wt.% NL, using a spray coating method. The cells are tested in house using the equipment described in Section 2.2.2. The conventional CL has also been tested in NRC-IFCI using a parallel flow field arrangement. Comparisons of the differing hardware and test station setups are described in the discussion section. In addition to the 28, 56, and 84 $\mu g_{Pt}/cm^2$ EG electrodes, a 112 $\mu g_{Pt}/cm^2$ was also characterized for ECSA and thickness. However, due to excessive crossover the experimental I-V curves were omitted. The ECSA and thickness results are used later in the mathematical modelling section in order to predict performance allowing the possible limiting phenomenon to be examined.

A significant increase in the kinetic region was observed with increased Pt loading for both solvent types. Increasing the Pt loading of IJP CLs is achieved by increasing the number of printed layers. Printing additional layers will also increases the thickness of the CL. As the thickness of a CL increases it is found to have negative effects in terms of mass transport and charge transport, thereby inhibiting the cells limiting current. This issue can be observed in both EG and Gly IJP CLs with a loading between 54 and 108 $\mu g_{Pt}/cm^2$, showing little to no increase in limiting current.

4.2.2 Modelling Results

In this work several Pt loading electrodes have been fabricated and tested. The aim of this section is to see if OpenFCST's non-isothermal MEA model using the new DTKs model can accurately predict the change in performance with Pt loading. Figure 4.14 shows MEA predicted performance of the DTK and TK models at different Pt loadings observed when using EG ink. Simulation parameters for this study can be found in Table 3.2 to 3.9. The dashed part of the polarization curve indicates that the RH in the cathode is higher than 100%.

Both kinetics models capture the decreasing performance with reduced Pt content, however, the TK model predicts a larger change in performance with Pt loadings. To investigate why the TK model fails to capture the large decrease in performance compared to the DTK model, contour plots for the lowest loading of 28 $\mu g_{Pt}/cm^2$ are compared.

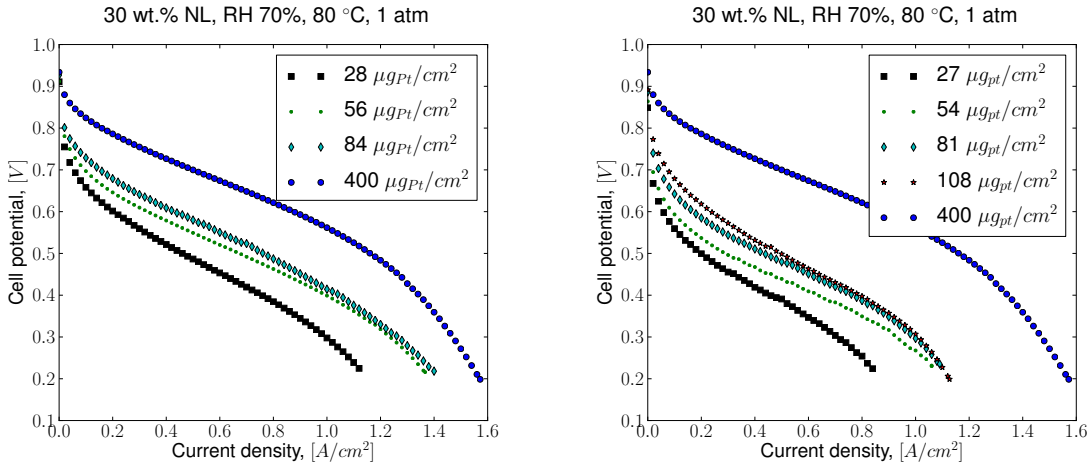

(a) (b)

Figure 4.13 – Experimental Pt loading comparison of conventional spray coated CCL (400 $\mu g_{Pt}/cm^2$) with low Pt loading IJP CLs for EG (a) and Gly (b) solvent. Showing increasing kinetic region with increased Pt loading and the onset of mass/charge transport issues with increasing CCL thickness.

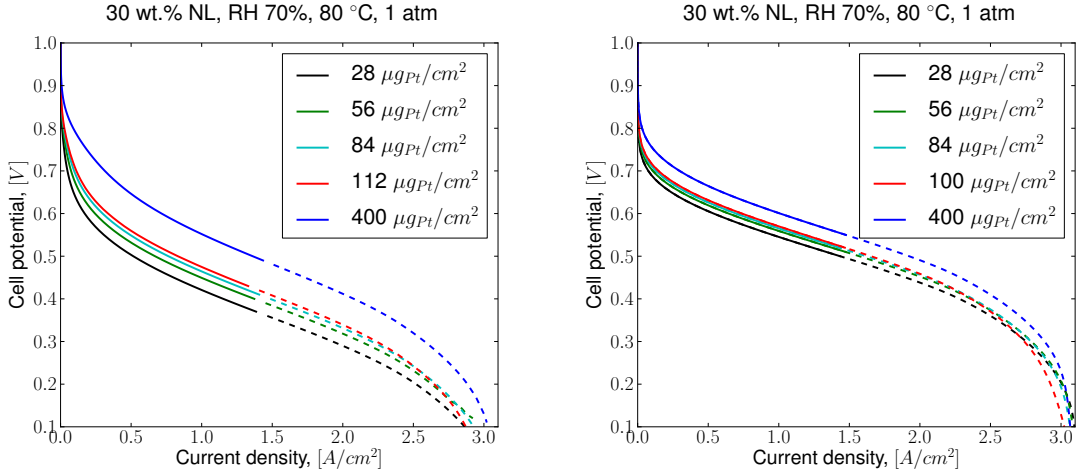

(a) Double-trap kinetics (b) Tafel kinetics

Figure 4.14 – Qualitative comparisons of simulation and experimental results for 28-112 $\mu g_{Pt}/cm^2$. Where the DTK model shows good prediction of the performance drop with Pt loading, while TK fails to capture the drop.

Figure 4.15 shows the contour plots at 28 $\mu g_{Pt}/cm^2$, using the DTKs model (a)-(d) and TK model (e)-(h) at varying current densities. Comparing the two models it is possible to see that due to the slower reaction kinetics, predicted by the DTK model [14] a greater percentage of the CCL is needed to meet the current requirements. This differs greatly from the Tafel reaction kinetics model which predicts a faster reaction rate resulting in a very small portion of the CCL being required to produce the desired current. Hence, decreasing the CCLs loading does not have a large effect according to the TK model as much of the reaction is happening in a very thin section of the CCL. This explains the relatively small drop in performance in the Tafel Pt study in Figure 4.14 (b).

Figure 4.16 shows the current density plots at the kinetic, ohmic, and mass transport region of the various Pt loadings using the DTK model as it more accurately captures the decreasing performance seen experimentally. Observing these plots it is possible to see, for increasing current density and increasing loading (thickness), that the current production gradually migrates to the ML-CCL interface. This localized current is especially predominant in the conventional loading CL.

The calculated porosity obtained using for the 28, 56, 84, 112, and 400 $\mu g_{Pt}/cm^2$ CLs are 58, 45, 43, 36, and 56 % respectively. The 20 layer (112 $\mu g_{Pt}/cm^2$) CL having the lowest porosity is, as expected the cell which begins to observe initial reductions in oxygen mole fraction, seen in Figure 4.17. This reduced porosity is the main contribution to the 20 layer cell having one of the lower limiting currents. However, the oxygen mole fractions (x_{O_2}) are not low enough at 1.0 A/cm^2 to cause the current migration toward the ML-CCL interface.

To explain the current migration across the CCL, the protonic potential plots (ϕ_m) are required, as seen in Figure 4.18. ϕ_m represents the amount of protonic transfer loss across the CCL, therefore, the larger the protonic loss the more negative the ϕ_m value. When comparing the maximum ϕ_m losses in the 2.1 μm thick, 28 $\mu g_{Pt}/cm^2$ CL (0.074 mV) against the 10 μm thick conventional CL (0.1 mV) where ϕ_m losses are 35% greater. The ϕ_m plots show a relatively low ϕ_m loss from bottom left of the contour plot Figure 4.18 (a) to top right corner of the 2.1 μm CL, with largest losses occurring at the top right corner. In contrast, the 10 μm CL has a much larger ϕ_m loss over a greater area, Figure 4.18 (e), leading to lower overpotentials which make it difficult to produce current at the CL-GDL interface, as seen in Figure 4.19.

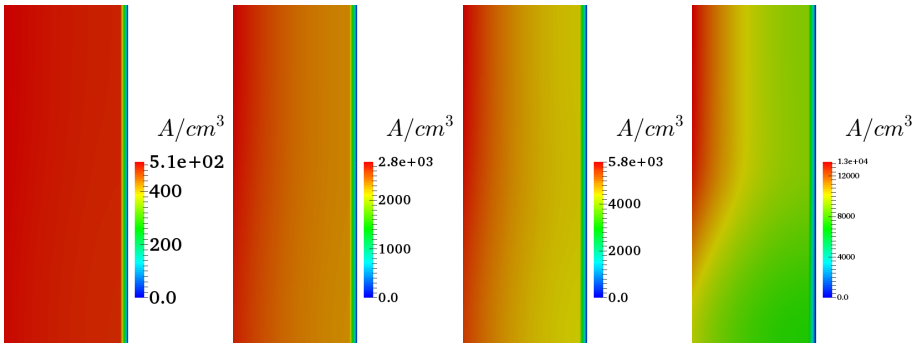

(a) 0.1 $[A/cm^2]$ (b) 0.5 $[A/cm^2]$ (c) 1.0 $[A/cm^2]$ (d) 2.0 $[A/cm^2]$

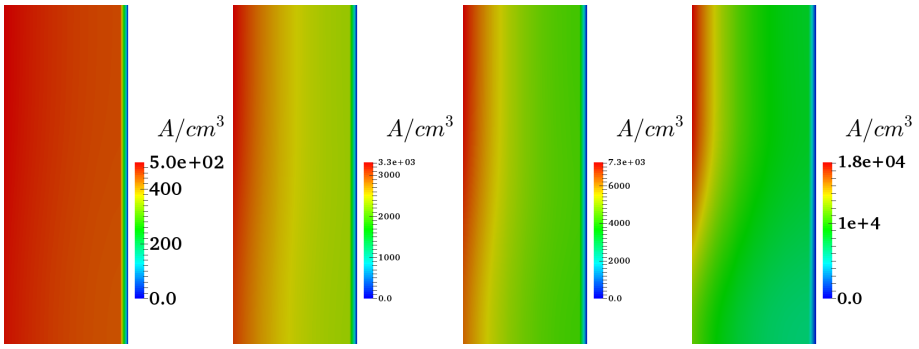

(e) 0.1 $[A/cm^2]$ (f) 0.5 $[A/cm^2]$ (g) 1.0 $[A/cm^2]$ (h) 2.0 $[A/cm^2]$

Figure 4.15 – Current density contour plots comparing DTK model (a)-(d) and TK model (e)-(h) at varying current densities. Where the DTK model requires a larger portion of the CCL in order to meet the current requirements. The zero current density along the right edge is a post process artifact caused by zero current in the MPL.

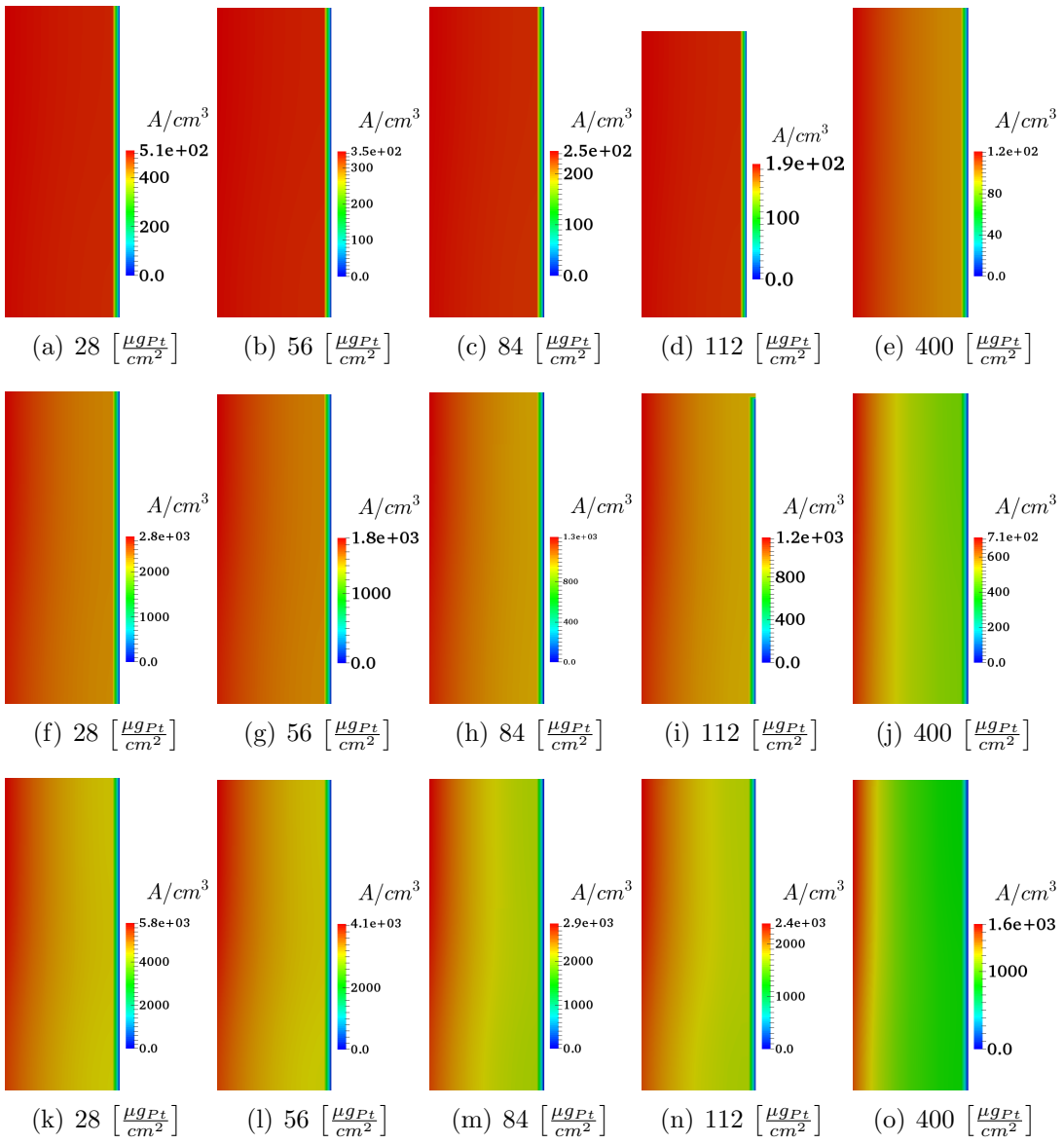

(a) 28 $\left[\frac{\mu g_{Pt}}{cm^2}\right]$ (b) 56 $\left[\frac{\mu g_{Pt}}{cm^2}\right]$ (c) 84 $\left[\frac{\mu g_{Pt}}{cm^2}\right]$ (d) 112 $\left[\frac{\mu g_{Pt}}{cm^2}\right]$ (e) 400 $\left[\frac{\mu g_{Pt}}{cm^2}\right]$

(f) 28 $\left[\frac{\mu g_{Pt}}{cm^2}\right]$ (g) 56 $\left[\frac{\mu g_{Pt}}{cm^2}\right]$ (h) 84 $\left[\frac{\mu g_{Pt}}{cm^2}\right]$ (i) 112 $\left[\frac{\mu g_{Pt}}{cm^2}\right]$ (j) 400 $\left[\frac{\mu g_{Pt}}{cm^2}\right]$

(k) 28 $\left[\frac{\mu g_{Pt}}{cm^2}\right]$ (l) 56 $\left[\frac{\mu g_{Pt}}{cm^2}\right]$ (m) 84 $\left[\frac{\mu g_{Pt}}{cm^2}\right]$ (n) 112 $\left[\frac{\mu g_{Pt}}{cm^2}\right]$ (o) 400 $\left[\frac{\mu g_{Pt}}{cm^2}\right]$

Figure 4.16 – Current density contour plots of the Pt loading study at varying current densities. (a)-(e) at 0.1 A/cm^2, (f)-(j) at 0.5 A/cm^2, (k)-(o) at 1.0 A/cm^2. Where the increasing Pt loading (thickness) the current is seen to migrate to the ML-CCL interface. The zero current density along the right edge is a post process artifact caused by zero current in the MPL.

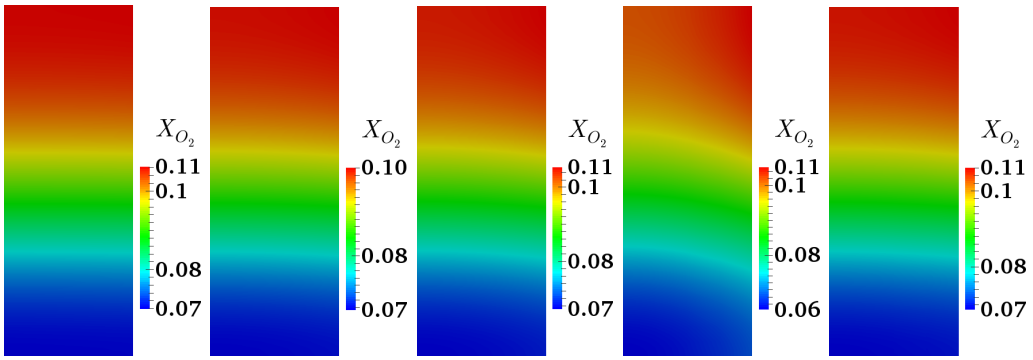

(a) 28 $\left[\frac{\mu g_{Pt}}{cm^2}\right]$ (b) 56 $\left[\frac{\mu g_{Pt}}{cm^2}\right]$ (c) 84 $\left[\frac{\mu g_{Pt}}{cm^2}\right]$ (d) 112 $\left[\frac{\mu g_{Pt}}{cm^2}\right]$ (e) 400 $\left[\frac{\mu g_{Pt}}{cm^2}\right]$

Figure 4.17 – Oxygen mole fraction contour plots of the Pt loading study at 1.0 A/cm^2, initial mass transport issues being seen in 112 $\left[\frac{\mu g_{Pt}}{cm^2}\right]$ CL.

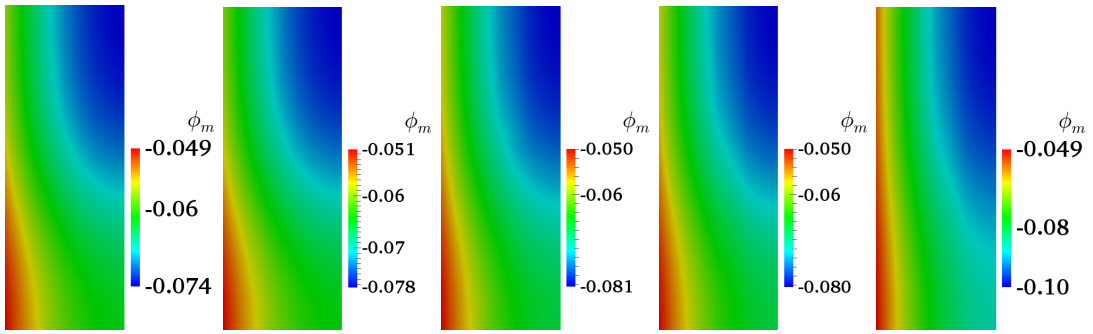

(a) 28 $\left[\frac{\mu g_{Pt}}{cm^2}\right]$ (b) 56 $\left[\frac{\mu g_{Pt}}{cm^2}\right]$ (c) 84 $\left[\frac{\mu g_{Pt}}{cm^2}\right]$ (d) 112 $\left[\frac{\mu g_{Pt}}{cm^2}\right]$ (e) 400 $\left[\frac{\mu g_{Pt}}{cm^2}\right]$

Figure 4.18 – Protonic potential contour plots of the Pt loading study at 1.0 A/cm^2, where ϕ_m losses increase with CL Pt loading (thickness).

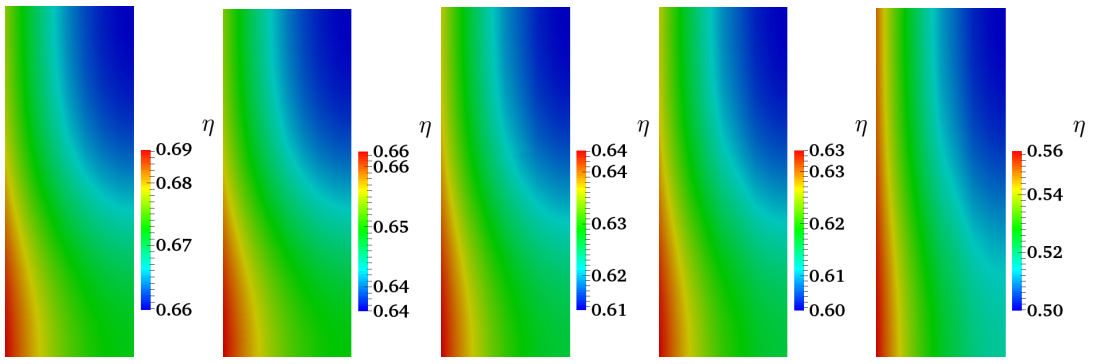

(a) 28 $\left[\frac{\mu g_{Pt}}{cm^2}\right]$ (b) 56 $\left[\frac{\mu g_{Pt}}{cm^2}\right]$ (c) 84 $\left[\frac{\mu g_{Pt}}{cm^2}\right]$ (d) 112 $\left[\frac{\mu g_{Pt}}{cm^2}\right]$ (e) 400 $\left[\frac{\mu g_{Pt}}{cm^2}\right]$

Figure 4.19 – Overpotential contour plots of the Pt loading study at 1.0 A/cm^2, where lowest overpotentials are located at the CCL-GDL interface.

4.2.3 Discussion

The experimental and simulated DTK results are shown side by side in Figure 4.20 for a qualitative comparisons of the results. The simulated results capture the large performance gap between the low Pt loading inkjet CLs and the conventional spray coated CL. In terms of the limiting current the simulated data has a much greater and unrealistic limit of 3 A/cm^2. This over prediction is due to several reasons, such as, calculated effective diffusion values in the diffusion media and CCL, calculated porosity of the CLs, and liquid water content and multi-component transport effects which are not taken into consideration.

Effective diffusion values are calculated from the porosity where the CL porosity is calculated using the material density and CL thickness which are sensitive to error, as oppose to using experimentally obtained diffusion data. In addition, the absence of liquid water in the model produces super-saturated gas ($>$ 100% RH) represented by the dashed line in the simulated polarization curves. These all aid in the over-prediction of current in the mass transport region. However, in terms of the limiting current trends, the model captures the convergence of the limiting current for the inkjet CLs as seen in experimental curves.

In order to compare the simulated and experimental curves quantitatively. Figure 4.21 is provided for the respective loadings, showing both kinetic model types. When comparing the 28 $\mu g_{Pt}/cm^2$ cell, the DTK model more accurately predicts the performance drop showing a much closer approximation to the kinetic and initial ohmic region. In contrast the TK fails to predict the drop in current density. In the later ohmic region the DTK results then begins to diverge away from the experimental data due to the onset of mass transport issues, for reasons explained previously.

As the Pt loading increases the DTK model begins to under predict the experimental data, showing greater under prediction as the loadings increase. The DTK model however is shown to better predict the overall trends. The under prediction is thought to occur due to the serpentine flow field channel effects. To support this claim the NRC-IFCI cell with serpentine and parallel (Paral) flow field arrangements are compared in Figure 4.21 (d). In parallel channel arrangement the cross channel pressure gradients and convective flow are consider negligible [14, 17, 79]. This assumption is considered reasonable as the fluid moves across the channel the pressure drop is in the direction of fluid flow, therefore at each section of the flow each

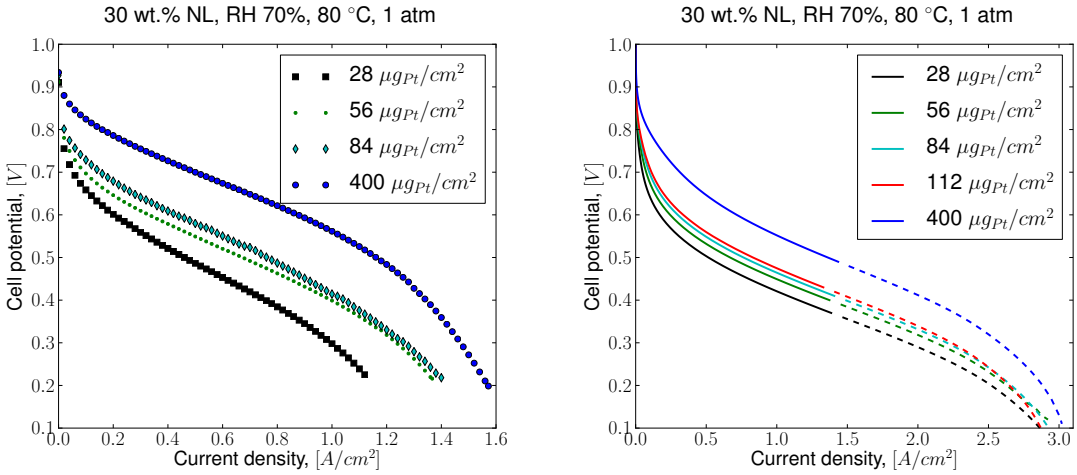

(a) Experimental trends

(b) Simulated trends

Figure 4.20 – Qualitative comparisons of simulation and experimental results for 28-112 $\mu g_{Pt}/cm^2$ Pt loading.

channel should have close to equal pressure ($P_1 \approx P_2$), as seen in Figure 4.22 (a). Using the parallel flow channel experimental data and comparing against the predicted simulated performance shows closer prediction, as the mathematical model assumes negligible pressure gradients between channels.

In serpentine flow field arrangement, a pressure drop is present perpendicular to the direction of fluid flow, as seen in Figure 4.22 (b), causing convective flow to occur between channels (represented by the white arrows). Convective flow through the diffusion media can increase the local (O_2) concentration, thereby increasing kinetics and can remove liquid water from under the BPP-GDL contact region (land). Therefore, when comparing the conventional spray coated CL data using the parallel flow field, the DTK shows the closest prediction compared to the TK.

The over-prediction of the TK can be explained recalling the observations in Figure 4.15. Due to the 'fast' reaction kinetics the TK only requires a small section of the CCL in order to produce the required current. This is not the case for the DTK whereby it requires more of the CCL. Therefore, the Pt reduction and hence thickness reduction has a larger impact using the DTKs model.

Increasing the Pt content resulted in an increase in performance, however it is important to try retain the high mass activity as seen in the low Pt loading 28 $\mu g_{Pt}/cm^2$

(5 layer) CL. Figure 4.23 shows that with increasing catalyst content the mass activity gradually decreases. The reason for this gradual decrease is the reduced uniformity of the reaction, as shown in Figure 4.16, resulting from the increased protonic transport losses. This is an unfavourable trend, to counteract this trend functionally graded CLs will be investigated in later sections.

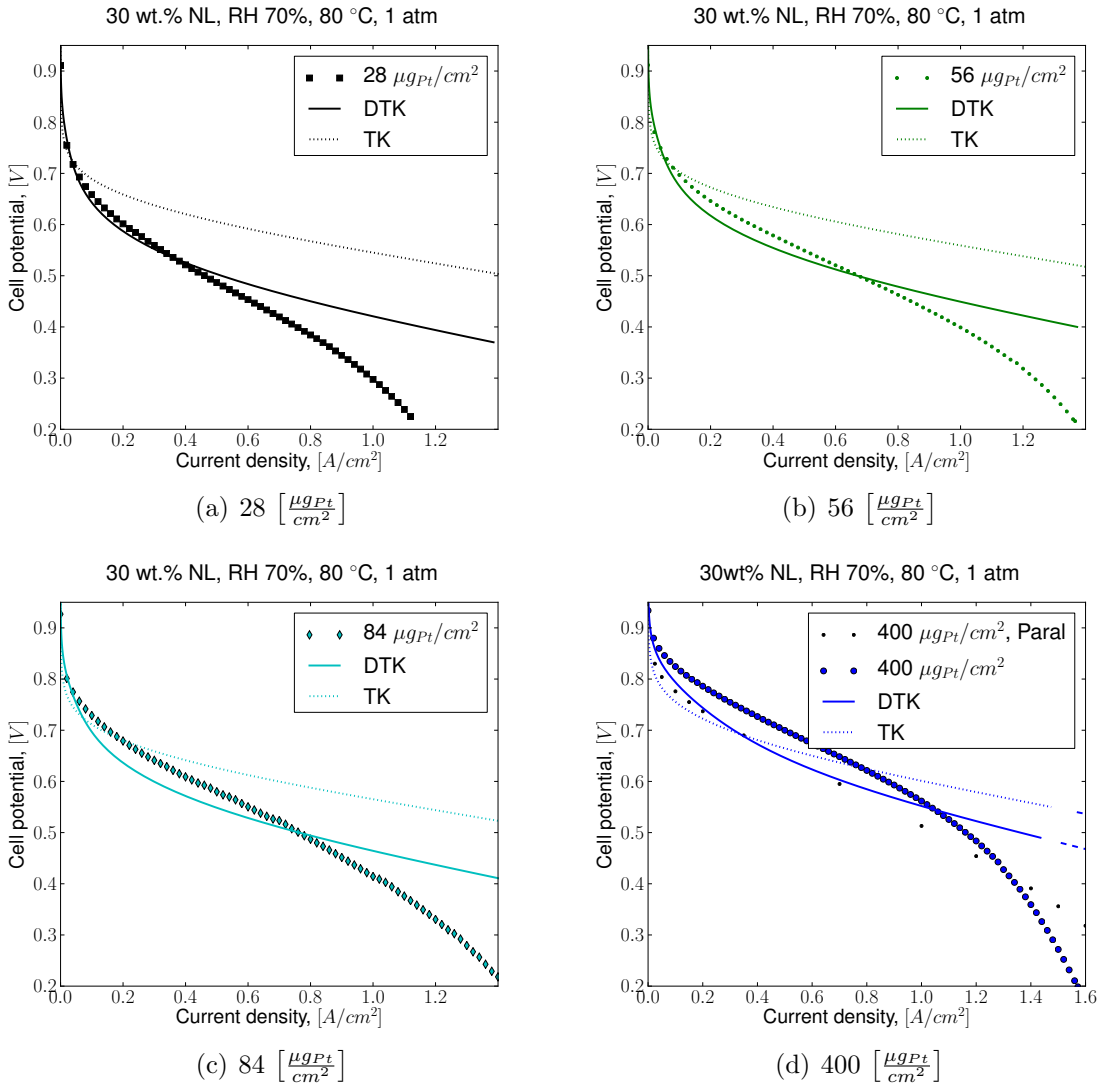

(a) 28 $\left[\frac{\mu g_{Pt}}{cm^2}\right]$

(b) 56 $\left[\frac{\mu g_{Pt}}{cm^2}\right]$

(c) 84 $\left[\frac{\mu g_{Pt}}{cm^2}\right]$

(d) 400 $\left[\frac{\mu g_{Pt}}{cm^2}\right]$

Figure 4.21 – Quantitative comparisons of simulation and experimental results for 28 - 400 $\mu g_{Pt}/cm^2$, using both DTK model and TK model. NRC-IFCI CL (d), showing both serpentine and parallel (Paral) flow arrangements

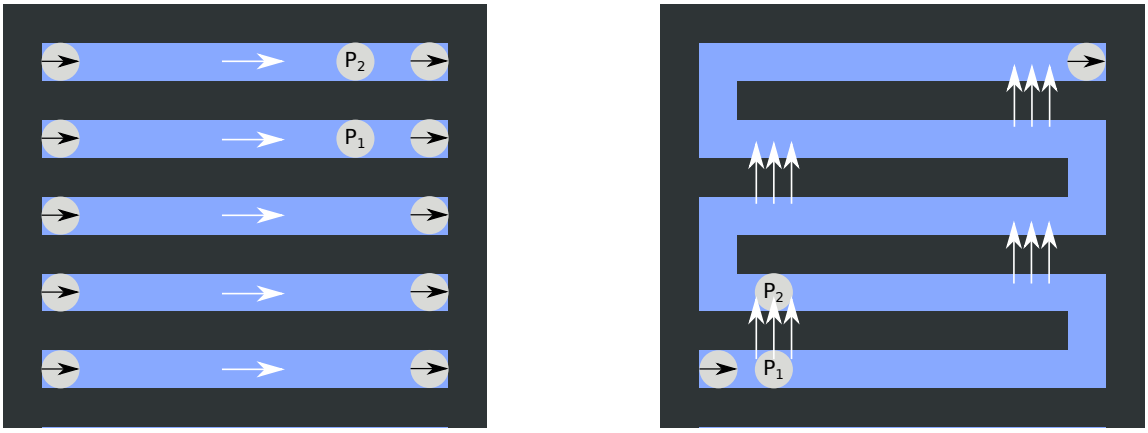

(a) Parallel channel (b) Serpentine channel

Figure 4.22 – Serpentine and parallel flow field geometry. Illustrating the negligible drop in parallel flow field arrangement (a), compared to the pressure drop between channels in serpentine flow field (b).

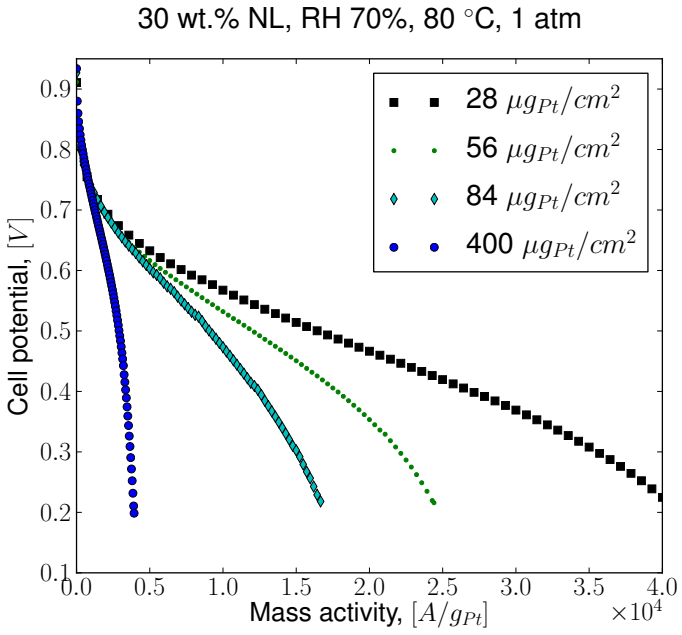

Figure 4.23 – Mass activity of the various Pt loading CCLs

.

4.3 Homogeneous Nafion® Loading Study

4.3.1 Experimental Results

In conventional CCLs protonic conductivity and ECSA have a significant sensitivity to NL [40, 44]. Until recently the effect of NL on low Pt loading IJP electrodes was unknown. Shukla et al. [1] investigated the NL and found that these low Pt content electrodes (27 $\mu g_{Pt}/cm^2$) have low sensitivity to the amount of ionomer present, with the exception of the extreme cases of 10 and 50 wt.% NL where ionomer coverage and porosity issues arise. This low sensitivity can be seen in Figure 4.24 where ionomer loadings of 20 to 40 wt.% show similar performances at 80 °C, 70% RH.

Table 4.4 shows the low change in ECSA for ionomer loadings greater than 20 wt.%. At 10 wt.% NL, a significant reduction in ECSA is recorded. This reduction is possibly due to the inadequate coverage of ionomer leading to more inactive platinum sites, a phenomenon also observed in the work of Soboleva et al. [120]. The optimum loading in Shukla et al.'s earlier work found the best ionomer loading at 40 wt.%. This differs from conventional CLs where the optimum is found close to ≈ 35 wt.% [40, 44]. In conventional CLs there is a trade-off between protonic transport and mass transport limitations. The trade-off arises from the relatively large thickness of conventional CLs (10 μm) roughly five times thicker compared to that of low Pt loading thin electrodes fabricated in this work having thickness of 1.55 - 5.5 μm. In these thinner CLs, mass transport limitations are reduced. This allows the low Pt content electrodes to have higher percentage of ionomer content promoting protonic transport without resulting in greater mass transport losses, which would otherwise occur in conventional CLs. In addition, the reduced thickness of low Pt content electrodes results in a shorter transport path for the protons further reducing operating losses.

Table 4.4 – Effect of NL on ECSA [1]

Nafion® loading wt.%	Active area $[m^2_{Pt}/g_{Pt}]$	Pt loading $[\mu g_{Pt}]$
10	46.1	27.2 ± 2
20	58.4	27.2 ± 2
30	60.5	27.2 ± 2
40	56.6	27.2 ± 2
50	52.3	27.2 ± 2

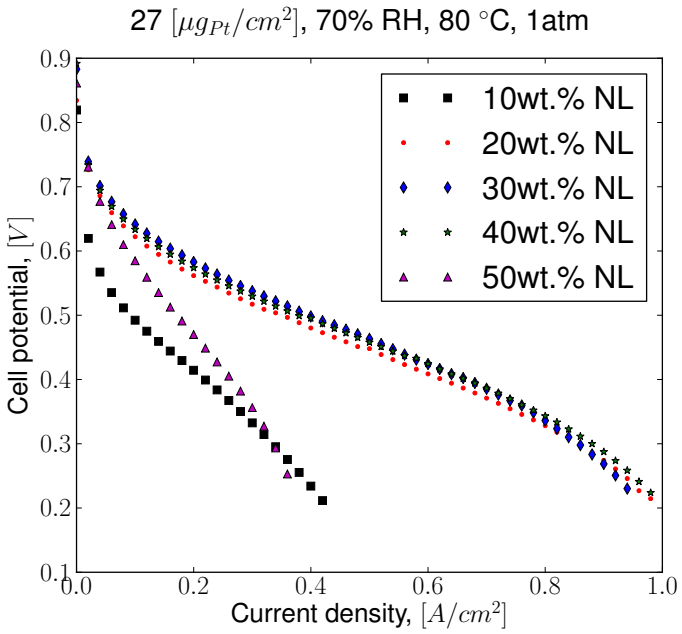

Figure 4.24 – Experimental NL study polarization curves, showing low sensitivity to ionomer content, with the exception of the extreme cases where ionomer coverage (10 wt.%) and porosity (50 wt.%) issues arise [1].

4.3.2 Modelling Results

The goal of simulating the ionomer loading work by Shukla et al. [1] is to understand if the mathematical model can accurately predict the experimental trends. Successful prediction of these ionomer trends will provide evidence that the mathematical model is capturing the predominant phenomenon. The contour plots of these simulations can then be examined to gain a deeper understanding about what is causing the change in performance. Once the cause has been found, the model can be used to direct the optimum cell properties.

Simulations for the MEAs are performed using the parameters in Section 3.3 and experimental data obtained from Table 4.4. Figure 4.25 shows the simulated results for different ionomer loadings. The results show that the best performance is achieved with CLs having a NL of 30 - 40 wt.%. The CL containing 20 wt.% ionomer begins to experience increased protonic losses due to the low ionomer content, an effect which is also observed in the experimental data. The model also predicts the 10 wt.% and 50 wt.% performing much worse, a trend which is also seen in conventional CLs [40].

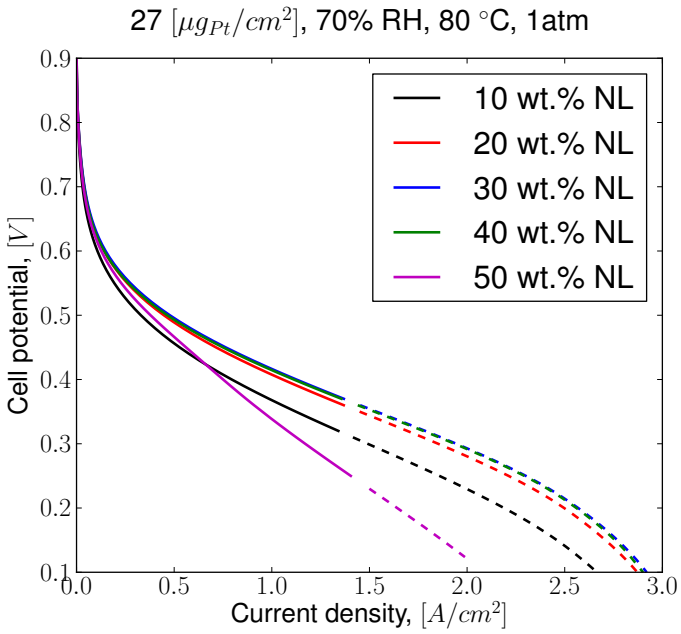

Figure 4.25 – Simulated NL study polarization curves, showing low sensitivity to ionomer content, with the exception of the extreme cases where proton transport (10 wt.%) and porosity (50 wt.%) issues arise.

Using OpenFCST's non-isothermal MEA model it is possible to visualize the phenomenon causing the change in performance, by viewing contour plots of the relevant variables. Figure 4.26 illustrates the current density of the CLs with varying loadings, for kinetic (a) - (e), ohmic (f) - (j), and mass transport region (k) - (o). With increasing NL, an increase in the uniformity of current production can be observed across the CL up to 40 wt.% NL.

At the ohmic region and mass transport region of the 10 wt.% NL case the majority of its current generation is present near the ML-CCL interface, while the 50 wt.% NL shows the majority of its current generation near the CCL-GDL interface. In contrast, the 40 wt.% NL electrode the current is found to be uniformly distributed across cross section.

To investigate the 10 wt.% and 50 wt.% NL and the increased uniformity of current production from 20 wt.% to 40 wt.%, several contour plots are examined. From this investigation the protonic potential (ϕ_m) and oxygen mole fractions (x_{O_2}) plots were found to have the greatest impact on performance.

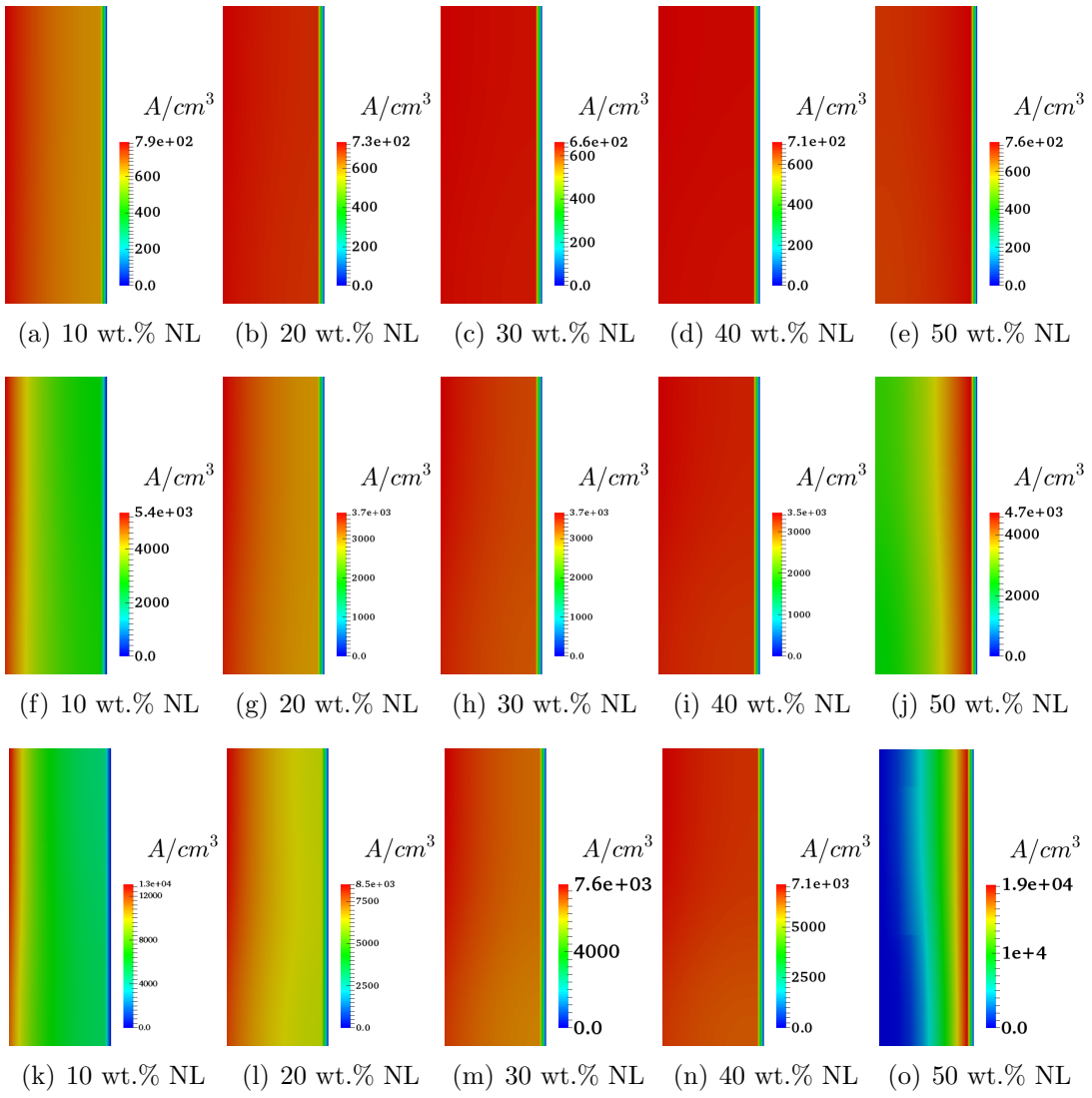

(a) 10 wt.% NL (b) 20 wt.% NL (c) 30 wt.% NL (d) 40 wt.% NL (e) 50 wt.% NL

(f) 10 wt.% NL (g) 20 wt.% NL (h) 30 wt.% NL (i) 40 wt.% NL (j) 50 wt.% NL

(k) 10 wt.% NL (l) 20 wt.% NL (m) 30 wt.% NL (n) 40 wt.% NL (o) 50 wt.% NL

Figure 4.26 – Current density contour plots for NL study at varying current densities. (a)-(e) at 0.1 A/cm^2, (f)-(j) at 0.5 A/cm^2, (k)-(o) at 1.0 A/cm^2. Current production is seen at the ML-CCL at 10 wt.% NL due to large protonic losses. The most uniform current production at 40 wt.% NL. Due to oxygen depletion at 50 wt.% NL current production is seen at the CCL-GDL interface. The zero current density along the right edge is a post process artifact caused by zero current in the MPL.

In the case of the 10 wt.% NL, the oxygen mole fraction contour plot in Figure 4.27 (a), shows high oxygen concentrations everywhere in the electrode with higher oxygen concentrations under the channel area. This high level of x_{O_2} demonstrates that reactant depletion is not the cause of poor cell performance. Figure 4.28 (a) shows a very large decrease in membrane potential due to the high resistance to proton transport. It is clear that for the 10 wt.% NL electrode, protonic transport is the limiting phenomenon, as the ϕ_m substantially drops across the electrode, showing a maximum loss of 120 mV. This large ϕ_m loss in the 10 wt.% case makes it undesirable to produce current away from the ML-CCL interface. Therefore, the majority of the current production is to the left of the CCL where protons have less distance to travel and overpotentials are high, as seen in Figure 4.29. In contrast, the 50 wt.% NL case has relatively low ϕ_m losses across the CL, showing a maximum loss of 64 mV across the electrode, as seen in Figure 4.28 (e). This decreasing protonic loss with increase ionomer content explains the increased uniformity of current production across the CL.

In terms of x_{O_2} the 10 wt.% ionomer case does not have any issues showing low gradients across the CL Figure 4.27 (a). This is expected as the 10, 20, 30, and 40 wt.% ionomer loading electrodes have porosity of 59, 53, 46, and 35 %, respectively. The 50 wt.% case, however, has a porosity of 26.7% approaching the porosity threshold ($\varepsilon_{th} = 25.9\%$) set in Section 3.1.2. Using Figure 3.1 it is possible to see that the effective diffusion is very low. This low effective diffusion in the CCL causes large areas of the CL to be oxygen depleted (starved) even at low current density (0.5 A/cm^2), as seen in Figure 4.27 (e). Due to the low diffusivity the majority of available reactant is being consumed at the CCL-GDL interface. The result is that all of the current is produced on the right side of the CCL where reactant is available closest to the channel.

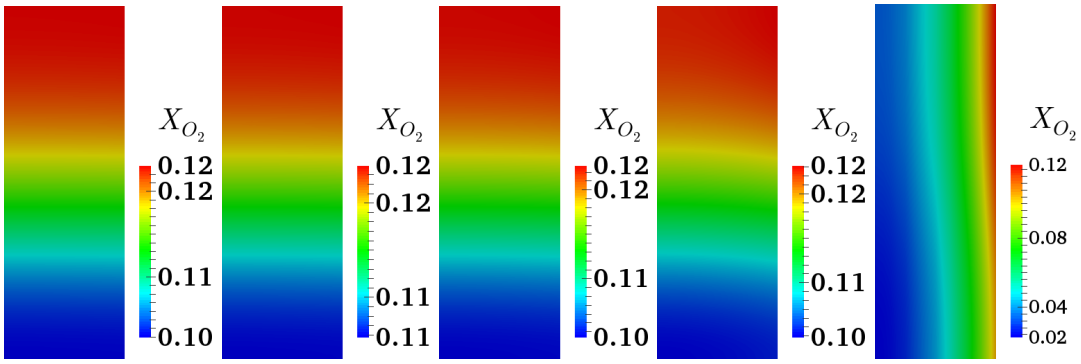

(a) 10 wt.% NL (b) 20 wt.% NL (c) 30 wt.% NL (d) 40 wt.% NL (e) 50 wt.% NL

Figure 4.27 – Oxygen mole fraction contour plots for NL at 0.5 A/cm^2. Oxygen mole fraction gradient change at high NL content.

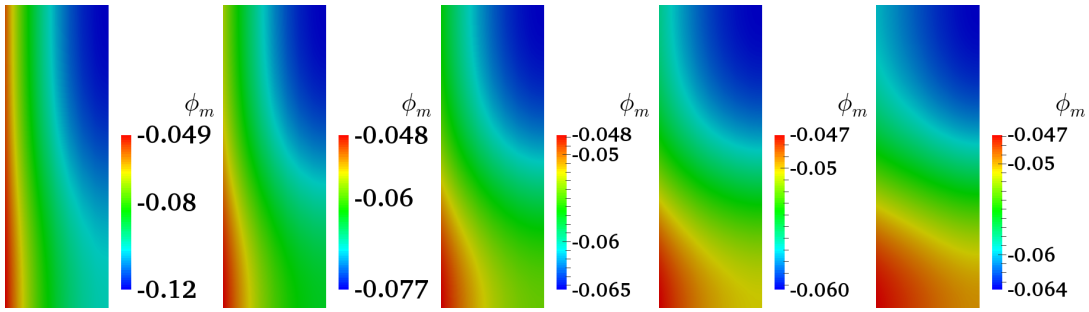

(a) 10 wt.% NL (b) 20 wt.% NL (c) 30 wt.% NL (d) 40 wt.% NL (e) 50 wt.% NL

Figure 4.28 – Protonic potential contour plots for NL at 1.0 A/cm^2. Illustrating the protonic gradient change from low to high NL content across the CCL.

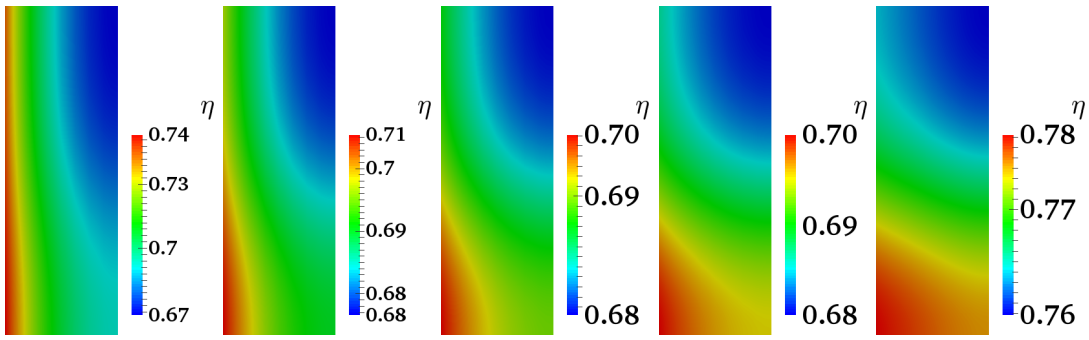

(a) 10 wt.% NL (b) 20 wt.% NL (c) 30 wt.% NL (d) 40 wt.% NL (e) 50 wt.% NL

Figure 4.29 – Overpotential contour plots for NL at 1.0 A/cm^2. Illustrating the gradient change from low to high NL content across the CCL.

4.3.3 Discussion

Comparing the experimental and simulated results qualitatively, as seen in Figure 4.30 matching trends are observed. Both showing similar performance for ionomer loadings of 20 to 40 wt.%, while poor performance for the extreme 10 and 50 wt.% cases, which were found as a result of poor proton conductivity in the 10 wt.% ionomer case and mass transport for the 50 wt.% case.

Figure 4.31 compares the ionomer loading results quantitatively. For the 20 to 40 wt.% cases all kinetic and initial ohmic regions are predicted accurately. Although there is good qualitative agreement, adequate quantitative agreement is not observed between numerical and experimental results, specifically at high current densities.

At high current densities unknown losses are observed possibly due to macro and micro mass transport limitations, as discussed in Section 4.2.3. In addition, Greszler et al. [57] conducted a study on the effect of cathode Pt loading (400 - 30 $\mu g_{Pt}/cm^2$) on oxygen transport resistance finding that along with the bulk transport resistance through the CL pores, there existed a secondary unknown resistance similar to that of a thin resistive film covering the Pt. Greszler et al. [57] found this resistive film to be $\sim 35\ nm$, however, only a maximum of 2 - 10 nm was found to be possible. Therefore, the authors conclude that ionomers do not behave bulk-like in the electrodes as previously assumed and that there might be a ionomer-gas interface resistance, specifying that further experimentation is required to test this hypothesis.

This slow oxygen dissolution at the gas-ionomer interface was investigate by Suzuki et al. [58] using an agglomerate model, where an order-of-magnitude analysis was conducted using diffusivity and dissolution rates finding that dissolution of reactant into the ionomer is significant for $\sim 100\ nm$. Stating that it is reasonable to hypothesis a gas-ionomer interface resistance, rather than to have excessively large agglomerate diameters. Using OpenFCST's agglomerate model functionally may also be able to investigate this issue, however, in this current work only the macro-homogenous effects are considered neglecting the possible film effects.

For the 50 wt.% case the kinetic region is accurately predicted, however, the curve separates from experimental data earlier due to the early onset of mass transport losses, which are not yet accurately accounted for, as stated previously. In the 10 wt.% case at 70% RH poor prediction of the experimental curve is observed. This

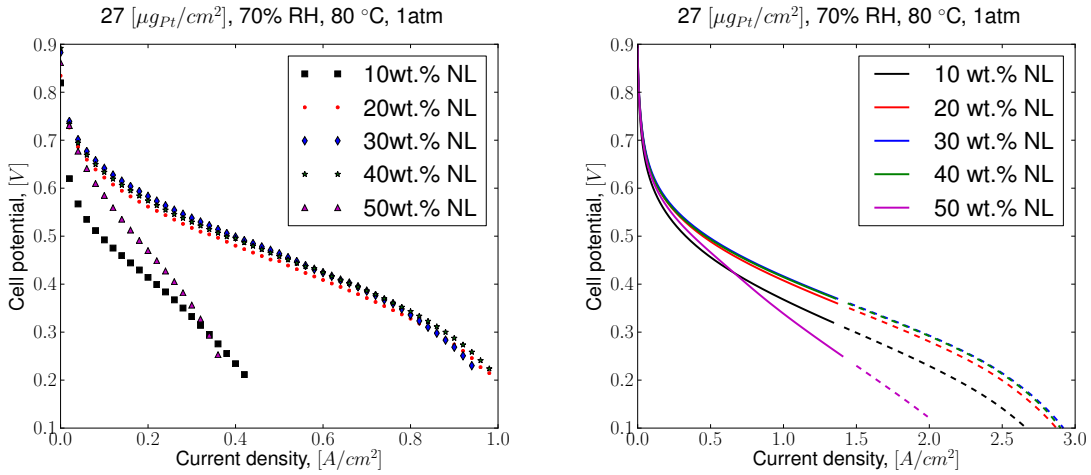

(a) Experimental Trends

(b) Simulated Trends

Figure 4.30 – Qualitative comparisons of simulation and experimental results for varying NL 10 - 50 wt.%.

is considered to be a result of the poor ionomer coverage leading to inactive Pt sites. Soboleva et al. [120] found that ECSA can increase with RH at low ionomer loadings. This increase in ECSA is thought to occur due to the increased water present in the CL pores causing inactive cites to become active while in contact with water, allowing protonic transport. As the ECSA of the CLs is characterized at 100% RH, the 90% RH experimental data is also plotted, Figure 4.31 (b). In the 90% RH case better prediction of the kinetic region is seen.

In summary, good agreement is observed at low current density. At moderate current densities, large deviations exist between model and the experimental data. The reasons for this deviation is currently unknown as mass transport losses are already accounted for in the model. Possible reasons for this discrepancy are macro scale diffusivity values as mentioned in Section 4.2.3, multi-component, convective transport, and micro-scale losses in the form of local mass transport in the agglomerate thin film caused by the dissolution of O_2 in ionomer, Knudsen effects and local build up of liquid water at RH below 100% due to the Kelvin effect.

Shukla et al. investigated the NL in order to further understand the thin, low Pt content CLs and find whether it is possible to increase the performance and mass activity of the CL while keeping the catalyst content low. However, the findings showed that NL has little effect on improving the mass activity of the CCL. Figure 4.32

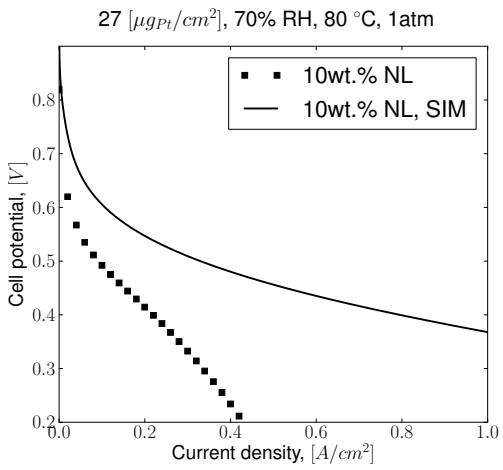

(a) 10 wt.% NL

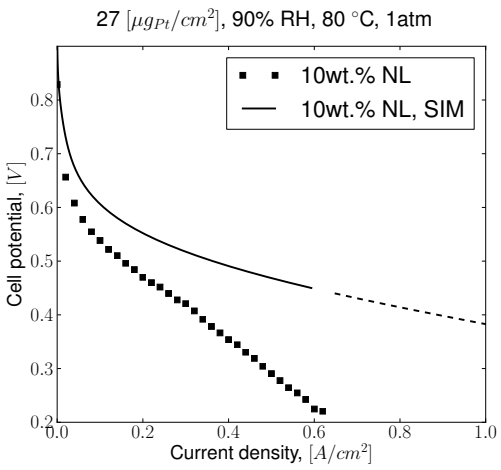

(b) 10 wt.% NL

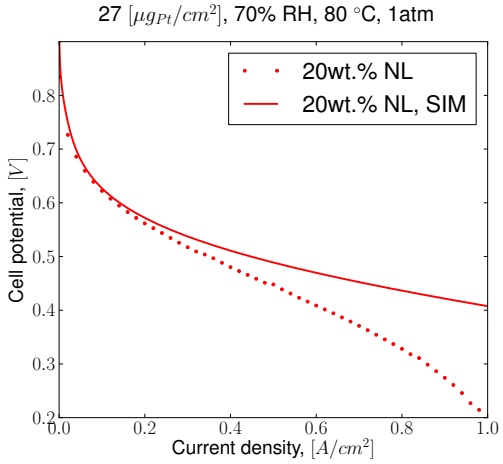

(c) 20 wt.% NL

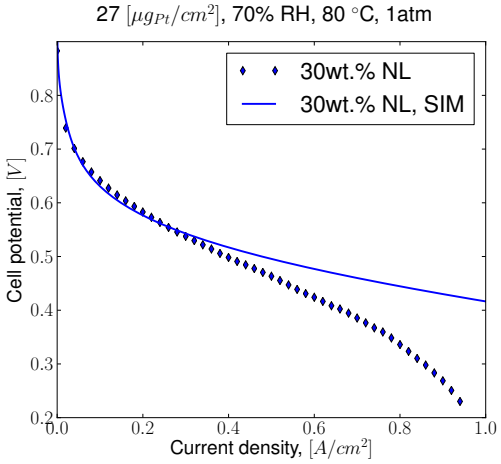

(d) 30 wt.% NL

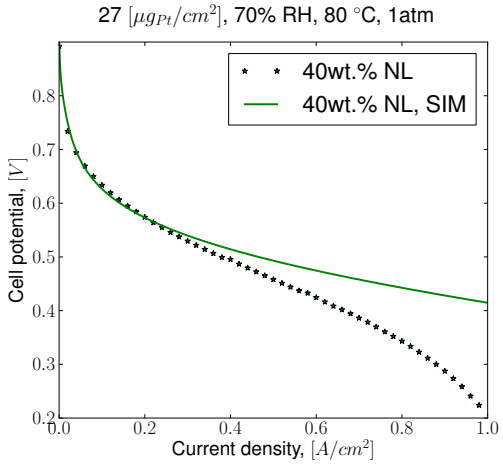

(e) 40 wt.% NL

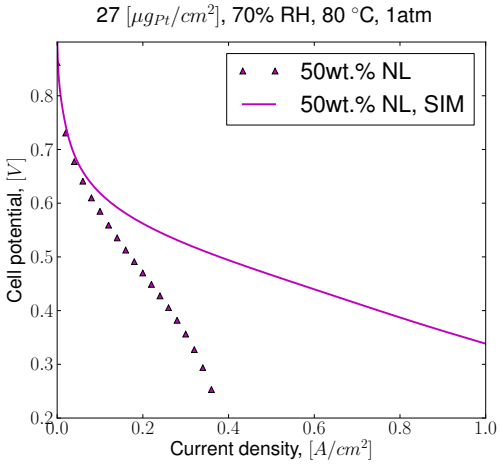

(f) 50 wt.% NL

Figure 4.31 – Quantitative comparisons of simulation and experimental results for 10-50 wt.% NL, with 20 to 50 wt.% NL showing good kinetic region prediction.

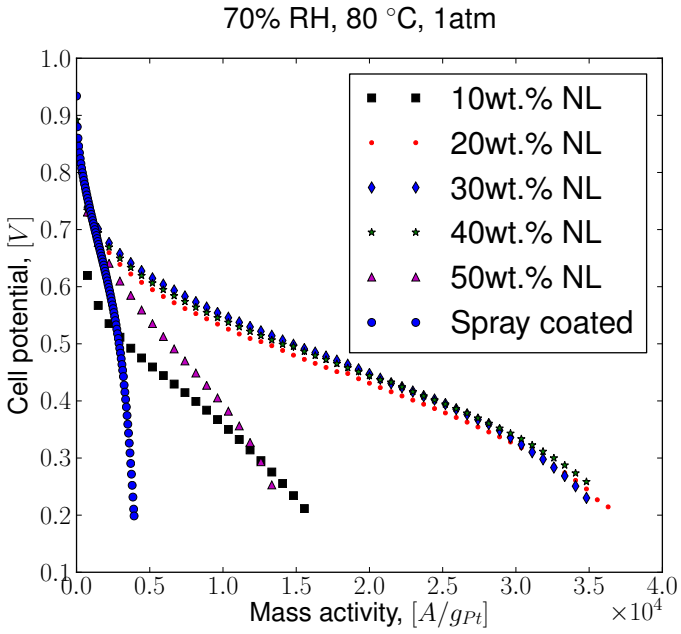

Figure 4.32 – Experimental mass activity of NL study, showing comparison for various ionomer contents 10 - 50 wt.% of IJP CLs (27 $\mu g_{Pt}/cm^2$) against conventional spray coated CL (400 $\mu g_{Pt}/cm^2$).

shows the conventional spray coated CL (400 $\mu g_{Pt}/cm^2$) against the low Pt content CLs. Therefore, neither increasing Pt content or ionomer loading have shown to increase mass activity in the kinetic region. In an effort to further study low Pt content electrodes, oxygen partial pressure and functionally graded CLs will be studied to see if increases in mass activity can be achieved.

4.4 Oxygen Partial Pressure Study

Oxygen partial pressure can have significant effects on fuel cell performance [122], changing open cell voltage, reaction kinetics, and mass transport losses. The aim of this partial pressure study is to investigate the effects of oxygen partial pressure on performance of thin low Pt content electrodes. This change in performance is then examined with the mathematical model to see if the variation in partial pressure can be predicted accurately. Such studies have not previously been performed in the literature.

4.4.1 Experimental Results

Figure 4.33 shows experimentally observed fuel cell performance for a PEFC operating at 80 °C and 70% RH, with variable oxygen concentration achieved by either using a dilute N_2-O_2 mixture or changing total pressure. Note that changing back pressure has an influence also on mass transport process as the product of pressure and molecular diffusivity is constant. In this study six different O_2 partial pressures are studied corresponding to O_2 partial pressures of:

1. 1% $O_{2_{dry}}$ at atm
2. 10% $O_{2_{dry}}$ at atm
3. 21% $O_{2_{dry}}$ (air) at atm
4. 52.5% $O_{2_{dry}}$ (air) at 1.5 bar_{gauge},
5. 100% $O_{2_{dry}}$ at atm
6. 201% $O_{2_{dry}}$ at 2 bar_{gauge}

The experimental results show high sensitivity to oxygen partial pressure, especially for the low Pt content electrode, as seen in Figure 4.33. When comparing the conventional and low Pt content electrode performance with respect to the change in performance from air to air at 1.5 bar_{gauge}. The low Pt content electrode at a cell voltage of 0.6 V and 0.5 V shows an increase in performance of 125% and 137%. In contrast, the conventional CL increased current density by 32% and 14% at the same cell voltages. This large increase in performance shows that low Pt content electrodes operate better at higher back pressure, as the performance increase is far greater relative to the conventional CLs.

Interestingly, both the polarization curves of low Pt loading and conventional CL at increased back pressures of 1.5 bar_{gauge} (52.5% $O_{2_{dry}}$) show kinetic performance outperforming the O_2 partial pressure (100% $O_{2_{dry}}$). This is counter intuitive as the current density and OCV are increased with increasing O_2 partial pressure, as seen in Equation (3.25) and (3.27). This phenomenon has been investigated in the work of Zhang et al. [123], where an increase in ECSA is observed with increasing back pressure. This increase in ECSA explains the back pressure case performing slightly better in the kinetic region as performance is strongly effected by ECSA.

In terms of low O_2 partial pressure, the performance and limiting current are significantly affected. Large decreases in the kinetic region and limiting current are observed with decreasing O_2 partial pressure, as seen in Figure 4.33 (a).

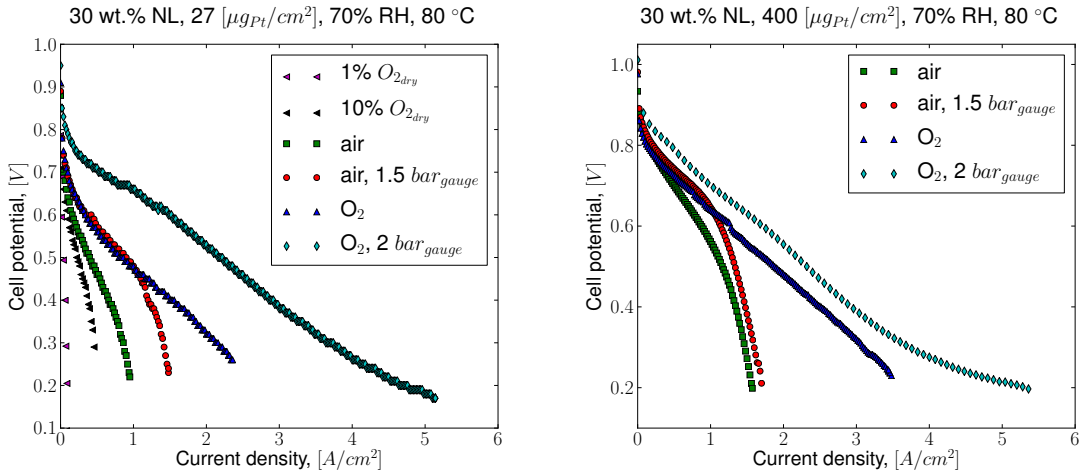

(a) (b)

Figure 4.33 – Comparisons of experimental O_2 partial pressure study for low Pt loading (27 $\mu g_{Pt}/cm^2$) and conventional spray coated (400 $\mu g_{Pt}/cm^2$) CL.

4.4.2 Modelling Results

The low Pt loading CCL mathematical model has been simulated for 1% $O_{2_{dry}}$, 10% $O_{2_{dry}}$, 21% $O_{2_{dry}}$ (air), and the effect of 1.5 bar_{gauge} total pressure. Pure oxygen cases have been omitted from the mathematical model study, as the model assumption of O_2 being infinity dilute in nitrogen is not valid.

Figure 4.34 shows the simulated performance and the large decreases in the kinetic region and limiting current for decreasing oxygen partial pressures. The model also shows an earlier onset of supersaturation of the gas with increased back pressure. To gain a better understanding of the phenomenon occurring in the low Pt loading CCL contour plots for 1% $O_{2_{dry}}$, 10% $O_{2_{dry}}$, 21% $O_{2_{dry}}$ (air), and air (52.5% $O_{2_{dry}}$) at 1.5 bar_{gauge} are investigated. Observing the range of partial pressure change will allow further understanding of the phenomenon occurring inside the CL. To investigated this the current density are shown in Figure 4.35. The 1% $O_{2_{dry}}$ case even at current densities of 0.1 A/cm^2, already shows low current production in the bottom half of the CCL as seen in Figure 4.35 (a).

Oxygen concentration contour plots are shown in Figure 4.36. For the 1% $O_{2_{dry}}$ case, the cell reaches a limiting current of 0.15 A/cm^2 as seen in Figure 4.34. At the limiting current density, Figure 4.35 (e) shows that current production has migrated to the CCL-GDL interface where the channel is located and oxygen molar fraction is

greatest, similar to the 50 wt.% NL CL case in Section 4.3.1. Figure 4.36 shows the oxygen concentration for the 1% $O_{2_{dry}}$ case is highest closest to the channel while the rest of the CCL cross section is significantly oxygen depleted.

Observing the current density contour plots in Figure 4.35 it can be seen that as the oxygen percentage increases in the supply gas (from left to right), the uniformity of the current production across the thin, low Pt content electrode increases. Figure 4.35 (l), showing the greatest uniformity of all cases.

Figure 4.34 shows super-saturation of the vapour by representing the performance lines as fine dashed lines. The relative humidity of the cathode gas inside the CCL reaches 100% significantly earlier when back pressure is applied. Figure 4.37 shows the contour plots of the CCL cross section at 1.0 A/cm^2. Here it can be seen that the super-saturation is occurring at the lower section of the CCL. The increased saturation has been caused by the decreased diffusion rate with increasing pressure. Equation (4.1) describes the change in diffusion with respect to molar mass of the binary gas, temperature, and pressure. The diffusion coefficient D describing diffusion in terms of centimetre squared per second (cm^2/s), is described as:

$$D = \frac{1.858 \times 10^{-3} T^{3/2} \sqrt{\frac{1}{M_1} + \frac{1}{M_2}}}{P \sigma_{12}^2 \Omega} \tag{4.1}$$

where, T is the absolute temperature in Kelvin, M_i is the molar mass g/mol of the two molecules in the gaseous mixture indicated by i, P is the pressure in atm, $\sigma_{12} = \frac{1}{2}(\sigma_1 + \sigma_2)$ is the average collision diameter, and Ω is a dimensionless temperature dependent collision integral.

Using this equation it is possible to see that if the pressure is doubled the diffusion coefficient will decrease by a factor of two. Therefore, water vapour produced in the CCL will have a slower rate diffusing out into the gas diffusion layers causing a local increase in humidification. This phenomenon has been observed experimentally by Zhang et al. [124] [123], where the increase in RH causes a reduction in membrane resistance due to the increased water content in the CL.

In the experimental section it was observed that the low Pt content electrodes had a far greater increase in performance when increasing the back pressure even

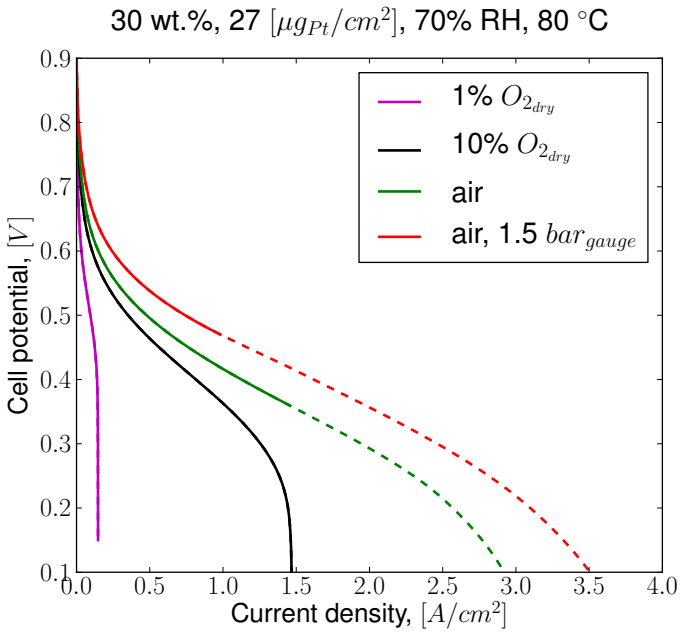

Figure 4.34 – Simulated comparison of O_2 partial pressure study for low Pt content electrode (27 $\mu g_{Pt}/cm^2$) CL. Dashed line indicating regions with over 100% RH.

if the partial pressure of oxygen did not increase as much. Figure 4.38 (a) and (b) shows the low Pt content electrode and (c) (d) represent the conventional CL , for both air and air at 1.5 bar_{gauge}. It is apparent in the low Pt loading case that with increasing partial pressure the CCL utilization increases and the reactions becomes more homogeneous across the layer. In the conventional CL although an increase in reaction is observed only one third of the CCL remains highly active and as a result Pt sites in the lower activity regions are poorly utilized. This poor utilization of two thirds of the CCL possibly explains the difference in performance increase between cells.

Oxygen molar fraction (x_{O_2}) plots across the CCL in Figure 4.39 shows that both the low Pt loading and conventional CL have the same mole fractions. This shows that even though the conventional layer is five times thicker, at 1.0 A/cm^2 oxygen starvation is not an issue. Therefore, the reduced increase in performance is a result of another phenomenon.

Figure 4.40 shows a large protonic potential loss in the conventional electrode relative to the low Pt content CL. The conventional layer shows a much larger region of

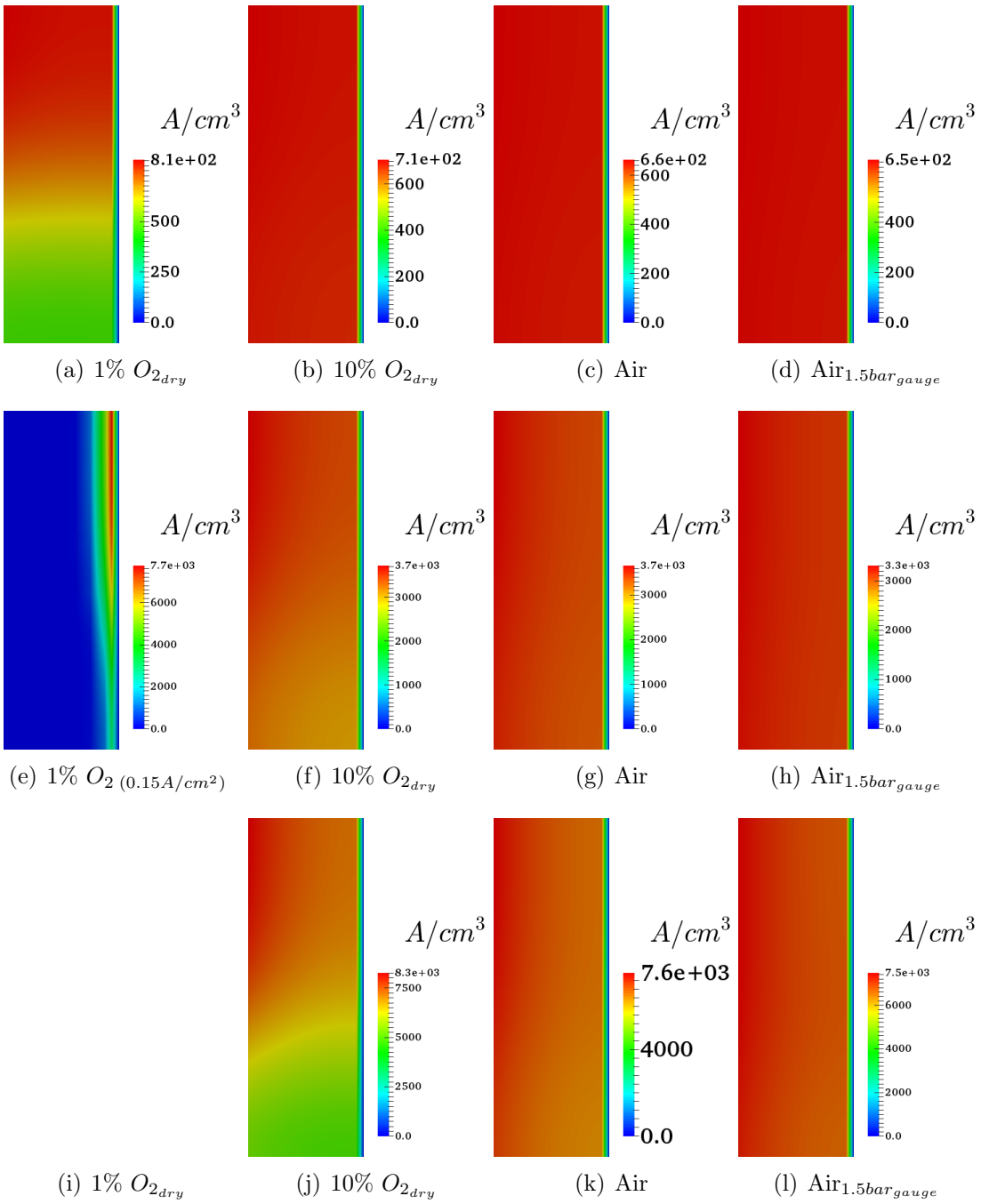

(a) 1% $O_{2_{dry}}$ (b) 10% $O_{2_{dry}}$ (c) Air (d) $\text{Air}_{1.5bar_{gauge}}$

(e) 1% O_2 $_{(0.15A/cm^2)}$ (f) 10% $O_{2_{dry}}$ (g) Air (h) $\text{Air}_{1.5bar_{gauge}}$

(i) 1% $O_{2_{dry}}$ (j) 10% $O_{2_{dry}}$ (k) Air (l) $\text{Air}_{1.5bar_{gauge}}$

Figure 4.35 – Current density contour plots for O_2 study, at varying current densities. (a)-(d) at 0.1 A/cm^2, (e) at 0.15 A/cm^2, (f)-(h) at 0.5 A/cm^2, (i)-(l) at 1.0 A/cm^2. The zero current density along the right edge is a post process artifact caused by zero current in the MPL.

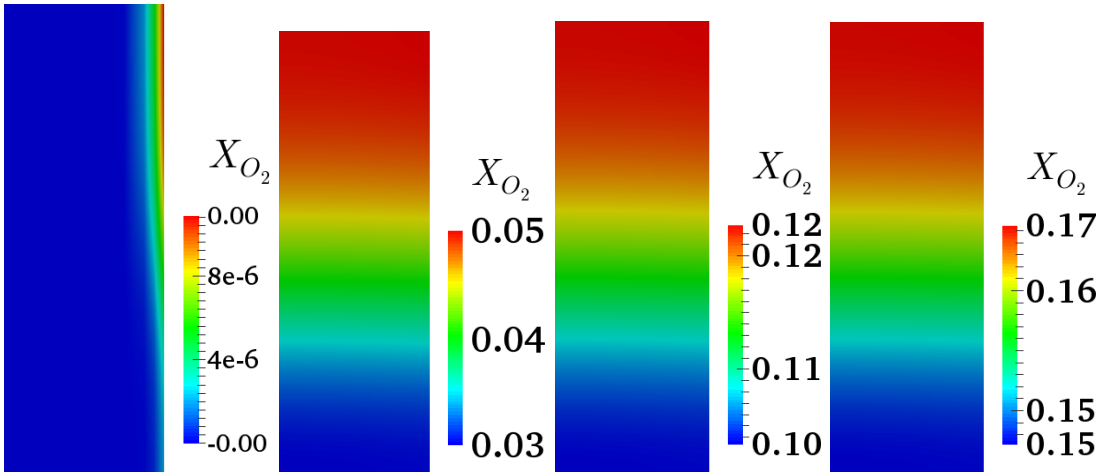

(a) 1% $O_{2\ (0.15 A/cm^2)}$ (b) 10% $O_{2_{dry}}$ (c) Air (d) $\text{Air}_{1.5bar_{gauge}}$

Figure 4.36 – Oxygen mole fraction contour plots for O_2 study, at 0.5 A/cm^2. Showing oxygen limitation of the 1% oxygen case at 0.15 A/cm^2, and initial reactant depletion for the 10% $O_{2_{dry}}$ case.

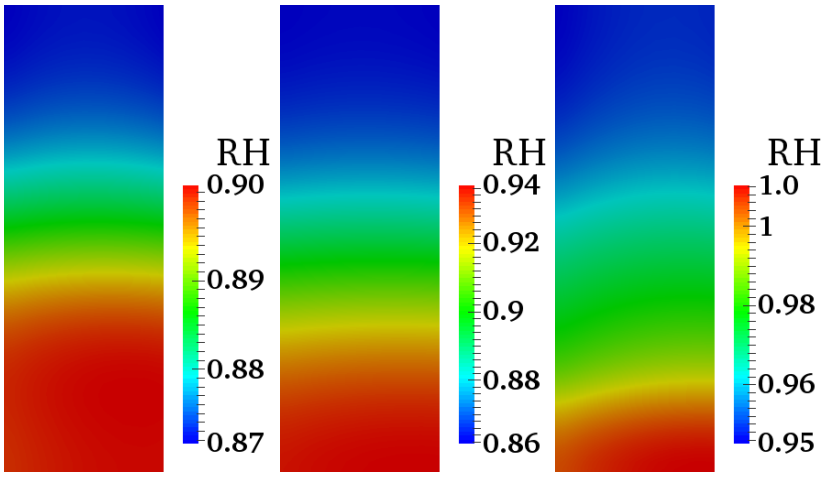

(a) 1% $O_{2_{dry}}$ (b) 10% $O_{2_{dry}}$ (c) Air (d) $\text{Air}_{1.5bar_{gauge}}$

Figure 4.37 – RH contour plots for O_2 study at 1.0 A/cm^2. Showing earlier super-saturation of the CCL with 1.5 bar_{gauge}.

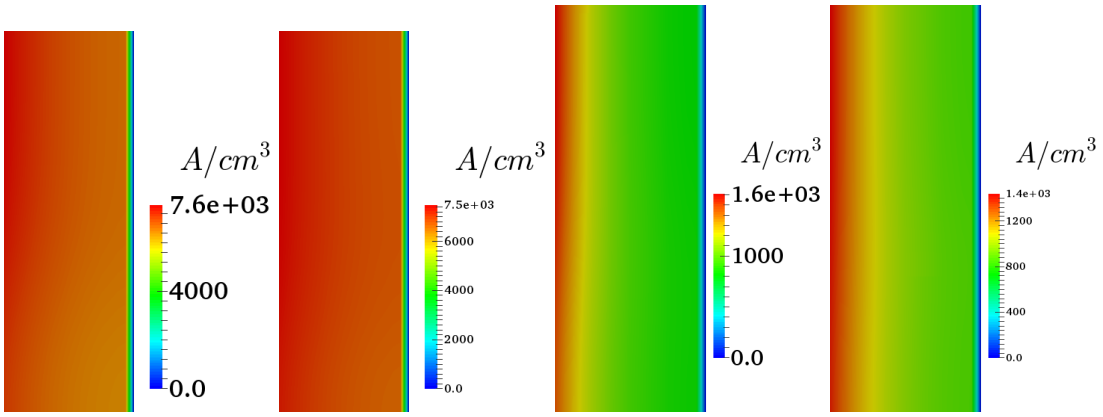

(a) Air (b) $\text{Air}_{1.5bar_{gauge}}$ (c) Air (d) $\text{Air}_{1.5bar_{gauge}}$

Figure 4.38 – Current density contour plots for back pressure study at 1.0 A/cm^2 and 30 wt.% NL. Low Pt loading CL (a) (b), and conventional spray coated CL (c) (d). The zero current density along the right edge is a post process artifact caused by zero current in the MPL.

high protonic potential losses compared to the low Pt content electrode. In addition, the losses incurred by the conventional layer are almost double those of low Pt content electrode for both air and air at 1.5 bar_{gauge} cases. These relatively large protonic losses in the conventional spray coated CL make it undesirable to generate current on the side furthest from the membrane, represented by the low overpotentials in Figure 4.41. In contrast these relatively high losses are not observed in the low Pt CL case and therefore a much more uniformly reaction rate is observed.

4.4.3 Discussion

Figure 4.42 compares the low Pt content experimental and simulated results showing a good qualitative prediction of the performance decrease with decreasing partial pressure of oxygen. To assess the quantitative agreement Figure 4.43 shows comparisons between the experimental and predicted results at 1% $O_{2_{dry}}$, 10% $O_{2_{dry}}$, air, and air at 1.5 bar_{gauge}. The experimental and simulated 1% $O_{2_{dry}}$, 10% $O_{2_{dry}}$, and air show very good prediction of the experimental performance at low current densities. The air at 1.5 bar_{gauge} shows slight under prediction of the kinetic region, however, maintaining good ohmic prediction having similar slopes. The under predicted kinetics can possibly be explained by the work of Zhang et al. [123] where an increase in ECSA is seen with increasing back pressure. This increase in ECSA will cause the experimental results to show improved kinetics a relationship which is not yet described in the mathematical model. In additional this increase in kinetics

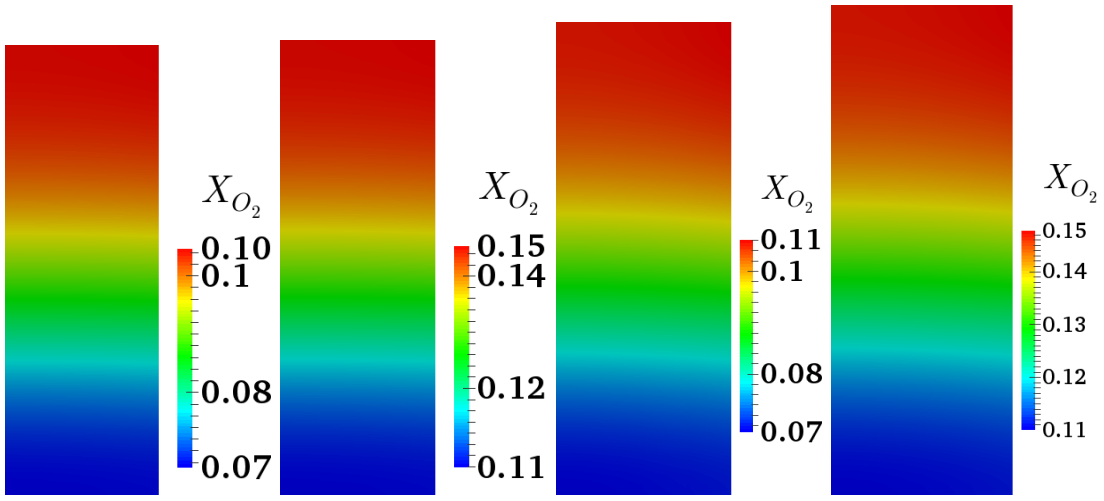

(a) Air (b) $\text{Air}_{1.5bar_{gauge}}$ (c) Air (d) $\text{Air}_{1.5bar_{gauge}}$

Figure 4.39 – Oxygen mole fraction contour plots for back pressure study at 1.0 A/cm^2 and 30 wt.% NL. Low Pt content CL (a) (b) and conventional spray coated CL (c) (d).

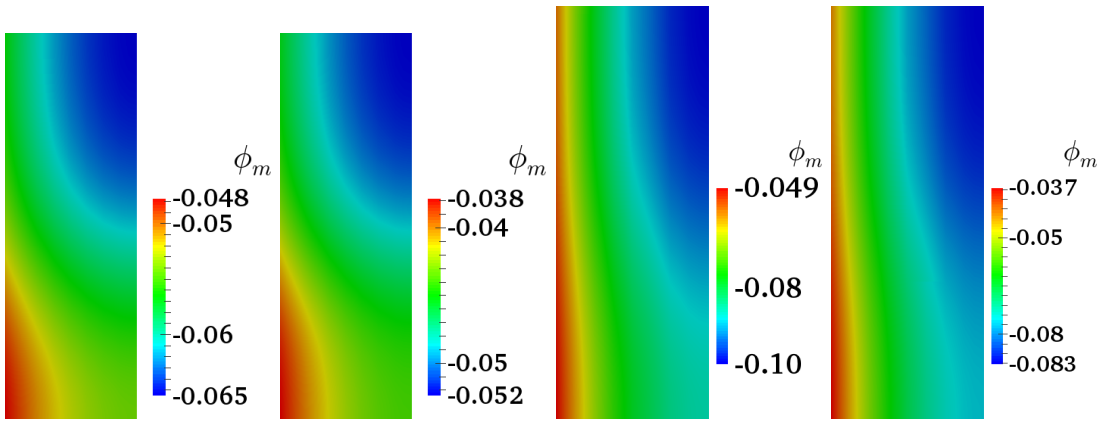

(a) Air (b) $\text{Air}_{1.5bar_{gauge}}$ (c) Air (d) $\text{Air}_{1.5bar_{gauge}}$

Figure 4.40 – Protonic potential contour plots for back pressure study at 1.0 A/cm^2 and 30 wt.% NL. Low Pt content CL (a) (b), and conventional CL (c) (d).

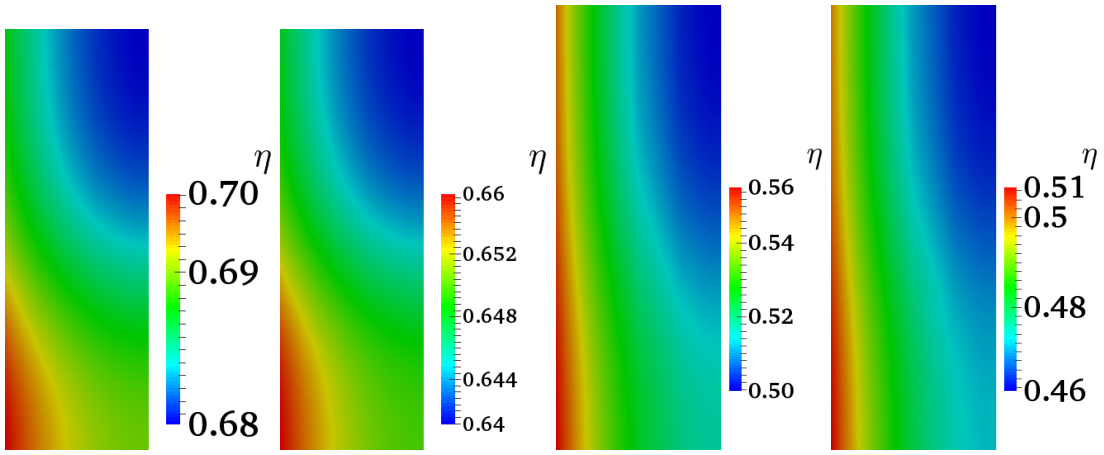

(a) Air (b) $Air_{1.5bar_{gauge}}$ (c) Air (d) $Air_{1.5bar_{gauge}}$

Figure 4.41 – Overpotential contour plots for back pressure study at 1.0 A/cm^2 and 30 wt.% NL. Low Pt content CL (a) (b), and conventional CL (c) (d).

may also be aided by the serpentine flow channel effects as described in Section 4.2.3.

4.4.3.1 Conventional loading electrode comparisons

The overall trends and predicted voltage improvement of the conventional spray coated CL show good characterization, as seen in Figure 4.44 (a). However due to the serpentine flow channel effects as explained earlier in Section 4.2.3, the model prediction are slightly under the experimental results. Figure 4.44 (b) shows the experimental results using the parallel flow channel arrangement, where good production is observed at ambient pressure and slight under-predictions at 2 bar_{gauge} pressure [114]. The slight under-prediction with increased back pressure can possibly be contributed to the observed increase in ECSA with pressure [123] which is not yet accounted for in the model.

4.4.3.2 Mass Activity of Conventional and Low Pt loading Electrode Comparison

The mass activity plots in Figure 4.45, show when back pressure (or O_2 partial pressure) is increased that the low Pt content electrodes have a relatively large increase in mass activity compared to that seen in conventionally Pt content electrodes. This large increase in mass activity compared to the conventional CL makes low Pt content electrodes very appealing in terms of industrial applications, as at relatively small increases in back pressure large increases in performance can be observed.

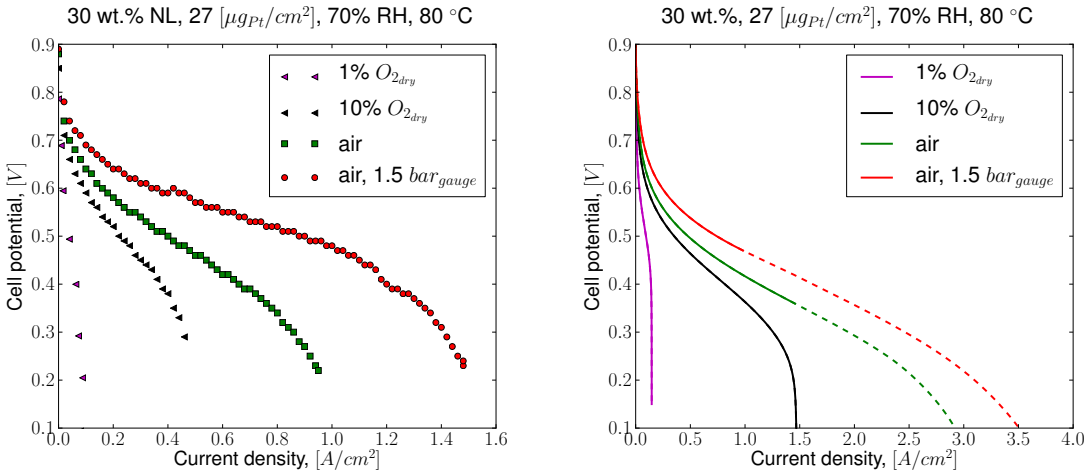

(a) Experimental Trends

(b) Simulated Trends

Figure 4.42 – Qualitative comparisons of experimental (a) and simulation (b) results for O_2 partial pressure and back pressure, 27 $\mu g_{Pt}/cm^2$.

In previous sections when varying ionomer or Pt content no increase in active area was achieved, especially in the desired >0.6 V range, where typical industrial application operate for high cell efficiency. However, increasing back pressure has shown to increase mass activity, not only in the mass transport region but also in this desired high voltage region. This attribute should be investigated in future work to see if there is an optimum operating range, as using moderate back pressure with low Pt content electrodes could produce performances equivalent to much larger Pt content electrodes.

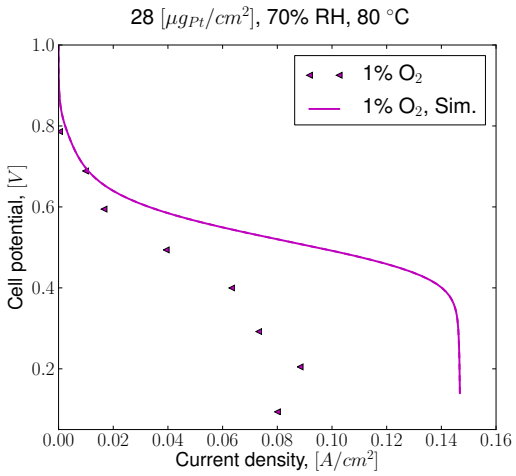

(a) 1% $O_{2_{dry}}$

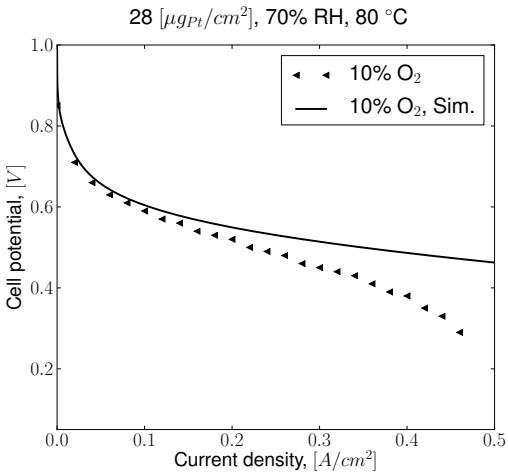

(b) 10% $O_{2_{dry}}$

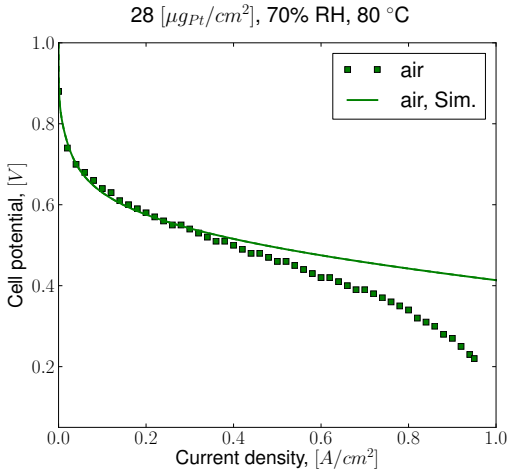

(c) Air

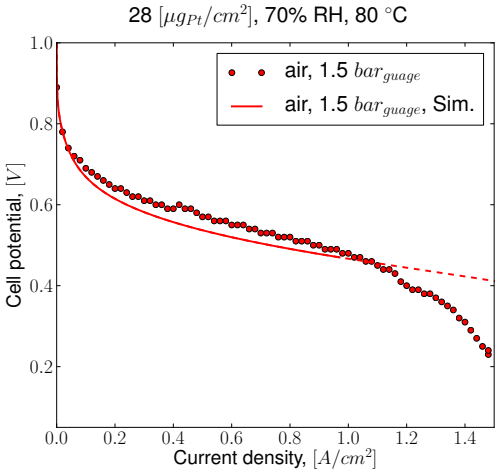

(d) Air at 1.5 bar_{gauge}

Figure 4.43 – Quantitative comparisons of simulation and experimental results for O_2 partial pressure and back pressure. Showing good prediction of the kinetic region in all cases.

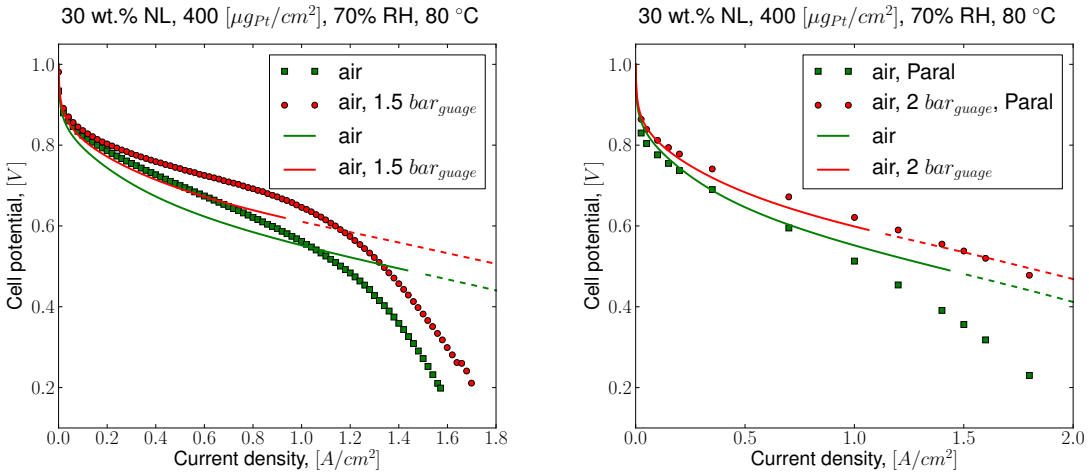

(a) Serpentine (b) Parallel (Experimental data [114])

Figure 4.44 – Qualitative and quantitative comparisons of experimental O_2 partial pressure study for conventional (400 $\mu g_{Pt}/cm^2$) electrode and also the discrepancy between serpentine and parallel flow fields.

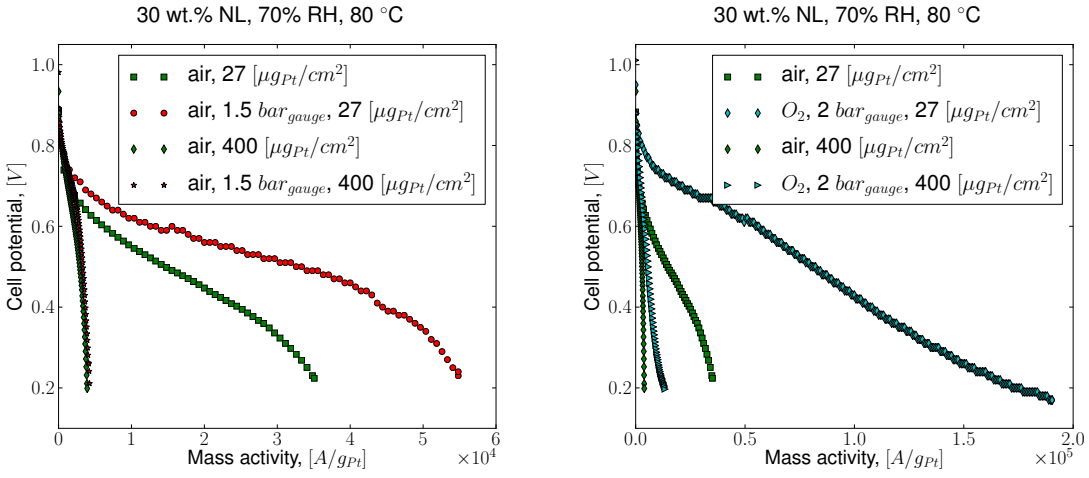

(a) (b)

Figure 4.45 – Comparisons of mass activity results for back pressures and O_2 partial pressure for both thin low Pt loading and conventional spray coated CL.

4.5 Functionally Graded Nafion® CL Study

In previous sections, ionomer [1] and Pt loadings (this work) were investigated to see if it is possible to increase mass activity or performance for the same Pt content. Findings showed that ionomer had little to no affect, and that Pt content increased performance at the expense of mass activity values.

In order to see if performance can be increased for equivalent NL and Pt content, functionally graded NL electrodes are fabricated, characterized, and compared to a homogeneous CCL. The CLs have been fabricated using the methods described in Section 2.3. In the work by Shukla et al. [1] no noticeable change in performance was observed for NL between 20 - 40 wt.%. Therefore, in this work the functionally graded CCLs have been fabricated using 20 - 40 wt.% NL in either the inner or outer layers (Figure 2.12) in order to provide greatest layer contrast without incurring large charge transport losses as seen in the 10 wt.% NL case or mass transport issues as seen in the 50 wt.% NL case.

The functionally graded CCLs were fabricated with an intermediate drying process to ensure a sharp change in layer type, providing closest representation of the functionally graded model. To investigate whether this intermediate drying has an effect on the cell performance, a study of intermediate drying process is also conducted in this section.

Before fabrication of the functionally graded CCLs the mathematical model was run for both homogeneous NL electrodes of 20, 30, and 40 wt.% and functionally graded ionomer electrodes. The homogeneous CLs are simulated to see if increasing from 1.55 μm to 3.1 μm thickness will have increased sensitivity to NL, and aid in observing the possible phenomenon that occur in 3.1 μm thick functionally graded CLs.

4.5.1 Modelling Results

Figure 4.46 shows the simulated results for both homogeneous and functionally graded CLs, using the simulation parameters seen in Section 3.3. The simulated data shows the homogeneous 20 wt.% NL electrode (ML|20|20) having the poorest results, while the 40 wt.% NL electrode (ML|40|40) showed the best kinetic and ohmic performance. Therefore, the mathematical model demonstrates that for CLs with 3.1 μm thickness NL begins to play an important roll in electrode performance.

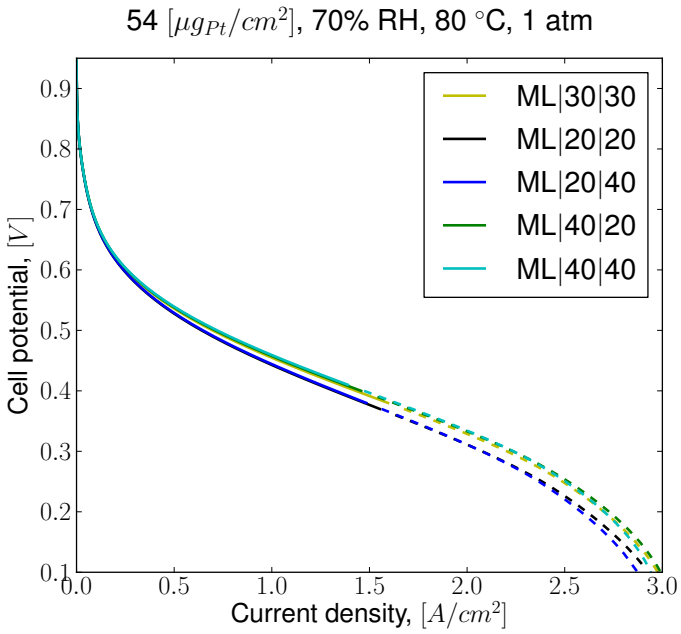

Figure 4.46 – Simulated homogeneous and functionally graded NL study. Homogeneous 40 wt.% NL CL showing best kinetic and ohmic regions, with similar performance for the functionally graded ML|40|20 electrode showing best mass transport performance. 20 wt.% NL electrodes for both homogeneous and functionally graded (ML|20|20 and ML|20|40) showing worst performances

The functionally graded ionomer CL with the 20 wt.% NL on the inner layer (ML|20|40) shows the second worst performance in the kinetic and ohmic region while also having lowest mass transport performance out of all of the cells. The homogeneous base case (ML|30|30) shows average results, while the functionally graded ionomer CL with 40 wt.% NL on the inner layer (ML|40|20) shows performances similar to the homogeneous 40 wt.% NL electrode with the best overall performance in the mass transport region.

To gain a better understanding into the phenomenon occurring inside the functionally graded and homogeneous CLs several contour plots are investigated, as seen in Figure 4.47. The contours show the base case ML|30|30, ML|40|40 and the functionally graded ML|40|20 and ML|20|40 CCLs. The ML|40|20 CL showing the best distribution of current across the CL. Conversely, in the ML|20|20 and ML|20|40 CCLs very poor utilization of the entire CCL area is seen. To understand the reasons for this variation in performance, both the oxygen mole fraction (x_{O_2}) and protonic

potential (ϕ_m) contour plots are investigated.

Observing the x_{O_2} plots in Figure 4.48, show that all molar fractions are very similar with ML|40|40 and ML|20|40 beginning to see onset of reactant depletion, due to the high ionomer content reducing CL porosity. This is not seen in the functionally graded ionomer CL ML|40|20, as the outer layer contain only 20 wt.% ionomer allowing good diffusion characteristics across the first half of the CCL with adequate NL on the inner layer allowing good charge transport characteristics.

As none of the CCLs have x_{O_2} limitations the poor cell performance for ML|20|20 and ML|20|40 can be explained examining the ϕ_m contour plots. In Figure 4.49 it is possible to see that the ML|20|20 and ML|20|40 have the greatest ϕ_m losses causing the current to migrate to the ML-CCL interface, and low overpotentials making current production difficult, as seen in Figure 4.50. While the ML|30|30, ML|40|40 and ML|40|20 have the lowest ϕ_m losses. Interestingly even thought the ML|40|20 electrode contains 20 wt.% ionomer on the outer layer its ϕ_m equivalent if not less than the homogeneous ML|40|40 CL.

Comparing the current density plots it is possible to see that the homogeneous ML|40|40 is not getting full utilization of the outer layer compared to the inner half. Therefore, the functionally graded CL ML|40|20 with only 20 wt.% NL on the outer layer does not experience great protonic loss as a lower portion of outer layer is being utilized for current production.

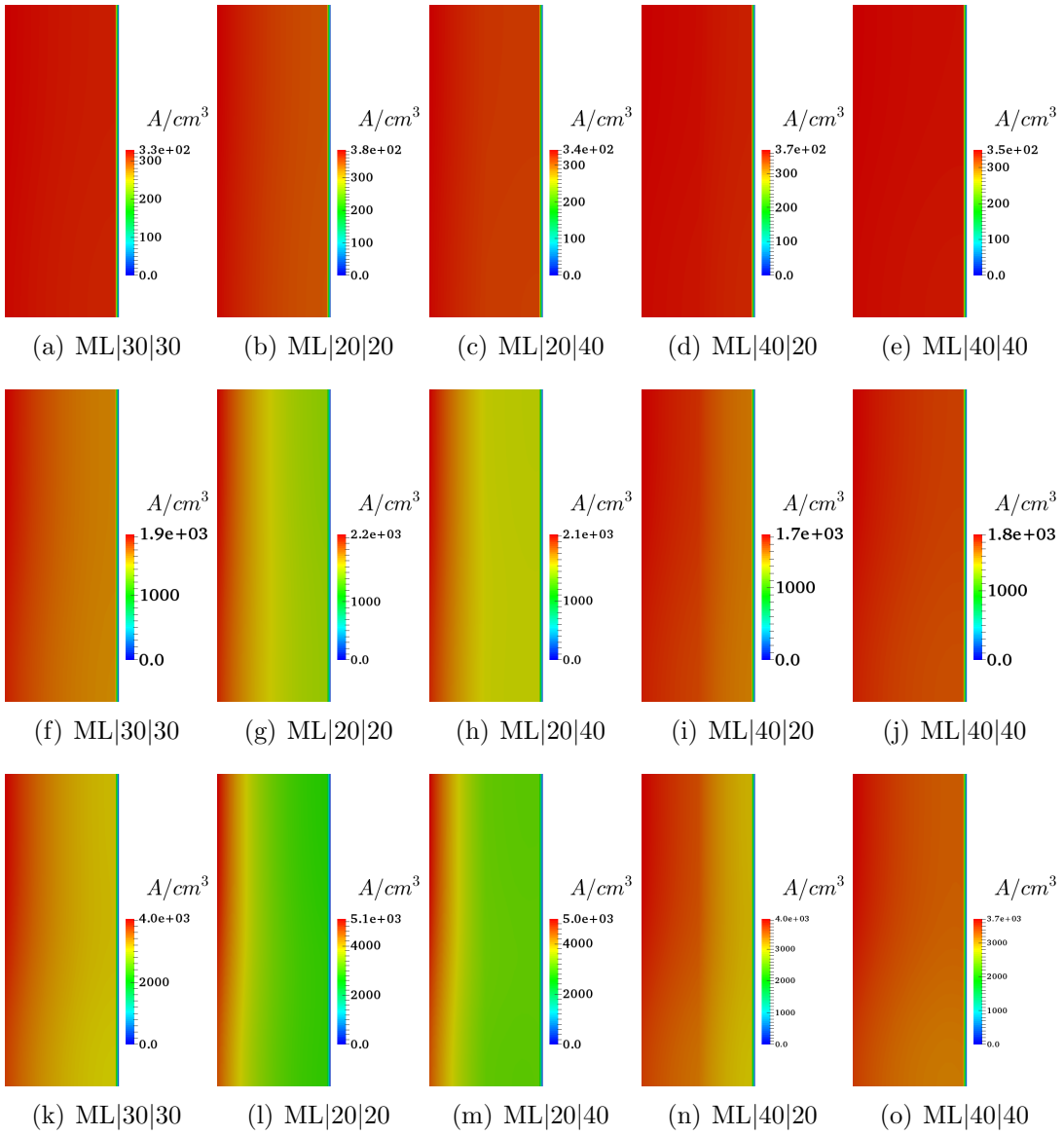

(a) ML|30|30 (b) ML|20|20 (c) ML|20|40 (d) ML|40|20 (e) ML|40|40

(f) ML|30|30 (g) ML|20|20 (h) ML|20|40 (i) ML|40|20 (j) ML|40|40

(k) ML|30|30 (l) ML|20|20 (m) ML|20|40 (n) ML|40|20 (o) ML|40|40

Figure 4.47 – Current density contour plots for homogeneous and functionally graded NL study at varying current densities. (a)-(d) at 0.1 A/cm^2, (e)-(h) at 0.5 A/cm^2, (i)-(l) at 1.0 A/cm^2. Showing the most homogeneous distribution of current production in the ML|30|30, ML|40|40 and the functionally graded ML|40|20 CCLs. With poor distribution seen in the ML|20|20 and the functionally graded ML|20|40 CCLs. The zero current density along the right edge is a post process artifact caused by zero current in the MPL.

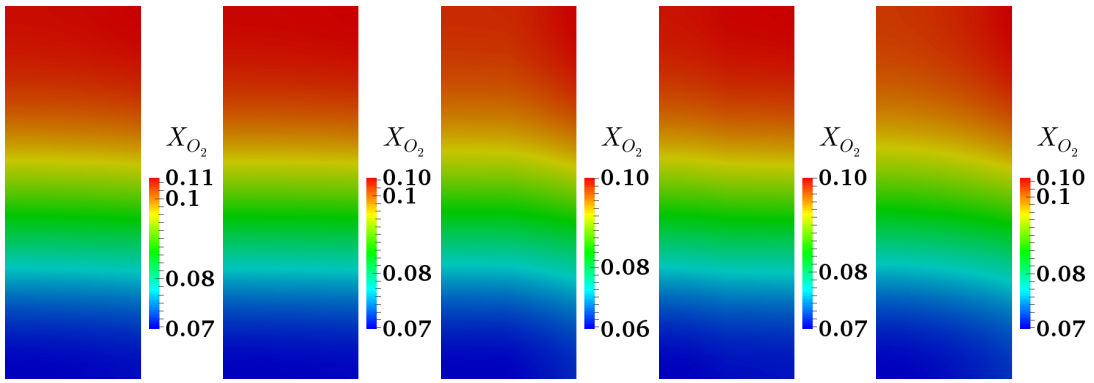

(a) ML|30|30 (b) ML|20|20 (c) ML|20|40 (d) ML|40|20 (e) ML|40|40

Figure 4.48 – Oxygen mole fraction contour plots for homogeneous and functionally graded NL study at 1.0 A/cm^2. The ML|40|40 and ML|20|40 CCLs showing initial onsets of reactant depletion.

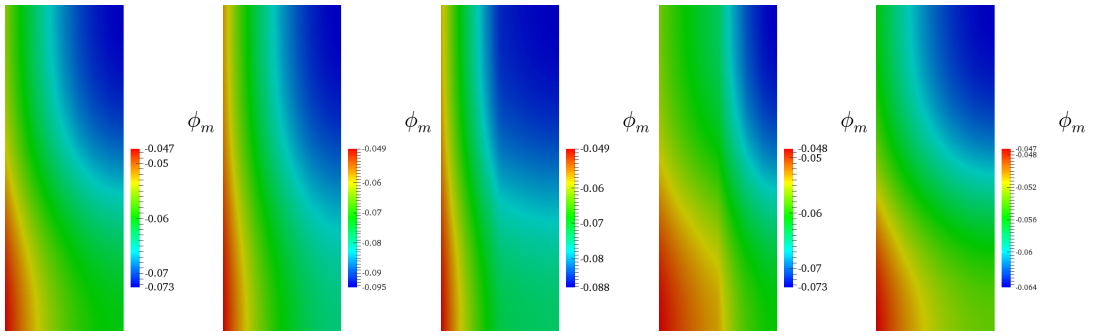

(a) ML|30|30 (b) ML|20|20 (c) ML|20|40 (d) ML|40|20 (e) ML|40|40

Figure 4.49 – Protonic potential contour plots for homogeneous and functionally graded NL study at 1.0 A/cm^2. Showing large protonic losses in the ML|20|20 and ML|20|40 CCLs.

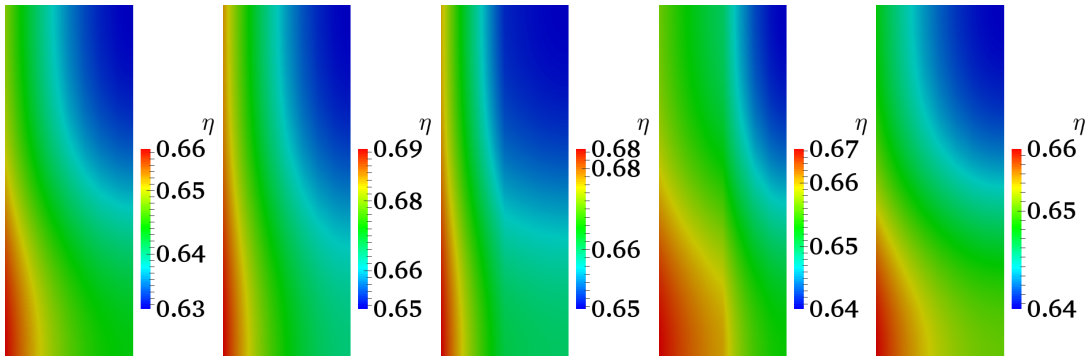

(a) ML|30|30 (b) ML|20|20 (c) ML|20|40 (d) ML|40|20 (e) ML|40|40

Figure 4.50 – Overpotential contour plots for homogeneous and functionally graded NL study at 1.0 A/cm^2. Showing areas of low overpotentials in ML|20|20 and ML|20|40 CCLs reducing current production across the electrode.

4.5.2 Experimental Results

Figure 4.51 shows the results for a homogeneous ionomer content electrode containing 30 wt.% NL. and two functionally graded ionomer CLs, as seen in Figure 2.12. It is observed that the functionally graded layers show superior performance in the kinetic region, for both ML|40|20 and ML|20|40 when compared to the base homogeneous case.

Towards the mass transport region of the curve a small deviation between graded electrodes are seen, where the ML|20|40 appears to incur greater losses. This loss is thought to arise due to the decreased porosity in the outer layer, as well as the low ionomer content close to the ML leading to larger protonic resistance where the protonic flux is greatest. In contrast, the ML|40|20 due to the low NL on the outer layer should have adequate reactant diffusion where the diffusion flux is greatest and higher percentages of ionomer near the membrane where protonic flux is greatest.

4.5.3 Intermediate Drying

To investigate whether drying has any effect on electrodes other than slightly increasing the thickness, as seen in Section 4.1, an additional comparison is carrying out comparing a 10 pass CL with 30 wt.% NL with no intermediate drying and a 10 pass CL with overnight drying after the first 5 layers, as done with the functionally graded electrodes.

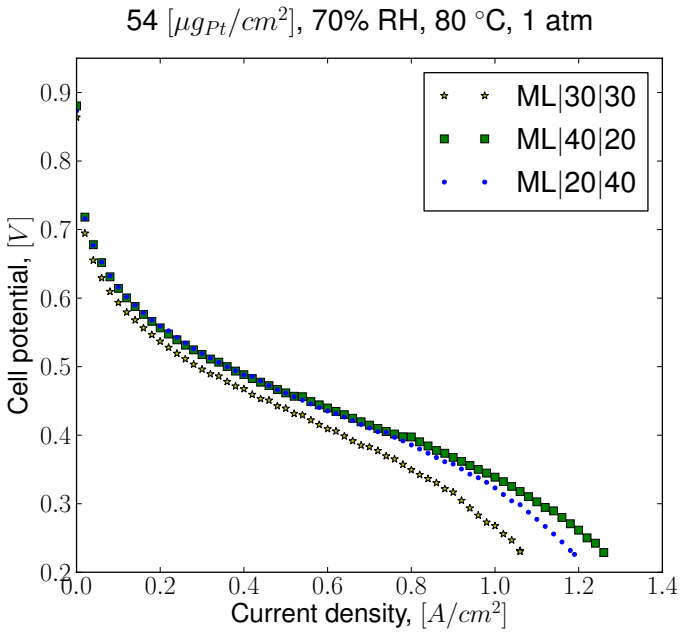

Figure 4.51 – Comparisons of functionally graded NL Study and equivalent NL homogeneous CL. Showing increased kinetic, ohmic, and mass transport regions.

A comparison of the two homogenous electrode performance can be seen in Figure 4.52. The figure shows that the maximum performance for both cells remained the same, however, the CL which had undergone an intermediate drying stage showed more sensitivity to RH. To understand the change in performance the cell resistance is plotted against the current, in Figure 4.52 (b). Comparing both cells it is possible to see that the electrode that was fabricated with a drying process has a greater cell resistance at lower RH. This difference in resistance is then reduced with increased RH values.

The resistance plot shows a large reduction in resistance with increasing RH. It is also observed that at low RH the resistance reduces with increasing current. This reduction is less prominent at higher humidification, where the water production in the CCL has less hydration effect on the membrane. In the case of the 10 layer electrode the results show that the drying process only decreases the performance of a homogeneous CL at low RH, and that the increased kinetic region (ECSA) for functionally graded CLs observed in Section 4.1.2.5 is likely due to the functionally grading.

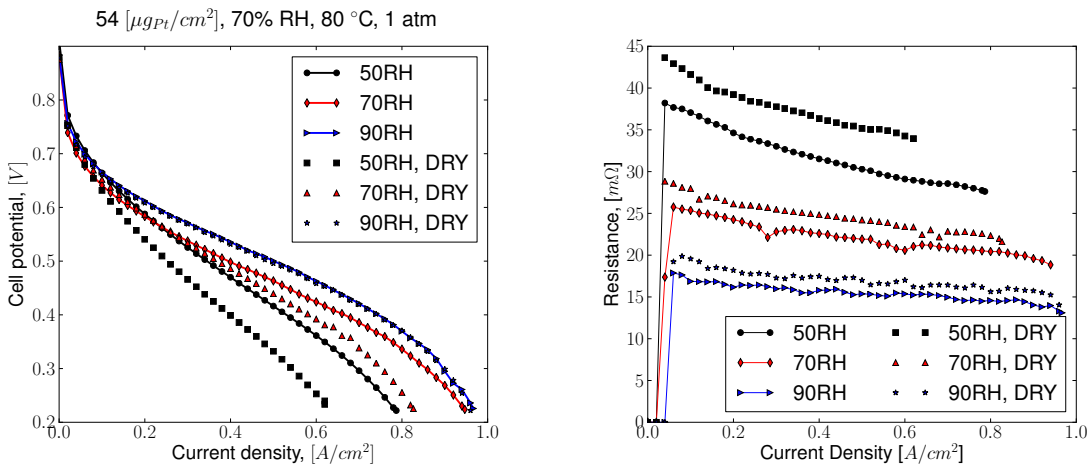

(a) (b)

Figure 4.52 – Comparisons of intermediate drying on homogeneous CCLs. Showing similar maximum performance (a), and increased sensitivity to RH change due to higher protonic resistance (b) at low humidity.

4.5.4 Discussion

The qualitative comparisons of simulation and experimental results for functionally graded NL can be seen in Figure 4.53. The comparisons has been done using the experimentally observed ECSA data as seen in Section 3.11. Comparing the trends it is possible to see good correlation between all CCLs except for the later mass transport region of the ML|20|40 CCL. This large under prediction is due to the large protonic losses across the 20 wt.% section of the CL where much of the active area is not being utilized in the mathematical model.

When comparing the simulated results quantitatively there are large over predictions by the model in the kinetic region. This is a result of using a older batch of Pt which had a lower catalyst performance. This catalyst batch showed similar ECSA as the newer batch, however, its performance was much lower. This lower activity of the Pt can be observed more easily in the mass activity plot in Figure 4.55, where the kinetic region is substantial reduced when compared to the conventional spray coated CL a region that has shown similar results with the newer batch of Pt (Figure 4.23 and 4.32).

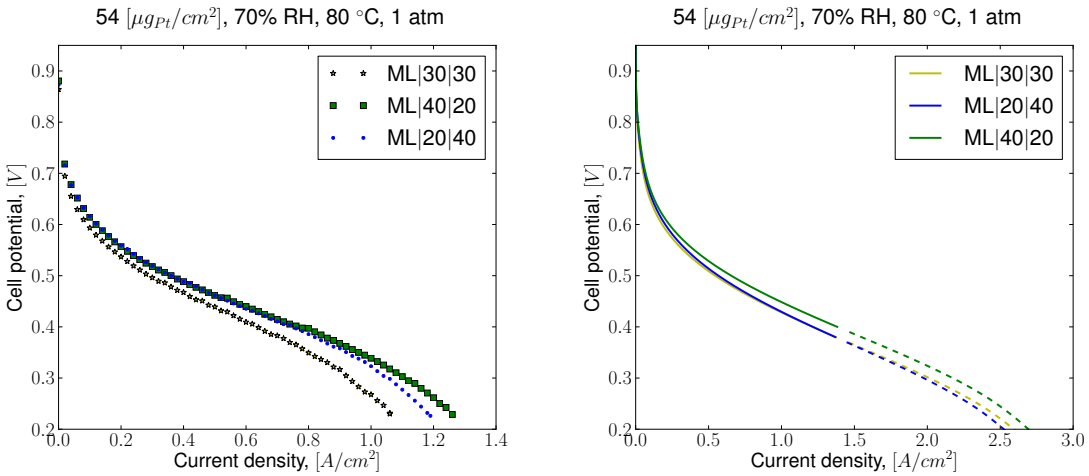

(a) Experimental Trends

(b) Simulated Trends

Figure 4.53 – Qualitative comparisons of simulation and experimental results for functionally graded NL, 54 $\mu g_{Pt}/cm^2$.

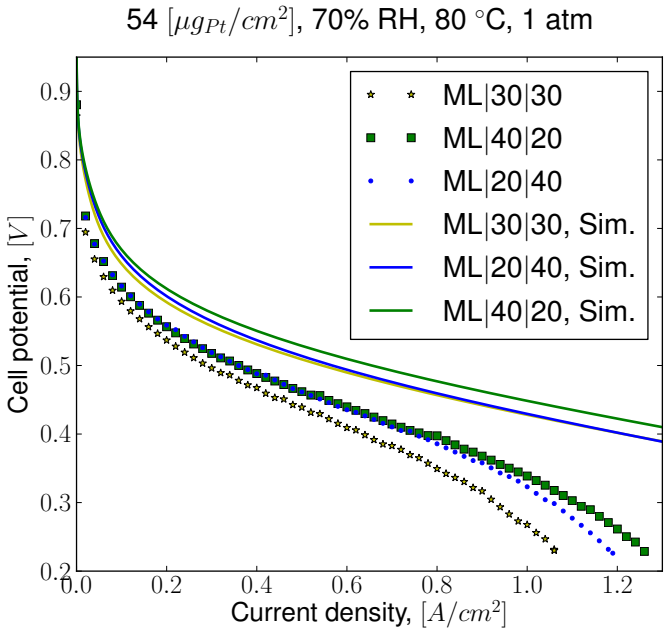

Figure 4.54 – Qualitative and quantitative comparisons of simulation and experimental results for functionally graded NL. Showing good trend prediction with slight over prediction.

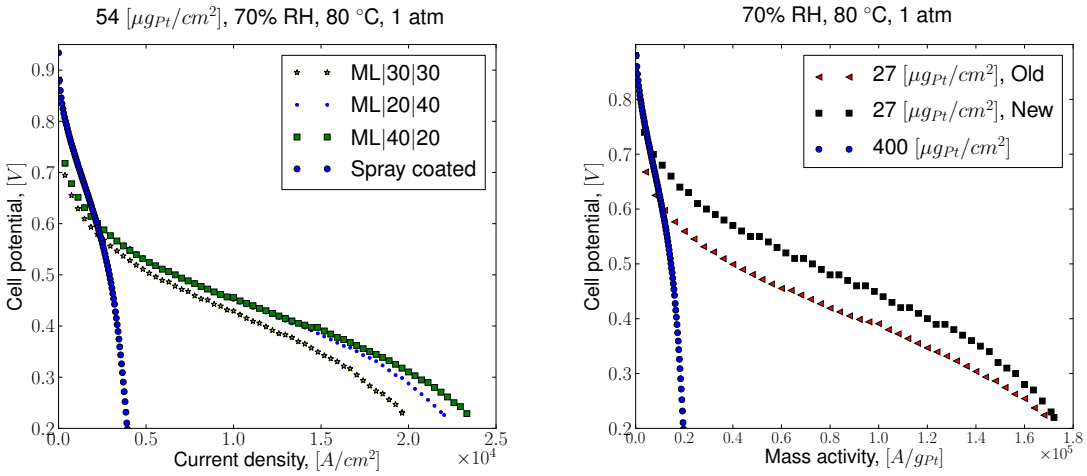

(a) Mass activity

(b) Pt batch comparison

Figure 4.55 – Quantitative comparisons of mass activity for homogeneous 30 wt.% NL CCL and functionally graded CCLs. Showing increased kinetic, ohmic, and mass transport regions of functionally graded CCLs (a). Mass activity comparisons of old Pt batch (used in functionally graded study) and new Pt batch used in the other studies (b), showing the old Pt to have a substantially reduced mass activity

Chapter 5

Conclusion and Future Work

5.1 Conclusion

Thin low Pt content electrodes have been investigated and characterized showing the following results:

Electrode thickness was found to have a linear relationship to the number of printer passes when using Glycerol solvent and non-linear relationship when using Ethylene glycol. Increasing solvent content resulted in an increased thickness. In addition, when printing 10 layer electrodes intermediate drying was shown to increase the electrode thickness and standard deviation by 10 and 33%. Overall, the thickness study of the SEM images showed close to uniform thickness with no micro cracks and good homogeneous distribution of material throughout the electrode cross section.

The solvent type and ratio were also found to have effects on the surface coverage characteristics when printing 5 layer electrodes. The Glycerol ink formed striations in the directions of the printing path, leaving areas of the membrane exposed. Ethylene glycol was shown to have better coverage while still showing slight striations. The ink with increased Ethylene glycol content was shown to have the most uniform coverage of the membrane. At 10 printer passes or greater, uniform coverage and thickness was found for both Ethylene glycol and Glycerol ink types.

Electrode Pt loadings were characterized using X-ray fluorescence at AFCC, showing linear trends between the number of printer passes for all ink types, between 5 and 10 printer passes, with Ethylene glycol ink showing most consistent results.

The fabrication process for PEFC using the inkjet methods showed pristine cells to

have an average crossover of 0.9 mA/cm^2 using NR211 ionomer membrane (25 μm). This value was observed to stay constant irrespective of the number of printed cathode catalyst layers. PEFCs with hydrogen crossover above a 1.0 mA/cm^2 (2.0×10^{-8} $mole\cdot s^{-1}\cdot cm^{-2}$) threshold were omitted from this thesis.

PEFC assembly losses consist of protonic, electronic and contact resistances. In this work a current interrupt technique is used to acquire the total internal resistance and an Ohmic method is used to find the portion associated with electronic resistance. Using these two techniques allowed the charge transport resistances to be observed separately. The electronic resistance was found to be ≈ 1.9 $m\Omega/cm^2$ at an operating cell temperature of 80 °C and increased with temperature. The results found that at 90 % relative humidity the electronic and contact resistance made up a maximum of 29% of the total internal resistance, showing that the majority of charge transfer losses occur due to protonic resistances.

The effect on electrode electrochemical active area at varying Pt loadings is also studied. The analysis showed that with increasing Pt content for the 20 wt.% Pt|C and 46.7 wt.% Pt|C a decrease in active area is observed. The active area in all electrodes were shown to have a large decrease between 5 and 10 layers, this large decrease reduced between 10 to 20 printer passes. In addition, a significant effect is observed when using different solvents, where the Ethylene glycol ink was shown to have a 25% increase in active area compared to the Glycerol ink.

The effects of relative humidity on electrochemical active area was also studied in order to investigated whether the thin low Pt content electrodes have similar sensitivity to relative humidity as is seen in conventional electrodes. The study was conducted on two 30 wt.% ionomer loading cells showing no correlation between relative humidity and active area. This contrasts to conventional electrodes where a change in active area is observed.

Functionally graded ionomer electrodes were also investigate. The results found to have a 28% increase in active area compared to a homogeneous electrode containing equivalent Pt and ionomer loadings. Therefore, functionally graded electrodes are shown to increase electrode utilization and should be investigated further.

In order to better understand the characteristics behind inkjet printing electrodes and to also understand the limiting phenomenon with increasing Pt loading, several

electrodes electrodes were fabricated and characterized. The experimental results for the Pt loading study showed a significant increase in the kinetic region with increased Pt loading for both solvent types. With the increase in Pt loading a reduced mass activity is also observed in the mass transport region for all electrodes. This is due to the increased charge and mass transport losses with increased thickness.

The experimental Pt loading data is used to validate a new multi-step kinetics model. The results found that the new double-trap kinetics model is better able to predict the drop in cell performance with reduced Pt content. In contrast the conventional Tafel kinetics model was observed to greatly overstated the low Pt content performances. Once validated the model was utilized to investigate the phenomenon causing a reduction in mass activity. The model predicted that the increased protonic losses across the catalyst layer is the predominant cause for reduced performance and electrode utilization. The results from this investigation emphasize the need low charge transport losses in the electrodes, thereby allowing high utilization of Pt particles across the entire catalyst layer.

Shukla et al. [1] conducted an ionomer study on thin low Pt content electrodes, showing low sensitivity between 20 - 40 wt.% ionomer loadings and large fall offs in performance outside this range where ionomer coverage and mass transport issues arose. In this study, Shukla et al. observed large mass activities compared to the conventional spray coated electrode. The experimental data was used in this work to validate the mathematical models ability to predict the ionomer trends for the kinetic and ohmic regions. The model was found to successfully predict the trends and closely match the performances in the kinetic and initial ohmic regions. The model deviates away from the experimental data towards the second half of the ohmic region over-predicting the cell performance. This over-prediction is thought to result from the increasing significance of the oxygen transport through the gas-ionomer interface, as seen in recent literature [51, 58, 120]. The model showed an increasing utilization of the electrode cross sections with increasing ionomer from 20 - 40 wt.%, a trend also observed experimentally whereby thin low Pt content electrodes show best performance at higher contents of ionomer loading [1, 23].

Low Pt content electrodes were studied for several oxygen partial pressure. The variation in oxygen concentration is achieved by either using a dilute N_2-O_2 mixture or changing total pressure. The results found that oxygen partial pressure has a significant effect on low Pt content electrodes, having large increase in performance in

kinetic, ohmic, and mass transport regions with increased partial pressure and back pressure. A conventional spray coated electrode is also compared against for similar operating conditions showing a lower increase in performance compared to the significance performance increase seen in the thin low Pt content electrode. Both the electrodes showed similar performances when pure oxygen is supplied to the cathode at 2 bar_{gauge}, the conventional cell having marginally higher kinetic region compared to the low Pt content cell and both cells showing similar limiting current density of 5.1 A/cm^2.

The mathematical model was then used to simulated the varying oxygen concentrations for the low oxygen content, air, and air at 1.5 bar_{gauge}. The simulation results were found to accurately predict the kinetic and initial ohmic regions, where the contour plots showed more uniform current production across the low Pt content electrode with increasing oxygen concentrations. This same trend was not seen in the conventional electrode, whereby 66% of the cell showed relatively low activity. This contrasted greatly to the low Pt content electrode which showed high activity across the entire catalyst layer cross section. The limiting phenomenon in the conventional electrode was found to result from the large protonic losses across the electrode. The large increase in protonic loss is a possible explanation to the poor increase in conventional cell performance at increased back pressure. The increased back pressure was also found to decrease the diffusion rates in the catalyst layer, causing the earlier onset of super-saturation of gases inside the cathode catalyst layer.

Functionally graded ionomer low Pt content electrodes were simulated as well as homogeneous electrodes at equivalent thicknesses (3.1 μm), in order to gain further information on the phenomena dictating cell performance. Results found that ionomer had a more significant effect on performance compared to 1.55 μm thick electrodes. Simulations show that the functionally graded electrodes performed best with highest ionomer loading on the ML-CL interface (ML|40|20) which is also observed in literature for both mathematical and experimentally results [33, 43, 66]. The functionally graded electrode with the highest ionomer content on the outer layer (ML|20|40) was shown to perform the worst due to charge and mass transportation issues. In addition the model showed highest performance in the kinetic and ohmic region for a homogeneous ionomer loaded electrode of 40 wt.% ionomer indicating that at 3.1 μm thick oxygen depletion is not the limiting phenomenon for low to medium current densities.

To validate the mathematical model two functionally graded ionomer electrodes

were fabricated and tested. Experimental results showed an increased kinetic region due to an increase in electrochemical active area for both functionally graded electrodes. The experimental cells showed similar performance in both the kinetic and ohmic regions while the electrode with the lowest ionomer loading on the outer layer showed superior mass transport region performance due to the increased porosity on the outer layer. This differed from the model predictions showing reduced performance for the ML|20|40 electrode due to substantial protonic losses. It is uncertain as to why the experimental ML|20|40 electrode performed as well as the ML|40|20 electrode, therefore, further investigation is required.

5.2 Future Work

The observations in this work have raised a number of possibilities for further investigation. In this study, 20 wt.% Pt|C is investigated for various Pt loadings. Results from the simulations concluded that increasing loading (thickness) caused charge and mass transport losses to increase, thereby reducing cell performance. One further are of research is to investigate the change in performance while keeping the printer passes constant and varying the wt.% Pt|C ratio using 20 wt.% Pt|C, 40 wt.% Pt|C, and 60 wt.% Pt|C. The use of different wt.% Pt|C ratios would allowing the observation of increased platinum without altering thickness. This work can then be used to validate the mathematical model in its ability to capture various Pt concentrations.

Several operating conditions were investigated in this study in order to validate the mathematical model. This work highlighted the substantial performance and mass activity improvements that can be achieved at higher oxygen partial pressures as well as increased kinetic region with back pressure. However, only one back pressure case was used in this study. Future work should focus on testing low Pt content electrodes at differing operating conditions in order to find the condition under which these cells show optimal cell performance. In addition the model was only valid for low oxygen concentrations, diffusion correlations for pure oxygen concentrations should be considered in future versions of the mathematical model as it will allow comparisons of electrodes which are not subject to oxygen transport limitations.

The inkjet printed cells were characterize for various ink types, however, thickness data from 5 to 20 layers was only observed for two of the ink types, namely, Glycerol and Ethylene glycol. In this work it was found that the solvent did not have much

variation on the loading, however, an effect on thicknesses with respect to printer passes changed considerably. From this observation further work on rheology of the catalyst ink could be investigated in order to find the optimal porosity. As the model has been validated for Pt loading, ionomer loading, and oxygen partial pressures the mathematical model could be utilization in this endeavour to guide the optimum porosity/Pt|C ratio/ionomer content using the models optimizations capabilities.

This work extended an existing mathematical model (OpenFCST) to allow simulation of functionally graded electrodes. In this thesis only two functionally graded ionomer electrodes are investigated in order to validate the mathematical model, however several layers can be modelled and fabricated. In future works there is much that can be done, such as, functionally graded Pt and/or ionomer. In addition, utilization of the models optimization capabilities to predict the optimal catalyst layer compositions.

The mathematical model has shown good prediction over a variety of operating conditions and loadings. However, future work can be done to increase the models accurately and high current densities. Possible avenues is to obtain experimentally observed diffusion values through the gas diffusion media and catalyst layers. In addition OpenFCST possess several catalyst layer models that can be used to further investigate the gas-ionomer interface resistance. This phenomenon has been hypothesized as one of the processes reducing cell performance at low Pt loadings and is only recently being investigated in the literature.

References

[1] Shukla S, Taufertshofer K, Bhattacharjee S, Secanell M, Halliop E, Malevich D, and Karan K. Effect of ionomer loading in inkjet printed catalyst coated membranes on pefc performance. pages 123–128, 2012. cited By (since 1996)0.

[2] Yu Z, Carter R, and Zhang J. Measurements of pore size distribution, porosity, effective oxygen diffusivity, and tortuosity of pem fuel cell electrodes. *Fuel Cells*, 12(4):557–565, 2012. cited By (since 1996)4.

[3] Grove W. Xxiv. on voltaic series and the combination of gases by platinum. *Philosophical Magazine Series 3*, 14(86):127–130, 1839. doi: 10.1080/14786443908649684.

[4] Steele B and Heinzel A. Materials for fuel-cell technologies. *Nature*, 414(6861): 345–352, 2001. cited By (since 1996)3056.

[5] Hayre R. O, Cha S. W, Colella W, and Prinz F. B. *Fuel Cell Fundamentals*. Wiley, New York, USA, 2 edition, 2008.

[6] Gottesfeld S and Zawodzinski T. Polymer electrolyte fuel cells. *Advances in Electrochemical Science and Engineering*, 5:195–301, 1997. cited By (since 1996)486.

[7] Jung D, Lee C, Kim C, and Shin D. Performance of a direct methanol polymer electrolyte fuel cell. *Journal of Power Sources*, 71(1-2):169–173, 1998. cited By (since 1996)126.

[8] Prakash J, Tryk D, Aldred W, and Yeager E. Investigations of ruthenium pyrochlores as bifunctional oxygen electrodes. *Journal of Applied Electrochemistry*, 29(12):1463–1469, 1999. cited By (since 1996)40.

[9] Paulus U, Wokaun A, Scherer G, Schmidt T, Stamenkovic V, Markovic N, and Ross P. Oxygen reduction on high surface area pt-based alloy catalysts in

comparison to well defined smooth bulk alloy electrodes. *Electrochimica Acta*, 47(22-23):3787–3798, 2002. cited By (since 1996)334.

[10] Fournier J, Lalande G, Ct R, Guay D, and Dodelet J.-P. Activation of various fe-based precursors on carbon black and graphite supports to obtain catalysts for the reduction of oxygen in fuel cells. *Journal of the Electrochemical Society*, 144(1):218–226, 1997. cited By (since 1996)67.

[11] Chiem B, Beattie P, and Colbow K. The development and demonstration of technology on the path to commercially viable pem fuel cell stacks. volume 16, pages 1927–1935, 2008. cited By (since 1996)2.

[12] Cavarroc M, Ennadjaoui A, Mougenot M, Brault P, Escalier R, Tessier Y, Durand J, Roualds S, Sauvage T, and Coutanceau C. Performance of plasma sputtered fuel cell electrodes with ultra-low pt loadings. *Electrochemistry Communications*, 11(4):859–861, 2009. cited By (since 1996)46.

[13] Saha M, Malevich D, Halliop E, Pharoah J, Peppley B, and Karan K. Electrochemical activity and catalyst utilization of low pt and thickness controlled membrane electrode assemblies. *Journal of the Electrochemical Society*, 158(5): B562–B567, 2011. cited By (since 1996)36.

[14] Moore M. Investigation of the Double-Trap Intrinsic Kinetic Equation for the Oxygen Reduction Reaction and its implementation into a Membrane Electrode Assembly model. Master's thesis, University of Alberta, 2012.

[15] Secanell M, Putz A, Zingan V, Bhaiya M, Moore M, Dobson P, Wardlaw P, and Domican K. Open-source Fuel Cell Simulation Toolbox (OpenFCST): User and Developer's Reference Guide, September 2013. Taken on November 05, 2013.

[16] Papageorgopoulos D. DOE fuel cell technology program overview and introduction to the 2010 fuel cell pre-solicitation workshop in DOE fuel cell pre-solicitation workshop. Technical report, Department of Energy, Lakewood, Colorado, 2010.

[17] Bhaiya M. An open-source two-phase non-isothermal mathematical model of a polymer electrolyte membrane fuel cell. Master's thesis, University of Alberta, 2013.

[18] Ferng Y and Su A. A three-dimensional full-cell cfd model used to investigate the effects of different flow channel designs on pemfc performance. *International Journal of Hydrogen Energy*, 32(17):4466–4476, 2007. cited By (since 1996)60.

[19] Bender G, Zawodzinski T, and Saab A. Fabrication of high precision pefc membrane electrode assemblies. *Journal of Power Sources*, 124(1):114–117, 2003. cited By (since 1996)43.

[20] Kim C, Chun Y, Peck D, and Shin D. A novel process to fabricate membrane electrode assemblies for proton exchange membrane fuel cells. *International Journal of Hydrogen Energy*, 23(11):1045 – 1048, 1998. ISSN 0360-3199. doi: http://dx.doi.org/10.1016/S0360-3199(98)00021-4.

[21] Hobson L, Nakano Y, Ozu H, and Hayase S. Targeting improved dmfc performance. *Journal of Power Sources*, 104(1):79–84, 2002. cited By (since 1996)76.

[22] Cho Y.-H, Park H.-S, Cho Y.-H, Park I.-S, and Sung Y.-E. The improved methanol tolerance using pt/c in cathode of direct methanol fuel cell. *Electrochimica Acta*, 53(20):5909–5912, 2008. cited By (since 1996)9.

[23] Martin S, Garcia-Ybarra P, and Castillo J. High platinum utilization in ultra-low pt loaded pem fuel cell cathodes prepared by electrospraying. *International Journal of Hydrogen Energy*, 35(19):10446–10451, 2010. cited By (since 1996)26.

[24] Park I.-S, Li W, and Manthiram A. Fabrication of catalyst-coated membrane-electrode assemblies by doctor blade method and their performance in fuel cells. *Journal of Power Sources*, 195(20):7078–7082, 2010. cited By (since 1996)18.

[25] Mehta V and Cooper J. Review and analysis of pem fuel cell design and manufacturing. *Journal of Power Sources*, 114(1):32–53, 2003. cited By (since 1996)744.

[26] Wagner N, Kaz T, and Friedrich K. Investigation of electrode composition of polymer fuel cells by electrochemical impedance spectroscopy. *Electrochimica Acta*, 53(25):7475–7482, 2008. cited By (since 1996)21.

[27] Cunningham N, Irissou E, Lefvre M, Denis M.-C, Guay D, and Dodelet J.-P. Pemfc anode with very low pt loadings using pulsed laser deposition. *Electrochemical and Solid-State Letters*, 6(7):A125–A128, 2003. cited By (since 1996)26.

[28] Hirano S, Kim J, and Srinivasan S. High performance proton exchange membrane fuel cells with sputter-deposited pt layer electrodes. *Electrochimica Acta*, 42(10):1587–1593, 1997. cited By (since 1996)193.

[29] Mukerjee S, Srinivasan S, and Appleby A. Effect of sputtered film of platinum on low platinum loading electrodes on electrode kinetics of oxygen reduction in proton exchange membrane fuel cells. *Electrochimica Acta*, 38(12):1661–1669, 1993. cited By (since 1996)120.

[30] Pozio A, De Francesco M, Cemmi A, Cardellini F, and Giorgi L. Comparison of high surface pt/c catalysts by cyclic voltammetry. *Journal of Power Sources*, 105(1):13–19, 2002. cited By (since 1996)529.

[31] Tsou Y, Cao L, and De Castro E. Novel high performance platinum and alloy catalysts for pemfc and dmfc. volume 49, pages 679–680, 2004. cited By (since 1996)2.

[32] Rao R and Rengaswamy R. Optimization study of an agglomerate model for platinum reduction and performance in pem fuel cell cathode. *Chemical Engineering Research and Design*, 84(10 A):952–964, 2006. cited By (since 1996)16.

[33] Taylor A, Kim E, Humes V, Kizuka J, and Thompson L. Inkjet printing of carbon supported platinum 3-d catalyst layers for use in fuel cells. *Journal of Power Sources*, 171(1):101–106, 2007. cited By (since 1996)50.

[34] Towne S, Viswanathan V, Holbery J, and Rieke P. Fabrication of polymer electrolyte membrane fuel cell meas utilizing inkjet print technology. *Journal of Power Sources*, 171(2):575–584, 2007. cited By (since 1996)28.

[35] Young D, Sukeshini A, Cummins R, Xiao H, Rottmayer M, and Reitz T. Inkjet printing of electrolyte and anode functional layer for solid oxide fuel cells. *Journal of Power Sources*, 184(1):191–196, 2008. cited By (since 1996)27.

[36] Wilson M. S and Goffesfeld S. High performance catalyzed membranes of ultra-low pt loadings for polymer electrolyte fuel cells. *Journal of the Electrochemical Society*, 139(2):L28–L30, 1992. cited By (since 1996)385.

[37] Chun Y.-G, Kim C.-S, Peck D.-H, and Shin D.-R. Performance of a polymer electrolyte membrane fuel cell with thin film catalyst electrodes. *Journal of Power Sources*, 71(1-2):174–178, 1998. cited By (since 1996)84.

[38] Wilson M and Gottesfeld S. Thin-film catalyst layers for polymer electrolyte fuel cell electrodes. *Journal of Applied Electrochemistry*, 22(1):1–7, 1992. cited By (since 1996)621.

[39] Saha M, Tam M, Berejnov V, Susac D, McDermid S, Hitchcock A, and Stumper J. Characterization and performance of catalyst layers prepared by inkjet printing technology. volume 58, pages 797–806, 2013. cited By (since 1996)0.

[40] Xie J, Xu F, Wood III D, More K, Zawodzinski T, and Smith W. Influence of ionomer content on the structure and performance of pefc membrane electrode assemblies. *Electrochimica Acta*, 55(24):7404–7412, 2010. cited By (since 1996)18.

[41] Lee S, Mukerjee S, McBreen J, Rho Y, Kho Y, and Lee T. Effects of nafion impregnation on performances of pemfc electrodes. *Electrochimica Acta*, 43(24): 3693–3701, 1998. cited By (since 1996)280.

[42] Qi Z and Kaufman A. Low pt loading high performance cathodes for pem fuel cells. *Journal of Power Sources*, 113(1):37–43, 2003. cited By (since 1996)164.

[43] Sasikumar G, Ihm J, and Ryu H. Optimum nafion content in pem fuel cell electrodes. *Electrochimica Acta*, 50(2-3 SPEC. ISS.):601–605, 2004. cited By (since 1996)81.

[44] Antolini E. Recent developments in polymer electrolyte fuel cell electrodes. *Journal of Applied Electrochemistry*, 34(6):563–576, 2004. cited By (since 1996)110.

[45] Costamagna P and Srinivasan S. Quantum jumps in the pemfc science and technology from the 1960s to the year 2000: Part i. fundamental scientific aspects. *Journal of Power Sources*, 102(1-2):242–252, 2001. cited By (since 1996)637.

[46] Huang K.-L, Lai Y.-C, and Tsai C.-H. Effects of sputtering parameters on the performance of electrodes fabricated for proton exchange membrane fuel cells. *Journal of Power Sources*, 156(2):224–231, 2006. cited By (since 1996)30.

[47] Wilson M and Gottesfeld S. Thin-film catalyst layers for polymer electrolyte fuel cell electrodes. *Journal of Applied Electrochemistry*, 22(1):1–7, 1992. ISSN 0021-891X. doi: 10.1007/BF01093004.

[48] Su H.-N, Zeng Q, Liao S.-J, and Wu Y.-N. High performance membrane electrode assembly with ultra-low platinum loading prepared by a novel multi catalyst layer technique. *International Journal of Hydrogen Energy*, 35(19):10430–10436, 2010. cited By (since 1996)8.

[49] Martin S, Garcia-Ybarra P, and Castillo J. Electrospray deposition of catalyst layers with ultra-low pt loadings for pem fuel cells cathodes. *Journal of Power Sources*, 195(9):2443–2449, 2010. cited By (since 1996)25.

[50] Wang X, Richey F, Wujcik K, and Elabd Y. Ultra-low platinum loadings in polymer electrolyte membrane fuel cell electrodes fabricated via simultaneous electrospinning/electrospraying method. *Journal of Power Sources*, 264:42–48, 2014. cited By (since 1996)1.

[51] Ohma A, Mashio T, Sato K, Iden H, Ono Y, Sakai K, Akizuki K, Takaichi S, and Shinohara K. Analysis of proton exchange membrane fuel cell catalyst layers for reduction of platinum loading at nissan. *Electrochimica Acta*, 56(28): 10832–10841, 2011. cited By (since 1996)19.

[52] Martin S, Martinez-Vazquez B, Garcia-Ybarra P, and Castillo J. Peak utilization of catalyst with ultra-low pt loaded pem fuel cell electrodes prepared by the electrospray method. *Journal of Power Sources*, 229:179–184, 2013. cited By (since 1996)5.

[53] Fofana D, Natarajan S, Hamelin J, and Benard P. Low platinum, high limiting current density of the pemfc (proton exchange membrane fuel cell) based on multilayer cathode catalyst approach. *Energy*, 64:398–403, 2014. cited By (since 1996)2.

[54] Fofana D, Hamelin J, and Bnard P. Modelling and experimental validation of high performance low platinum multilayer cathode for polymer electrolyte membrane fuel cells (pemfcs). *International Journal of Hydrogen Energy*, 38 (24):10050–10062, 2013. cited By (since 1996)2.

[55] Tian Z, Lim S, Poh C, Tang Z, Xia Z, Luo Z, Shen P, Chua D, Feng Y, Shen Z, and Lin J. A highly order-structured membrane electrode assembly with vertically aligned carbon nanotubes for ultra-low pt loading pem fuel cells. *Advanced Energy Materials*, 1(6):1205–1214, 2011. cited By (since 1996)18.

[56] Mashio T, Ohma A, Yamamoto S, and Shinohara K. Analysis of reactant gas transport in a catalyst layer. volume 11, pages 529–540, 2007. cited By (since 1996)20.

[57] Greszler T, Caulk D, and Sinha P. The impact of platinum loading on oxygen transport resistance. *Journal of the Electrochemical Society*, 159(12):F831–F840, 2012. cited By (since 1996)9.

[58] Suzuki T, Kudo K, and Morimoto Y. Model for investigation of oxygen transport limitation in a polymer electrolyte fuel cell. *Journal of Power Sources*, 222:379–389, 2013. cited By (since 1996)0.

[59] Yoon W and Weber A. Modeling low-platinum-loading effects in fuel-cell catalyst layers. *Journal of the Electrochemical Society*, 158(8):B1007–B1018, 2011. cited By (since 1996)30.

[60] Wang J, Zhang J, and Adzic R. Double-trap kinetic equation for the oxygen reduction reaction on pt(111) in acidic media. *Journal of Physical Chemistry A*, 111(49):12702–12710, 2007.

[61] Moore M, Putz A, and Secanell M. Investigation of the ORR using the double-trap intrinsic kinetic model. *Journal of the Electrochemical Society*, 160(6): F670–F681, 2013.

[62] Ruvinskiy P, Bonnefont A, and Savinova E. 3d-ordered layers of vertically aligned carbon nanofilaments as a model approach to study electrocatalysis on nanomaterials. *Electrochimica Acta*, 84:174–186, 2012. cited By (since 1996)2.

[63] Xie Z, Navessin T, Shi K, Chow R, Wang Q, Song D, Andreaus B, Eikerling M, Liu Z, and Holdcroft S. Functionally graded cathode catalyst layers for polymer electrolyte fuel cells ii. experimental study of the effect of nafion distribution. *Journal of the Electrochemical Society*, 152(6):A1171–A1179, 2005. cited By (since 1996)90.

[64] Wang Q, Eikerling M, Song D, Liu Z, Navessin T, Xie Z, and Holdcroft S. Functionally graded cathode catalyst layers for polymer electrolyte fuel cells: I. theoretical modeling. *Journal of the Electrochemical Society*, 151(7):A950–A957, 2004. cited By (since 1996)78.

[65] Yoon Y.-G, Yang T.-H, Park G.-G, Lee W.-Y, and Kim C.-S. A multi-layer structured cathode for the pemfc. *Journal of Power Sources*, 118(1-2):189–192, 2003. cited By (since 1996)27.

[66] Song D, Wang Q, Liu Z, Eikerling M, Xie Z, Navessin T, and Holdcroft S. A method for optimizing distributions of nafion and pt in cathode catalyst layers of pem fuel cells. *Electrochimica Acta*, 50(16-17):3347–3358, 2005. cited By (since 1996)71.

[67] Antoine O, Bultel Y, Ozil P, and Durand R. Catalyst gradient for cathode active layer of proton exchange membrane fuel cell. *Electrochimica Acta*, 45 (27):4493–4500, 2000. cited By (since 1996)56.

[68] Al-Baghdadi M. Modelling of proton exchange membrane fuel cell performance based on semi-empirical equations. *Renewable Energy*, 30(10):1587–1599, 2005. cited By (since 1996)42.

[69] Haraldsson K and Wipke K. Evaluating pem fuel cell system models. *Journal of Power Sources*, 126(1-2):88–97, 2004. cited By (since 1996)69.

[70] Kim J, Lee S.-M, Srinivasan S, and Chamberlin C. E. Modeling of proton exchange membrane fuel cell performance with an empirical equation. *Journal of the Electrochemical Society*, 142(8):2670–2674, 1995. cited By (since 1996)348.

[71] Block D. L and T-Raissi A. Hydrogen research at florida universities. Technical report, National Aeronautics and Space Administration, 2009.

[72] Abrmoff D. M. D, Magalhes D. P. J, and Ram D. S. J. Image processing with imagej. *Biophotonics International*, 11(7):36–42, July 2004.

[73] Neyerlin K, Gu W, Jorne J, and Gasteiger H. Determination of catalyst unique parameters for the oxygen reduction reaction in a pemfc. *Journal of the Electrochemical Society*, 153(10):A1955–A1963, 2006. cited By (since 1996)131.

[74] Collier A, Wang H, Zi Yuan X, Zhang J, and Wilkinson D. Degradation of polymer electrolyte membranes. *International Journal of Hydrogen Energy*, 31 (13):1838–1854, 2006. cited By (since 1996)201.

[75] Carter R, Kocha S, Wagner F, Fay M, and Gasteiger H. Artifacts in measuring electrode catalyst area of fuel cells through cyclic voltammetry. volume 11, pages 403–410, 2007. cited By (since 1996)30.

[76] Ralph T, Hards G, Keating J, Campbell S, Wilkinson D, Davis M, St-Pierre J, and Johnson M. Low cost electrodes for proton exchange membrane fuel cells: Performance in single cells and ballard stacks. *Journal of the Electrochemical Society*, 144(11):3845–3857, 1997. cited By (since 1996)242.

[77] Kinoshita K and Stonehart P. Preparation and characterization of highly dispersed electrocatalytic materials. *Mod Aspects Electrochem*, (12):183–267, 1977. cited By (since 1996)2.

[78] Gloaguen F, Lger J.-M, and Lamy C. Electrocatalytic oxidation of methanol on platinum nanoparticles electrodeposited onto porous carbon substrates *. *Journal of Applied Electrochemistry*, 27(9):1052–1060, 1997. cited By (since 1996)156.

[79] Secanell M. *Computational modeling and optimization of proton exchange membrane fuel cells*. PhD thesis, University of Victoria, November 2007.

[80] Bird R. B, Stewart W. E, and Lightfoot E. N. *Transport Phenomena, Revised 2nd Edition*. John Wiley & Sons, Inc., 2nd edition, December 2006. ISBN 0470115394.

[81] Tomadakis M. M and Sotirchos S. V. Effective Knudsen diffusivities in structures of randomly overlapping fibers. *AIChE Journal*, 37(1):74–86, 1991.

[82] Stauffer D and Aharony A. *Introduction to Percolation Theory*. Taylor & Francis, 2nd edition edition, 1992.

[83] Isichenko M. Percolation, statistical topography, and transport in random media. *Reviews of Modern Physics*, 64(4):961–1043, 1992. cited By (since 1996)708.

[84] Tomadakis M. M and Sotirchos S. V. Ordinary and transition regime diffusion in random fiber structures. *AIChE Journal*, 39(3):397–412, 1993.

[85] Bard A. J and Faulkner L. R. *Electrochemical Methods: Fundamentals and Applications*. John Wiley & Sons, Inc., second edition, 2001.

[86] Springer T, Zawodzinski T, and Gottesfeld S. Polymer electrolyte fuel cell model. *Journal of the Electrochemical Society*, 138(8):2334–2342, 1991.

[87] Iden H, Sato K, Ohma A, and Shinohara K. Relationship among Microstructure, Ionomer Property and Proton Transport in Pseudo Catalyst Layers. *Journal of The Electrochemical Society*, 158(8):B987–B994, 2011.

[88] Peron J, Mani A, Zhao X, Edwards D, Adachi M, Soboleva T, Shi Z, Xie Z, Navessin T, and Holdcroft S. Properties of Nafion® NR-211 membranes for PEMFCs. *Journal of Membrane Science*, 356(1-2):44–51, 2010.

[89] BekkTech L. In-Plane Conductivity Testing Procedures & Results, 2007. Taken on August 10, 2010.

[90] Dobson P, Lei C, Navessin T, and Secanell M. Characterization of the PEM fuel cell catalyst layer microstructure by nonlinear least-squares parameter estimation. *Journal of the Electrochemical Society*, 159(5):B514–B523, 2012.

[91] Ren X and Gottesfeld S. Electro-osmotic drag of water in poly(perfluorosulfonic acid) membranes. *Journal of the Electrochemical Society*, 148(1):A87–A93, 2001. cited By (since 1996)176.

[92] Zawodzinski T, Davey J, Valerio J, and Gottesfeld S. The water content dependence of electro-osmotic drag in proton-conducting polymer electrolytes. *Electrochimica Acta*, 40(3):297–302, 1995. cited By (since 1996)394.

[93] O'Hayre R, Cha S, Colella W, and Prinz F. *Fuel Cell Fundamentals*. John Wiley & sons, 2nd edition, 2010.

[94] Bhaiya M, Moore M, and Secanell M. Development of a single-phase non-isothermal MEA model for multi-step Oxygen Reduction Reaction (ORR) kinetics. Presented at the Hydrogen + Fuel Cells Congerence 2013, Vancouver, June 16-19 2013.

[95] Sun W, Peppley B, and Karan K. An improved two-dimensional agglomerate cathode model to study the influence of catalyst layer structural parameters. *Electrochimica Acta*, 50(16-17):3359–3374, 2005.

[96] Gottesfeld S. Some observations on the oxygen reduction reaction (ORR) at platinum catalysts based on post year 2000 reports. volume 6, pages 51–67, 2008. cited By (since 1996)17.

[97] Damjanovic A, Dey A, and Bockris J. Kinetics of oxygen evolution and dissolution on platinum electrodes. *Electrochimica Acta*, 11(7):791–814, 1966. cited By (since 1996)77.

[98] Wang J, Zhang J, and Adzic R. R. Double-trap kinetic equation for the oxygen reduction reaction on pt(111) in acidic media. *J. Phys. Chem. A*, 111:12702–12710, 2007.

[99] Ruvinskiy P, Bonnefont A, Pham-Huu C, and Savinova E. Using ordered carbon nanomaterials for shedding light on the mechanism of the cathodic oxygen reduction reaction. *Langmuir*, 27(14):9018–9027, 2011. cited By (since 1996)20.

[100] Subramanian N, Greszler T, Zhang J, Gu W, and Makharia R. Pt-oxide coverage-dependent oxygen reduction reaction (orr) kinetics. *Journal of the Electrochemical Society*, 159(5):B531–B540, 2012. cited By (since 1996)9.

[101] Parthasarathy A, Srinivasan S, Appleby A. J, and Martin C. R. Pressure dependence of the oxygen reduction reaction at the platinum microelectrode/nafion interface: Electrode kinetics and mass transport. *Journal of the Electrochemical Society*, 139(9):2530–2537, 1992.

[102] Parthasarathy A, Srinivasan S, Appleby A. J, and Martin C. R. Temperature dependence of the electrode kinetics of oxygen reduction at the platinum/nafion interface—a microelectrode investigation. *Journal of the Electrochemical Society*, 139(10):2856–2862, 1992.

[103] Chen S and Kucernak A. Electrocatalysis under conditions of high mass transport: Investigation of hydrogen oxidation on single submicron pt particles supported on carbon. *Journal of Physical Chemistry B*, 108(37):13984–13994, 2004. cited By (since 1996)91.

[104] Wang J, Springer T, and Adzic R. Dual-pathway kinetic equation for the hydrogen oxidation reaction on pt electrodes. *Journal of the Electrochemical Society*, 153(9):A1732–A1740, 2006. cited By (since 1996)70.

[105] Hinatsu J. T, Mizuhata M, and Takenaka H. Water uptake of perfluorosulfonic acid membranes from liquid water and water vapor. *Journal of the Electrochemical Society*, 141(6):1493–1498, 1994.

[106] Liu Y, Murphy M, Baker D, Gu W, Ji C, Jorne J, and Gasteiger H. Proton conduction and oxygen reduction kinetics in PEM fuel cell cathodes: Effects of ionomer-to-carbon ratio and relative humidity. *Journal of the Electrochemical Society*, 156(8):B970–B980, 2009.

[107] Davis T. A. Algorithm 832: UMFPACK, an unsymmetric-pattern multifrontal method. *ACM Transactions on Mathematical Software*, 30(2):196–199, June 2004.

[108] Nam J and Kaviany M. Effective diffusivity and water-saturation distribution in single- and two-layer PEMFC diffusion medium. *International Journal of Heat and Mass Transfer*, 46(24):4595–4611, 2003.

[109] Pharoah J, Karan K, and Sun W. On effective transport coefficients in PEM fuel cell electrodes: Anisotropy of the porous transport layers. *Journal of Power Sources*, 161(1):214–224, 2006.

[110] Zamel N, Litovsky E, Shakhshir S, Li X, and Kleiman J. Measurement of in-plane thermal conductivity of carbon paper diffusion media in the temperature range of -20C to +120C. *Applied Energy*, 88(9):3042–3050, 2011.

[111] Zamel N, Litovsky E, Li X, and Kleiman J. Measurement of the through-plane thermal conductivity of carbon paper diffusion media for the temperature range from -50 to +120 c. *International Journal of Hydrogen Energy*, 36(19):12618–12625, 2011.

[112] Karimi G, Li X, and Teertstra P. Measurement of through-plane effective thermal conductivity and contact resistance in PEM fuel cell diffusion media. *Electrochimica Acta*, 55(5):1619–1625, 2010.

[113] Teertstra P, Karimi G, and Li X. Measurement of in-plane effective thermal conductivity in PEM fuel cell diffusion media. *Electrochimica Acta*, 56(3):1670–1675, 2011.

[114] Dobson P. Investigation of the Polymer Electrolyte Membrane Fuel Cell Catalyst Layer Microstructure. Master's thesis, University of Alberta, September 2011.

[115] Yu Z and Carter R. N. Measurement of effective oxygen diffusivity in electrodes for proton exchange membrane fuel cells. *Journal of Power Sources*, 195(4):1079 – 1084, 2010. ISSN 0378-7753.

[116] Khandelwal M and Mench M. Direct measurement of through-plane thermal conductivity and contact resistance in fuel cell materials. *Journal of Power Sources*, 161(2):1106–1115, 2006. cited By (since 1996)138.

[117] Khandelwal M and Mench M. Direct measurement of through-plane thermal conductivity and contact resistance in fuel cell materials. *Journal of Power Sources*, 161(2):1106–1115, 2006.

[118] Xiong L and Manthiram A. High performance membrane-electrode assemblies with ultra-low Pt loading for proton exchange membrane fuel cells. *Electrochimica Acta*, 50(16-17):3200–3204, 2005. cited By (since 1996)51.

[119] E-TEK . Specifications for C-1: HP Platinum on Vulcan XC-72. *www.etek-inc.com*, Data accessed on February 2, 2007.

[120] Soboleva T, Malek K, Xie Z, Navessin T, and Holdcroft S. Pemfc catalyst layers: The role of micropores and mesopores on water sorption and fuel cell activity. *ACS Applied Materials and Interfaces*, 3(6):1827–1837, 2011. cited By (since 1996)19.

[121] Cho Y.-H, Park H.-S, Cho Y.-H, Jung D.-S, Park H.-Y, and Sung Y.-E. Effect of platinum amount in carbon supported platinum catalyst on performance of polymer electrolyte membrane fuel cell. *Journal of Power Sources*, 172(1): 89–93, 2007. cited By (since 1996)28.

[122] Prasanna M, Ha H, Cho E, Hong S.-A, and Oh I.-H. Investigation of oxygen gain in polymer electrolyte membrane fuel cells. *Journal of Power Sources*, 137 (1):1–8, 2004. cited By (since 1996)47.

[123] Zhang J, Li H, and Zhang J. Effect of operating backpressure on pem fuel cell performance. volume 19, pages 65–76, 2009. cited By (since 1996)3.

[124] Zhang J, Song C, Zhang J, Baker R, and Zhang L. Understanding the effects of backpressure on pem fuel cell reactions and performance. *Journal of Electroanalytical Chemistry*, 688:130–136, 2013. cited By (since 1996)0.